Advances in heterogeneous ice nucleation research: theoretical modeling and measurements

Submitted in partial fulfillment of the requirements for

the degree of

Doctor of Philosophy

in

Mechanical Engineering

Hassan Beydoun

B.E., Mechanical Engineering, American University of Beirut
M.S., Mechanical Engineering, Carnegie Mellon University

Carnegie Mellon University
Pittsburgh, PA

February, 2017
(in which degree was or will be conferred)

The views and conclusions contained in this document are those of the author, and should not be interpreted as representing the official policies, either expressed or implied, of any sponsoring institution, the U.S. government, or any other entity.

Dedicated to my mother

Acknowledgements

I would like to start off by thanking my advisor Professor Ryan Sullivan. From the moment I started at the Center for Atmospheric Particle Studies (CAPS) in CMU, Ryan has inspired me to keep pushing my intellectual limits. The research we have done together has been challenging and quite daunting at times, but he remained a believer in the power of perseverance and staying on target. I am grateful for the humbling opportunity he gave me and for allowing me to pursue research at this level. It has been an honor working with a such a creative scientist who doesn't believe in the easy way out and inspires such academic rigor.

The work was in part supported by the two NSF grants: CHE-1213718 & CHE-1554941. I would also like to thank Diane and Bradford Smith as well as John and Claire Bertucci for their generous fellowships that supported part of my PhD.

I am grateful to have a thesis committee composed of exceptional and inspiring scientists. A very special thanks to Alan McGaughey, Peter Adams, and Neil Donahue for agreeing to help guide me in the last stages of my PhD. Their feedback and support has been immensely valuable.

Neil has been there for me every time I needed an imaginative research eye or just needed to talk science. We also ride bikes together and nothing can beat that!

It is very difficult to start writing about Rawad Saleh and not get emotionally overwhelmed. He has been both a mentor and a best friend. Rawad was there for me every step of the way, through the good and the bad. Inspiring conversations with Rawad have greatly contributed to coming up with my ice nucleation framework. It is impossible to envision me completing this PhD without him. I can't wait to come down and visit him in Georgia right after I finally submit this document!

I was very lucky to be part of the mechanical engineering department at Carnegie Mellon. I'd really like to thank the department head and CAPS professor Allen Robinson who was always there if a PhD student needed help or guidance. The department grad program administrator Chris Hertz is a wonderful human who in every sense of the word had his door open every time I needed to talk. Thank you Chris!

Where I am today would not have been possible had I not met and worked with my undergraduate advisor Alan Shihadeh. I am forever indebted to his willingness to take on an undergrad who knew nothing about research and preparing him for PhD level work. Alan is an inspiration, and his work for the American University of Beirut, Lebanon, and the entire region is invaluable.

Kyle Gorkowski has been a wonderful lab mate, research mate, and friend. Ever since he joined CAPS shortly after I did, Kyle and I did great things with the optical tweezers. Much of the work in analyzing my data in Chapter 4 of this dissertation would not be possible without Kyle's coding resourcefulness. We also became great friends, enjoying many scientific conversations over fantastic wine. I will sorely miss having him around.

My lab mate and friend Michael Polen is a talented experimentalist who I've had the honor of working with and learning from. Much of the freezing data sets presented and analyzed in Chapters 2 and 3 were retrieved by Mike. I am incredibly grateful for his willingness to treat his work like it was ours, exhibiting outstanding scientific citizenship. I will also miss his seemingly abrupt political rants!

Not one single event (or non-event) of my last 3.5 years of life in Pittsburgh didn't involve my dear friend Georges Saliba. Georges and I go back to our sophomore year of college when we met

in real analysis (ouch). Since then we have enabled each other in every single way imaginable. Georges has been an integral part of my ice nucleation model as he was always ready to discuss any advances or ideas I had on it. I'd also like to thank my friend Maria Yazighi who along with Georges gave me tremendous amount of support in the last couple of months of my PhD. Many dinners were prepared for me by these two selfless humans as I wrote this document!

I'd like to thank my awesome friends Ellis Robinson and Daniel Tkacik, my formerly senior colleagues at CAPS, who in my second year of grad school showed me how best take advantage of grad life in this beautiful city. They also introduced me to cycling, which I deeply appreciate. I don't think I've ever met someone as critical as Ellis, he epitomizes the ideal scientist in that regard as loose/weak arguments just don't fly with him. I am really grateful for that, as it made a better scientist and person.

CAPS has been a wonderful place to do research. My biggest struggle in finding a post doc is the feeling that I've already been at the best work environment possible. I'd like to give a shout out to my office mate Elina Karnezi for stabilizing my blood sugar at critical times and everyone in the Sullivan group: Leif, Lydia, Tom and Qing. Of course I can't forget Adam Ahern, who started his PhD with me and defended a day after I did. He has always been there for me, be it science or ranting.

My very close friend from Lebanon Khairallah Atwi has inspired and enabled my passion for science ever since we met in college. His intellect is a standard to live up to. I am also grateful for Ayla Tabbara who supported me through the first few years of my PhD and continues to be there for me today. My best friends from high school: Fuad, Samer, and Majd told me I could be a scientist when I said it was my dream 12 years ago! The luck I've had!

I'm filled with love and gratitude for Meredith Schervish who reignited my passion for my work recently in a way I never thought would be possible. I can't thank her enough for continuously telling me I could do it and for listening to me read my chapters out loud. Chapter 3 on Snomax and ice nucleating mixtures is dedicated to Meredith, as she instilled the pleasure and drive with which that chapter was written.

Last (and not surely not least) I'd like to thank my wonderful family: my uncle Mouhib and cousin Rawan for travelling from Beirut to watch me defend. My aunt Iman who's always been a second mother to me. Of course my wonderful sister Assile for an entire lifetime of unconditional love. My father Ali who charged my original drive for science when he taught me about special relativity and for showing me nothing but love and overwhelming support since the day I was born. My mother Randa who is the most selfless human imaginable, always putting my sister and I first before anything else and loving us no matter what. No words can truly capture what my family has done for me.

Abstract

In the atmosphere, cloud droplets can remain in a supercooled liquid phase at temperatures as low as -40 °C. Above this temperature, cloud droplets freeze via heterogeneous ice nucleation whereby a rare and poorly understood subset of atmospheric particles catalyze the ice phase transition. As the phase state of clouds is critical in determining their radiative properties and lifetime, deficiencies in our understanding of heterogeneous ice nucleation poses a large uncertainty on our efforts to predict human induced global climate change.

Experimental challenges in properly simulating particle-induced freezing processes under atmospherically relevant conditions have largely contributed to the absence of a well-established model and parameterizations that accurately predict heterogeneous ice nucleation. Conversely, the sparsity of reliable measurement techniques available struggle to be interpreted by a single consistent theoretical or empirical framework, which results in layers of uncertainty when attempting to extrapolate useful information regarding ice nucleation for use in atmospheric cloud models.

In this dissertation a new framework for describing heterogeneous ice nucleation is developed. Starting from classical nucleation theory, the surface of an ice nucleating particle is treated as a continuum of heterogeneous ice nucleating activity and a particle specific distribution of this activity g is derived. It is hypothesized that an individual particle species exhibits a critical surface area. Above this critical area the ice nucleating activity of a particle species can be described by one g distribution, $\bar{g}$, while below it $\bar{g}$ expresses itself expresses externally resulting in particle to particle variability in ice nucleating activity. The framework is supported by cold plate droplet freezing measurements for dust and biological particles in which the total surface area of particle

material available is varied. Freezing spectra above a certain surface area are shown to be successfully fitted with $\bar{g}$ while a process of random sampling from $\bar{g}$ can predict the freezing behavior below the identified critical surface area threshold. The framework is then extended to account for droplets composed of multiple particle species and successfully applied to predict the freezing spectra of a mixed proxy for an atmospheric dust-biological particle system.

The contact freezing mode of ice nucleation, whereby a particle induces freezing upon collision with a droplet, is thought to be more efficient than particle initiated immersion freezing from within the droplet bulk. However, it has been a decades' long challenge to accurately measure this ice nucleation mode, since it necessitates reliably measuring the rate at which particles hit a droplet surface combined with direct determination of freezing onset. In an effort to remedy this longstanding deficiency a temperature controlled chilled aerosol optical tweezers capable of stably isolating water droplets in air at subzero temperatures has been designed and implemented. The new temperature controlled system retains the powerful capabilities of traditional aerosol optical tweezers: retrieval of a cavity enhanced Raman spectrum which could be used to accurately determine the size and refractive index of a trapped droplet. With these capabilities, it is estimated that the design can achieve ice supersaturation conditions at the droplet surface. It was also found that a KCl aqueous droplet simultaneously cooling and evaporating exhibited a significantly higher measured refractive index at its surface than when it was held at a steady state temperature. This implies the potential of a "salting out" process. Sensitivity of the cavity enhanced Raman spectrum as well as the visual image of a trapped droplet to dust particle collisions is shown, an important step in measuring collision frequencies of dust particles with a trapped droplet. These results may pave the way for future experiments of the exceptionally poorly understood contact freezing mode of ice nucleation.

Table of Contents

List of Figures

Chapter 1: Introduction

1.1 Background and motivation

Clouds on average cover two thirds of the earth's surface, making them a critical component of the climate system (Baker and Peter, 2008; Hewitt and Jackson, 2007; Robert A. Houze, 1993). They contribute substantially to the planet's radiation budget (Boucher et al., 2013; Quante, 2004) and play a key role in the hydrological cycle due to their control over water transport and availability (Heintzenberg and Charlson, 2009; Hewitt and Jackson, 2007). Despite their importance, many facets of cloud dynamics and microphysics remain poorly constrained which presents a major challenge to forecasting global climate change (Boucher et al., 2013). Clouds and airborne particulate matter (or aerosol particles) are critically linked (Baker, 1997; Boucher et al., 2013; Lohmann and Feichter, 2004; Pilinis et al., 1995). In the atmosphere every cloud droplet must initially form on an aerosol particle via heterogeneous nucleation, as the energy barrier associated with the phase transition from water vapor to liquid is too large and a foreign catalyst is required (Pruppacher and Klett, 1997). Aerosol particles that act as seeds to cloud droplets are termed cloud condensation nuclei (CCN). The freezing of a cloud droplet faces a similar challenge. Water has a propensity to supercool (remain in the liquid phase below its well-known 0 °C thermodynamic freezing point) and above a temperature of -40 °C an external surface is required to aid in the transition to the ice phase (Vali, 1996). Aerosol particles that nucleate ice are termed ice nuclei (IN) and the process by which they freeze droplets is termed heterogeneous ice nucleation (Vali et al., 2015). This intimate connection between aerosol particles and clouds has resulted in aerosol feedbacks on cloud formation, structure, and lifetime being the largest source

of uncertainty in our attempt to quantify future impact of anthropogenic activities on climate (Boucher et al., 2013).

Aerosol particles can affect clouds in different ways. Higher aerosol particle concentrations can lead to decreased average cloud droplet size, since for the same amount of condensed water more particles would lead to more numerous and smaller cloud droplets (Lohmann and Lesins, 2002). This modified cloud structure would lead to cloud brightening, whereby the smaller more tightly packed water droplets make the cloud more reflective leading to a climate cooling effect also known as the first aerosol indirect effect (Boucher et al., 2013; Lohmann and Feichter, 2004). Furthermore, smaller more numerous cloud droplets would extend the lifetime of a cloud as smaller cloud droplets take longer to precipitate, this is known as the second aerosol indirect effect (Boucher et al., 2013; Rosenfeld et al., 2008). The Intergovernmental Panel on Climate Change's latest report characterized our level of scientific understanding of these effects as low, due to a range of potential global forcings induced by aerosol-liquid cloud interactions lying from -0.3 W/m^2 to -1.8 W/m^2. The large uncertainties are attributable to a myriad of shortcomings regarding the complexity of modelling clouds, the difficulty in measuring aerosol impact on clouds, and limited understanding of aerosol particle distribution and composition and its consequent interaction with water (Andreae and Rosenfeld, 2008; Rosenfeld et al., 2013).

While understanding CCN particles remains a limiting factor in quantifying aerosol impacts on clouds, our state of knowledge in that regard has vastly improved in the past decade (Andreae and Rosenfeld, 2008; Bhattu and Tripathi, 2015; Petters and Kreidenweis, 2007). On the other hand, our state of knowledge regarding ice nuclei interactions with cold clouds (supercooled clouds below the melting point of water in contrast to warm clouds which are above freezing) remains fundamentally perplexing (Cantrell and Heymsfield, 2005; Murray et al., 2012). This is quite

problematic due to the vital role IN play in the atmosphere. Unlike CCN, IN are quite rare, often only measuring 1 in 1 million aerosol particles at temperatures as low as -30 °C (DeMott et al., 2010). Despite their sparsity IN control the initiation of the ice phase in a cloud at temperatures above -40 °C, which leads to the onset of the Wegener-Feindsein-Berguron (WFB) process (Pruppacher and Klett, 1997). During the WFB the formed ice crystals grow to precipitation relevant sizes (hundreds of microns) at the expense of the surrounding liquid droplets due to the lower saturated vapor pressure of ice versus supercooled water. The liquid droplets dissipate leading to cloud glaciation (Ervens et al., 2011). This rapid growth of ice crystals at the expense of cloud droplets typically causes rapid sedimentation and precipitation.

It was initially thought that most but not all of precipitation over land was initiated in the ice phase (Baker, 1997), however recent satellite data has shown that almost all of the contribution to precipitation over land indeed starts in the ice phase (Mülmenstädt et al., 2015). Clouds composed of ice crystals also have drastically different optical properties than clouds composed of liquid droplets. Ice clouds are optically thinner due to the larger less numerous ice crystals comprising them, which leads to them having a net warming effect on the radiation budget counter to the net cooling effect of liquid clouds (Baker and Peter, 2008; Gettelman et al., 2012; Pruppacher and Klett, 1997). This contrast can be spotted by the human eye quite nicely on a clear day when the high up thin wispy cirrus clouds comprised of ice crystals lie on top the lower fair weather white puffy cumulus clouds (Houze, 1993). The climate uncertainty from processes involving heterogeneous ice nucleation is threefold: 1) We do not understand the atmospheric distribution or abundance of IN of past climates and the preindustrial era (Tan et al., 2016); 2) We do not understand how much anthropogenic emissions are changing the IN budget (Gettelman et al., 2012); 3) We are unable to accurately represent the freezing process due to IN in climate models

which has implications on the phase state of present and future climate simulations (Storelvmo et al., 2015). These three key shortcomings are all rooted in our poor understanding of IN and the heterogeneous ice nucleation process.

Our worryingly limited understanding of ice nuclei in the atmosphere stems from quite fundamental deficiencies. We still do not understand what exactly makes a particle possess ice nucleating capabilities (Atkinson et al., 2013; Knopf and Koop, 2006; Murray et al., 2012). The longstanding hypothesis has been that particle possessing surface structures mimicking the structure of hexagonal ice can be good IN (Edwards et al., 1962; Fletcher, 1969; Knopf and Koop, 2006; Pruppacher and Klett, 1997; Yankofsky et al., 1981). However the hypothesis has not been enough to aid in narrowing down what atmospheric particles are IN (Cantrell and Heymsfield, 2005). The ability of silver iodide (AgI) to act as IN at very high temperatures of around -5 °C is certainly relatable to it closely resembling the ice crystal structure (Edwards et al., 1962; Fraux and Doye, 2014; Vonnegut, 1947) but that insight has never been extrapolated to atmospheric IN or aided in developing a testable theoretical treatment of heterogonous ice nucleation (Vali, 1996). As there are still no fully developed measurement capabilities that can probe the ice nucleation nano scale process, it may continue to prove difficult to comprehend from first principles (Cantrell and Heymsfield, 2005; Murray et al., 2012; Vali, 1996).

Over the years, laboratory measurements have provided evidence that confirms the role of certain mineral dust particle components as highly effective IN (Knopf and Koop, 2006). Kaolinite and illite clays, feldspars, and quartz are all mineral categories that are atmospherically relevant and have been shown to nucleate ice at temperatures between -30 °C up to -15 °C (Möhler et al., 2006; Niemand et al., 2012). Biological particles such as *Pseudomonas* Syringae are known to be able to nucleate ice at temperatures as high as -2 °C (Turner et al., 1990). Studies attempting to

understand biological particles' role in the atmosphere are old and numerous (Christner et al., 2008; Du et al., 2017; Möhler et al., 2007; Szyrmer and Zawadzki, 1997; Yankofsky et al., 1981) but their role in climate remains unconstrained (Hoose et al., 2010). Other types of potential IN are soot from biomass burning (Gorbunov et al., 2001), organic particles (Murray et al., 2010), and metals (Cziczo et al., 2009).

Heterogeneous ice nucleation can proceed via different modes (Cantrell and Heymsfield, 2005), which is another aspect adding to its complexity. The immersion mode occurs when a particle nucleates ice while immersed in the bulk of the droplet, after the particle already acted as a CCN and activated into a cloud droplet. The condensation mode occurs when a CCN particle nucleates a cloud droplet followed by the same particle nucleating ice during the water condensational growth process. The condensation and immersion modes can be classified as a single mode since they both induce freezing from the bulk of the droplet (Murray et al., 2012). The deposition mode occurs when ice crystal nucleates directly on the surface of a particle from the water vapor phase. And finally, the contact mode occurs when a particle causes freezing upon contact with the surface of the droplet. It remains unclear if any single mode dominates in the atmosphere, or a combination of modes contribute to ice nucleation (Lohmann, 2002). It is nearly established that the immersion mode is more efficient than the deposition mode, since the latter does require a lager energy barrier to be overcome (Barahona, 2012). The deposition mode is also somewhat irrelevant to mixed phase clouds since particles would activate into water droplets before they have the chance to freeze into ice (Murray et al., 2012). However, the deposition mode can play an important role in cold cirrus clouds occurring where it competes with homogenous freezing (Barahona and Nenes, 2008; Möhler et al., 2006). Measurements dating back to the 1970s give evidence that the contact mode is more efficient than the immersion mode (Gokhale and Spengler, 1972; Ladino et al., 2013). The

hypothesis however remains in question due to the challenges of properly simulating the contact mode in the laboratory (Ladino et al., 2011). It can therefore be concluded that the multi-modal nature of heterogonous ice nucleation is another dimension of uncertainty regarding its role in clouds and climate.

1.2 Ice nucleation measurement methods

Difficulties in conducting systematic and reliable measurements of IN is the leading cause for our lagging state of knowledge (DeMott et al., 2011; Hiranuma et al., 2015; Verlinde et al., 2007). Field measurements, in which the ability of atmospheric particles to nucleate ice are measured from the ground and air, have shed light on many important features of atmospheric IN (Creamean et al., 2013; DeMott et al., 2003; Prather et al., 2013; Pratt et al., 2009). However, *in situ* detection of IN requires advanced single particle analysis, an active and complex area of research within itself (Baustian et al., 2012; Creamean et al., 2013; Prather et al., 2013; Sullivan and Prather, 2005). Analysis of collected precipitation samples allows measurement of the freezing temperatures of the melted precipitation particles, but the method is examining bulk freezing properties and not those of individual IN (Petters and Wright, 2015). Controlled laboratory measurements can isolate various materials and examine their ice nucleation properties however the methods there are similarly limiting (Emersic et al., 2015; Hiranuma et al., 2015). Leading laboratory measurement techniques for the immersion mode can be classified as dry dispersion or wet dispersion methods. Dry dispersion techniques aerosolize particles then probe their freezing properties with a continuous flow ice nucleation chamber, or cloud expansion chamber (DeMott et al., 2015; Hartmann et al., 2011). On the other hand, wet dispersion methods prepare a suspension of the particle material being investigated in water, generate droplets from the suspension, and examine their freezing behavior on a cold plate. Due to the differences in sample

size the two methods can confidently examine different temperature ranges which may seem complimentary but makes comparing and validating the methods against each other challenging and places large uncertainties on the validity of a coherent theory or parametrization of heterogonous ice nucleation (Hiranuma et al., 2015; Wex et al., 2015).

Measurements of the contact freezing mode of ice nucleation present a more significant challenge compared to the immersion mode (Ladino et al., 2013). Proper determination of the freezing properties of particles in this mode requires accurate retrievals of the collision frequency of atmospherically relevant sized particles (hundreds of nanometers) with a cloud relevant sized droplet (10s of microns). While it could be argued that immersion freezing is independent of droplet size as crystallization is occurring within the droplet bulk, the occurrence of contact freezing at the droplet surface may give some role to the size dependent droplet surface free energy (Djikaev et al., 2002; Djikaev and Ruckenstein, 2008). This means a cloud relevant droplet size should be a necessary design feature of a contact freezing measurements technique. Measurements dating back to the 1960s have attempted to probe contact freezing using either a cold plate (Gokhale and Goold, 1968) or a wind tunnel (Gokhale and Spengler, 1972; Pitter and Pruppacher, 1973). However both these primitive approaches used very large water drops (hundreds of microns to a few mm's in size) and needed to estimate the collision frequency. Meyers et al. (1992) pointed out that contact freezing parametrizations derived from these older measurements produced unrealistically high freezing efficiencies (ratio of collisions leading to droplet freezing to total number of collisions) validating skepticism towards their atmospheric relevance. The last few years have experienced a good deal of improvement in contact freezing measurements, but key limitations remain. Details of these newer methods will be discussed in a later chapter as outlined below.

1.3 Dissertation overview

This dissertation attempts to help reduce some of the uncertainty associated with heterogeneous ice nucleation with both improvements in its theoretical modelling and measurements. In Chapter 2 a new framework is developed to help interpret and understand droplet freezing temperature spectra measurements. It is hypothesized that a single particle species possesses a critical surface area, resulting in droplet freezing spectra exhibiting different freezing properties for particle surfaces below and above this critical area. It is speculated that this could be a reason for the discrepancies in derived freezing properties from the wet and dispersion measurement techniques. Chapter 3 applies this new framework to particles composed of different components, particularly mixtures of dust and biological particles. Here the robustness of the framework is further validated in its ability to describe freezing behavior dictated by more than one particle species. The work in Chapter 4 addresses the longstanding problem of the absence of reliable contact freezing measurements by developing a novel experimental system *via* a temperature controlled aerosol optical tweezers instrument. The chapter begins with a discussion of what key design features a reliable contact freezing measurement technique requires and what recent advances have been made in that regard. It is then shown that the newly developed system can trap individual cloud relevant water droplets stably and control their temperature. With the aid of surface sensitive cavity enhanced Raman spectroscopy, the system shows strong potential for real time detection of particle-droplet collisions. These capabilities can pave the way for future contact freezing experiments that comprehensively overcome all the significant hurdles to properly examining this mode.

References

Andreae, M. O. and Rosenfeld, D.: Aerosol–cloud–precipitation interactions. Part 1. The nature and sources of cloud-active aerosols, Earth-Science Rev., 89(1–2), 13–41, doi:10.1016/j.earscirev.2008.03.001, 2008.

Atkinson, J. D., Murray, B. J., Woodhouse, M. T., Whale, T. F., Baustian, K. J., Carslaw, K. S., Dobbie, S., O'Sullivan, D. and Malkin, T. L.: The importance of feldspar for ice nucleation by mineral dust in mixed-phase clouds, Nature, 498(7454), 355–358, doi:10.1038/nature12278, 2013.

Baker, M. B.: Cloud Microphysics and Climate, Science (80-.)., 276(5315), 1072–1078, doi:10.1126/science.276.5315.1072, 1997.

Baker, M. B. and Peter, T.: Small-scale cloud processes and climate., Nature, 451(7176), 299–300, doi:10.1038/nature06594, 2008.

Barahona, D.: On the ice nucleation spectrum, Atmos. Chem. Phys., 12(8), 3733–3752, doi:10.5194/acp-12-3733-2012, 2012.

Barahona, D. and Nenes, A.: Parameterization of cirrus cloud formation in large-scale models: Homogeneous nucleation, J. Geophys. Res., 113(D11), D11211, doi:10.1029/2007JD009355, 2008.

Baustian, K. J., Cziczo, D. J., Wise, M. E., Pratt, K. A., Kulkarni, G., Hallar, A. G. and Tolbert, M. A.: Importance of aerosol composition, mixing state, and morphology for heterogeneous ice nucleation: A combined field and laboratory approach, J. Geophys. Res. Atmos., 117(D6), doi:10.1029/2011JD016784, 2012.

Bhattu, D. and Tripathi, S. N.: CCN closure study: Effects of aerosol chemical composition and mixing state, J. Geophys. Res. Atmos., 120(2), 766–783, doi:10.1002/2014JD021978, 2015.

Boucher, O., Randall, D., Artaxo, P., Bretherton, C., Feingold, G., Forster, P., Kerminen, V.-M. V.-M., Kondo, Y., Liao, H., Lohmann, U., Rasch, P., Satheesh, S. K., Sherwood, S., Stevens, B., Zhang, X. Y. and Zhan, X. Y.: Clouds and Aerosols, Clim. Chang. 2013 Phys. Sci. Basis. Contrib. Work. Gr. I to Fifth Assess. Rep. Intergov. Panel Clim. Chang., 571–657, 2013.

Cantrell, W. and Heymsfield, A.: Production of Ice in Tropospheric Clouds: A Review, Bull. Am. Meteorol. Soc., 86(6), 795–807, doi:10.1175/BAMS-86-6-795, 2005.

Christner, B. C., Morris, C. E., Foreman, C. M., Cai, R. and Sands, D. C.: Ubiquity of Biological Ice Nucleators in Snowfall, Science (80-.)., 319(5867), 1214–1214, doi:10.1126/science.1149757, 2008.

Creamean, J. M., Suski, K. J., Rosenfeld, D., Cazorla, A., DeMott, P. J., Sullivan, R. C., White, A. B., Ralph, F. M., Minnis, P., Comstock, J. M., Tomlinson, J. M. and Prather, K. a: Dust and biological aerosols from the Sahara and Asia influence precipitation in the western U.S., Science,

339(6127), 1572–8, doi:10.1126/science.1227279, 2013.

Cziczo, D. J., Stetzer, O., Worringen, A., Ebert, M., Weinbruch, S., Kamphus, M., Gallavardin, S. J., Curtius, J., Borrmann, S., Froyd, K. D., Mertes, S., Möhler, O. and Lohmann, U.: Inadvertent climate modification due to anthropogenic lead, Nat. Geosci., 2(5), 333–336, doi:10.1038/ngeo499, 2009.

DeMott, P. J., Cziczo, D. J., Prenni, A. J., Murphy, D. M., Kreidenweis, S. M., Thomson, D. S., Borys, R. and Rogers, D. C.: Measurements of the concentration and composition of nuclei for cirrus formation., Proc. Natl. Acad. Sci. U. S. A., 100(25), 14655–60, doi:10.1073/pnas.2532677100, 2003.

DeMott, P. J., Prenni, A. J., Liu, X., Kreidenweis, S. M., Petters, M. D., Twohy, C. H. and Richardson, M. S.: Predicting global atmospheric ice nuclei distributions and their impacts on climate, PNAS, 107(25), 11217–11222, doi:10.1073/pnas.0910818107, 2010.

DeMott, P. J., Möhler, O., Stetzer, O., Vali, G., Levin, Z., Petters, M. D., Murakami, M., Leisner, T., Bundke, U., Klein, H., Kanji, Z. A., Cotton, R., Jones, H., Benz, S., Brinkmann, M., Rzesanke, D., Saathoff, H., Nicolet, M., Saito, A., Nillius, B., Bingemer, H., Abbatt, J., Ardon, K., Ganor, E., Georgakopoulos, D. G. and Saunders, C.: Resurgence in Ice Nuclei Measurement Research, Bull. Am. Meteorol. Soc., 92(12), 1623–1635, doi:10.1175/2011BAMS3119.1, 2011.

DeMott, P. J., Prenni, A. J., McMeeking, G. R., Sullivan, R. C., Petters, M. D., Tobo, Y., Niemand, M., Möhler, O., Snider, J. R., Wang, Z. and Kreidenweis, S. M.: Integrating laboratory and field data to quantify the immersion freezing ice nucleation activity of mineral dust particles, Atmos. Chem. Phys., 15(1), 393–409, doi:10.5194/acp-15-393-2015, 2015.

Djikaev, Y. S. and Ruckenstein, E.: Thermodynamics of Heterogeneous Crystal Nucleation in Contact and Immersion Modes, J. Phys. Chem. A, 112(46), 11677–11687, doi:10.1021/jp803155f, 2008.

Djikaev, Y. S., Tabazadeh, a., Hamill, P. and Reiss, H.: Thermodynamic Conditions for the Surface-Stimulated Crystallization of Atmospheric Droplets, J. Phys. Chem. A, 106(43), 10247–10253, doi:10.1021/jp021044s, 2002.

Du, R., Du, P., Lu, Z., Ren, W., Liang, Z., Qin, S., Li, Z., Wang, Y. and Fu, P.: Evidence for a missing source of efficient ice nuclei, Sci. Rep., 7, 39673, doi:10.1038/srep39673, 2017.

Edwards, G. ., Evans, L. . and La Mer, V. .: Ice nucleation by monodisperse silver iodide particles, J. Colloid Sci., 17(8), 749–758, doi:org/10.1016/0095-8522(62)90049-1, 1962.

Emersic, C., Connolly, P. J., Boult, S., Campana, M. and Li, Z.: Investigating the discrepancy between wet suspension and dry-dispersion derived ice nucleation efficiency of mineral particles, Atmos. Chem. Phys., 15(19), 11311–11326, doi:10.5194/acp-15-11311-2015, 2015.

Ervens, B., Feingold, G., Sulia, K. and Harrington, J.: The impact of microphysical parameters, ice nucleation mode, and habit growth on the ice/liquid partitioning in mixed-phase Arctic clouds, J. Geophys. Res., 116(D17), D17205, doi:10.1029/2011JD015729, 2011.

Fletcher, N. H.: Active Sites and Ice Crystal Nucleation, J. Atmos. Sci., 26(6), 1266–1271, doi:10.1175/1520-0469(1969)026<1266:ASAICN>2.0.CO;2, 1969.

Fraux, G. and Doye, J. P. K.: Note: Heterogeneous ice nucleation on silver-iodide-like surfaces, J. Chem. Phys., 141(21), doi:org/10.1063/1.4902382, 2014.

Gettelman, A., Liu, X., Barahona, D., Lohmann, U. and Chen, C.: Climate impacts of ice nucleation, J. Geophys. Res., 117(D20), doi:10.1029/2012JD017950, 2012.

Gokhale, N. R. and Goold, J.: Droplet Freezing by Surface Nucleation, J. Appl. Meteorol., 7(5), 870–874, doi:10.1175/1520-0450(1968)007<0870:DFBSN>2.0.CO;2, 1968.

Gokhale, N. R. and Spengler, J. D.: Freezing of Freely Suspended, Supercooled Water Drops by Contact Nucleation, J. Appl. Meteorol., 11(1), 157–160, doi:10.1175/1520-0450(1972)011<0157:FOFSSW>2.0.CO;2, 1972.

Gorbunov, B., Baklanov, A., Kakutkina, N., Windsor, H. . and Toumi, R.: Ice nucleation on soot particles, J. Aerosol Sci., 32(2), 199–215, doi:10.1016/S0021-8502(00)00077-X, 2001.

Hartmann, S., Niedermeier, D., Voigtländer, J., Clauss, T., Shaw, R. a., Wex, H., Kiselev, A. and Stratmann, F.: Homogeneous and heterogeneous ice nucleation at LACIS: operating principle and theoretical studies, Atmos. Chem. Phys., 11(4), 1753–1767, doi:10.5194/acp-11-1753-2011, 2011.

Heintzenberg, J. and Charlson, R. J.: Clouds in the Perturbed Climate System., 2009.

Hewitt, C. N. and Jackson, A. V.: Handbook of Atmospheric Science: Principles and Applications, wiley., 2007.

Hiranuma, N., Augustin-Bauditz, S., Bingemer, H., Budke, C., Curtius, J., Danielczok, A., Diehl, K., Dreischmeier, K., Ebert, M., Frank, F., Hoffmann, N., Kandler, K., Kiselev, A., Koop, T., Leisner, T., Möhler, O., Nillius, B., Peckhaus, A., Rose, D., Weinbruch, S., Wex, H., Boose, Y., DeMott, P. J., Hader, J. D., Hill, T. C. J., Kanji, Z. A., Kulkarni, G., Levin, E. J. T., McCluskey, C. S., Murakami, M., Murray, B. J., Niedermeier, D., Petters, M. D., O'Sullivan, D., Saito, A., Schill, G. P., Tajiri, T., Tolbert, M. A., Welti, A., Whale, T. F., Wright, T. P. and Yamashita, K.: A comprehensive laboratory study on the immersion freezing behavior of illite NX particles: a comparison of 17 ice nucleation measurement techniques, Atmos. Chem. Phys., 15(5), 2489–2518, doi:10.5194/acp-15-2489-2015, 2015.

Hoose, C., Kristjánsson, J. E. and Burrows, S. M.: How important is biological ice nucleation in clouds on a global scale?, Environ. Res. Lett., 5(2), 24009, doi:10.1088/1748-9326/5/2/024009, 2010.

Houze, R. A.: Cloud dynamics., 1993.

Knopf, D. A. and Koop, T.: Heterogeneous nucleation of ice on surrogates of mineral dust, J. Geophys. Res., 111(D12), D12201, doi:10.1029/2005JD006894, 2006.

Ladino, L., Stetzer, O., Lüönd, F., Welti, A. and Lohmann, U.: Contact freezing experiments of kaolinite particles with cloud droplets, J. Geophys. Res., 116(January), 1–12, doi:10.1029/2011JD015727, 2011.

Ladino Moreno, L. A., Stetzer, O. and Lohmann, U.: Contact freezing: a review of experimental studies, Atmos. Chem. Phys., 13(19), 9745–9769, doi:10.5194/acp-13-9745-2013, 2013.

Lohmann, U.: Possible Aerosol Effects on Ice Clouds via Contact Nucleation, J. Atmos. Sci., 59(3), 647–656, doi:http://dx.doi.org/10.1175/1520-0469(2001)059<0647:PAEOIC>2.0.CO;2, 2002.

Lohmann, U. and Feichter, J.: Global indirect aerosol effects: a review, Atmos. Chem. Phys. Discuss., 4(6), 7561–7614, doi: 10.5194/acp-5-715-2005, 2004.

Lohmann, U. and Lesins, G.: Stronger Constraints on the Anthropogenic Indirect Aerosol Effect, Science (80-.)., 298(5595), 1012–1015, doi:10.1126/science.1075405, 2002.

Meyers, M. P., DeMott, P. J. and Cotton, W. R.: New Primary Ice-Nucleation Parameterizations in an Explicit Cloud Model, J. Appl. Meteorol., 31(7), 708–721, doi:10.1175/1520-0450(1992)031<0708:NPINPI>2.0.CO;2, 1992.

Möhler, O., Field, P. R., Connolly, P., Benz, S., Saathoff, H., Schnaiter, M., Wagner, R., Cotton, R., Krämer, M., Mangold, A. and Heymsfield, A. J.: Efficiency of the deposition mode ice nucleation on mineral dust particles, Atmos. Chem. Phys., 6(10), 3007–3021, doi:10.5194/acp-6-3007-2006, 2006.

Möhler, O., DeMott, P. J., Vali, G. and Levin, Z.: Microbiology and atmospheric processes: the role of biological particles in cloud physics, Biogeosciences Discuss., 4(4), 2559–2591, doi:hal-00297909, 2007.

Mülmenstädt, J., Sourdeval, O., Delanoë, J. and Quaas, J.: Frequency of occurrence of rain from liquid-, mixed-, and ice-phase clouds derived from A-Train satellite retrievals, Geophys. Res. Lett., 42(15), 6502–6509, doi:10.1002/2015GL064604, 2015.

Murray, B. J., Wilson, T. W., Dobbie, S., Cui, Z., Al-Jumur, S. M. R. K., Möhler, O., Schnaiter, M., Wagner, R., Benz, S., Niemand, M., Saathoff, H., Ebert, V., Wagner, S. and Kärcher, B.: Heterogeneous nucleation of ice particles on glassy aerosols under cirrus conditions, Nat. Geosci., 3(4), 233–237, doi:10.1038/ngeo817, 2010.

Murray, B. J., O'Sullivan, D., Atkinson, J. D. and Webb, M. E.: Ice nucleation by particles immersed in supercooled cloud droplets, Chem. Soc. Rev., 41(19), 6519, doi:10.1039/c2cs35200a, 2012.

Niemand, M., Möhler, O., Vogel, B., Vogel, H., Hoose, C., Connolly, P., Klein, H., Bingemer, H., DeMott, P., Skrotzki, J. and Leisner, T.: A Particle-Surface-Area-Based Parameterization of Immersion Freezing on Desert Dust Particles, J. Atmos. Sci., 69, 3077–3092, doi:org/10.1175/JAS-D-11-0249.1, 2012.

Petters, M. D. and Kreidenweis, S. M.: A single parameter representation of hygroscopic growth and cloud condensation nucleus activity, Atmos. Chem. Phys., 7(8), 1961–1971, doi:10.5194/acp-7-1961-2007, 2007.

Petters, M. D. and Wright, T. P.: Revisiting ice nucleation from precipitation samples, Geophys. Res. Lett., 42(20), 8758–8766, doi:10.1002/2015GL065733, 2015.

Pilinis, C., Pandis, S. N. and Seinfeld, J. H.: Sensitivity of direct climate forcing by atmospheric aerosols to aerosol size and composition, J. Geophys. Res., 100(D9), 18739, doi:10.1029/95JD02119, 1995.

Pitter, R. L. and Pruppacher, H. R.: A wind tunnel investigation of freezing of small water drops falling at terminal velocity in air, Q. J. R. Meteorol. Soc., 99(421), 540–550, doi:10.1002/qj.49709942111, 1973.

Prather, K. a, Bertram, T. H., Grassian, V. H., Deane, G. B., Stokes, M. D., Demott, P. J., Aluwihare, L. I., Palenik, B. P., Azam, F., Seinfeld, J. H., Moffet, R. C., Molina, M. J., Cappa, C. D., Geiger, F. M., Roberts, G. C., Russell, L. M., Ault, A. P., Baltrusaitis, J., Collins, D. B., Corrigan, C. E., Cuadra-Rodriguez, L. a, Ebben, C. J., Forestieri, S. D., Guasco, T. L., Hersey, S. P., Kim, M. J., Lambert, W. F., Modini, R. L., Mui, W., Pedler, B. E., Ruppel, M. J., Ryder, O. S., Schoepp, N. G., Sullivan, R. C. and Zhao, D.: Bringing the ocean into the laboratory to probe the chemical complexity of sea spray aerosol., Proc. Natl. Acad. Sci. U. S. A., 110(19), 7550–5, doi:10.1073/pnas.1300262110, 2013.

Pratt, K. a., DeMott, P. J., French, J. R., Wang, Z., Westphal, D. L., Heymsfield, A. J., Twohy, C. H., Prenni, A. J. and Prather, K. a.: In situ detection of biological particles in cloud ice-crystals, Nat. Geosci., 2(6), 398–401, doi: org/10.1038/ngeo521, 2009.

Pruppacher, H. R. and Klett, J. D.: Microphysics of Clouds and Precipitation, edited by R. D. Rosen, Kluwer Academic Publishers., 1997.

Quante, M.: The role of clouds in the climate system, J. Phys. IV, 121, 61–86 doi: org/10.1051/jp4:2004121003, 2004.

Rosenfeld, D., Lohmann, U., Raga, G. B., O'Dowd, C. D., Kulmala, M., Fuzzi, S., Reissell, A. and Andreae, M. O.: Flood or Drought: How Do Aerosols Affect Precipitation?, Science (80-.)., 321(5894), 1309–1313, doi:10.1126/science.1160606, 2008.

Rosenfeld, D., Chemke, R., DeMott, P., Sullivan, R. C., Rasmussen, R., McDonough, F., Comstock, J., Schmid, B., Tomlinson, J., Jonsson, H., Suski, K., Cazorla, A. and Prather, K.: The common occurrence of highly supercooled drizzle and rain near the coastal regions of the Western United States, J. Geophys. Res. Atmos., 118, doi:10.1002/jgrd.50529, 2013.

Storelvmo, T., Tan, I. and Korolev, A. V.: Cloud Phase Changes Induced by CO2 Warming—a Powerful yet Poorly Constrained Cloud-Climate Feedback, Curr. Clim. Chang. Reports, 1(4), 288–296, doi:10.1007/s40641-015-0026-2, 2015.

Sullivan, R. C. and Prather, K. A.: Recent Advances in Our Understanding of Atmospheric

Chemistry and Climate Made Possible by On-Line Aerosol Analysis Instrumentation, Anal. Chem., 77(12), 3861–3886, doi:10.1021/ac050716i, 2005.

Szyrmer, W. and Zawadzki, I.: Biogenic and Anthropogenic Sources of Ice-Forming Nuclei: A Review, Bull. Am. Meteorol. Soc., 78(2), 209–228, doi:org/10.1175/1520-0477(1997)078<0209:BAASOI>2.0.CO;2, 1997.

Tan, I., Storelvmo, T. and Zelinka, M. D.: Observational constraints on mixed-phase clouds imply higher climate sensitivity, Science (80-.)., 352(6282), 224–227, doi:10.1126/science.aad5300, 2016.

Turner, M. A., Arellano, F. and Kozloff, L. M.: Three separate classes of bacterial ice nucleation structures, J. Bacteriol., 172(5), 2521–2526, doi:PMC208892, 1990.

Vali, G.: Ice Nucleation - a Review, PoLAR, 271–279, 1996.

Vali, G., DeMott, P. J., Möhler, O. and Whale, T. F.: Technical Note: A proposal for ice nucleation terminology, Atmos. Chem. Phys., 15(18), 10263–10270, doi:10.5194/acp-15-10263-2015, 2015.

Verlinde, J., Harrington, J. Y., Yannuzzi, V. T., Avramov, a., Greenberg, S., Richardson, S. J., Bahrmann, C. P., McFarquhar, G. M., Zhang, G., Johnson, N., Poellot, M. R., Mather, J. H., Turner, D. D., Eloranta, E. W., Tobin, D. C., Holz, R., Zak, B. D., Ivey, M. D., Prenni, a. J., DeMott, P. J., Daniel, J. S., Kok, G. L., Sassen, K., Spangenberg, D., Minnis, P., Tooman, T. P., Shupe, M., Heymsfield, a. J. and Schofield, R.: The Mixed-Phase Arctic Cloud Experiment, Bull. Am. Meteorol. Soc., 88(2), 205–221, doi:10.1175/BAMS-88-2-205, 2007.

Vonnegut, B.: The nucleation of ice formation by silver iodide, J. Appl. Phys., 18(7), 593–595, 1947.

Wex, H., Augustin-Bauditz, S., Boose, Y., Budke, C., Curtius, J., Diehl, K., Dreyer, a., Frank, F., Hartmann, S., Hiranuma, N., Jantsch, E., Kanji, Z. a., Kiselev, a., Koop, T., Möhler, O., Niedermeier, D., Nillius, B., Rösch, M., Rose, D., Schmidt, C., Steinke, I. and Stratmann, F.: Intercomparing different devices for the investigation of ice nucleating particles using Snomax® as test substance, Atmos. Chem. Phys., 15(3), 1463–1485, doi:10.5194/acp-15-1463-2015, 2015.

Yankofsky, S. a., Levin, Z., Bertold, T. and Sandlerman, N.: Some Basic Characteristics of Bacterial Freezing Nuclei, J. Appl. Meteorol., 20(9), 1013–1019, doi:10.1175/1520-0450(1981)020<1013:SBCOBF>2.0.CO;2, 1981.

Chapter 2: The critical area hypothesis and the development of a new heterogeneous ice nucleation framework

The texts and figures of this chapter are a reprint of the following publication where I was the primary researcher and author:

Beydoun, H., Polen, M. and Sullivan, R. C.: Effect of particle surface area on ice active site densities retrieved from droplet freezing spectra, Atmos. Chem. Phys., 16(20), 13359–13378, doi:10.5194/acp-16-13359-2016, 2016.

Abstract

In this chapter we formulate an ice active surface site based stochastic model of heterogeneous freezing with the unique feature of invoking a continuum assumption on the ice nucleating activity (contact angle) of an aerosol particle's surface, that requires no assumptions about the size or number of active sites. The result is a particle specific property g that defines a distribution of local ice nucleation rates. Upon integration this yields a full freezing probability function for an ice nucleating particle.

Current cold plate droplet freezing measurements provide a valuable and inexpensive resource for studying the freezing properties of many atmospheric aerosol systems. We apply our g framework to explain the observed dependence of the freezing temperature of droplets in a cold plate on the concentration of the particle species investigated. Normalizing to the total particle mass or surface area present to derive the commonly used ice nuclei active surface (INAS) density (n_s) often cannot account for the effects of particle concentration, yet concentration is typically varied to span a wider measureable freezing temperature range. A method based on determining what is denoted an ice nucleating species' specific critical surface area is presented that explains the concentration dependence as a result of increasing the variability in ice nucleating active sites

between droplets. By applying this method to experimental droplet freezing data from four different systems we demonstrate its ability to interpret immersion freezing temperature spectra of droplets containing variable particle concentrations.

It is shown that general active site density functions such as the popular n_s parameterization cannot be reliably extrapolated below this critical surface area threshold to describe freezing curves for lower particle surface area concentrations. Freezing curves obtained below this threshold translate to higher n_s values, while the n_s values are essentially the same from curves obtained above the critical area threshold; n_s should remain the same for a system as concentration is varied. However, we can successfully predict the lower concentration freezing curves, which are more atmospherically relevant, through a process of random sampling from g distributions obtained from high particle concentration data. Our analysis is applied to cold plate freezing measurements of droplets containing variable concentrations of particles from NX illite minerals, MCC cellulose, and commercial Snomax bacterial particles. Parameterizations that can predict the temporal evolution of the frozen fraction of cloud droplets in larger atmospheric models are also derived from this new framework.

2.1 Introduction

There are currently two competing views on the dominant factors that control the heterogeneous ice nucleation process, the stochastic versus deterministic framework (Niedermeier et al., 2011; Vali, 2014). The stochastic framework assumes that freezing occurs with equal probability at any point across a particle's surface and can be constrained with a temperature dependent ice nucleation rate (Pruppacher and Klett, 1997). This effectively yields time dependent freezing and an element of non-repeatability (Vali, 2008). On the other hand in the deterministic framework ice nucleation is dictated by ice active surface sites (Fletcher, 1969; Levine, 1950; Meyers et al., 1992; Sear, 2013). Each active site has a characteristic critical freezing temperature, with the site with the highest critical temperature always initiating crystallization instantly (Vali, 2008). Careful examination of the experimental results published by Vali (2014) indicates that the very nature of the process need not be in contention. These results suggest that there is a strong spatial preference on where nucleation occurs, supporting a model of discrete active sites. However, variability in freezing temperatures still occurs indicating that a stochastic element also exists. Considering several decades of experimental work and theoretical considerations (Ervens and Feingold, 2013; Murray et al., 2012; Vali, 1994, 2014; Vali and Stransbury, 1966; Wright et al., 2013; Wright and Petters, 2013), the role of time has been determined to play a much weaker role than temperature does. It remains to be seen whether the difference is significant enough for time-dependent freezing to be completely omitted in atmospheric models.

The debate over how to properly parameterize heterogeneous ice nucleation has important implications on how freezing processes are represented in atmospheric models (Hoose et al., 2010a; Hoose and Möhler, 2012; Koop et al., 2000; Phillips et al., 2008, 2013), and also reflects our fundamental understanding of this nucleation process. Ervens & Feingold (2012) tested

different nucleation schemes in an adiabatic parcel model and found that critical cloud features such as the initiation of the WBF process, liquid water content, and ice water content, all diverged for the different ice nucleation parameterizations. This strongly affected cloud evolution and lifetime. The divergence was even stronger when the aerosol size distribution was switched from monodisperse to polydisperse. Similar sensitivities of adiabatic parcel models to time dependent freezing were shown in Wright and Petters (2013) and Vali and Snider (2015).

A new parameterization, starting from classical nucleation theory, is formulated in this paper. The new framework is stochastic by nature to properly reflect the randomness of ice embryo growth and dissolution, and assumes that an ice nucleating particle can exhibit variability in active sites along its surface, what will be referred to as internal variability, and variability in active sites between other particles of the same species, what will be referred to as external variability. A new method is presented to analyze and interpret experimental data from the ubiquitous droplet freezing cold plate method using this framework, and parameterize these experimental results for use in cloud parcel models. New insights into the proper design of cold plate experiments and the analysis of their immersion freezing datasets to accurately describe the behavior of atmospheric ice nucleating particles are revealed. Based on experimental observations and the new framework we argue that active site schemes that assume uniform active site density such as the popular n_s parameterization – a deterministic framework that assigns an active site density as a function of temperature (Hoose et al., 2008; Vali, 1971) – are unable to consistently describe freezing curves over a wide surface area range. This shortcoming is argued to be one of the causes of the discrepancies in retrieved n_s values of the same ice nucleating species using different measurement methods and particle in droplet concentrations (Emersic et al., 2015; Hiranuma et al., 2015a; Wex et al., 2015).

2.2 Classical nucleation theory

Ice nucleation is a fundamentally stochastic process brought about by the random formation, growth, and dissolution of critically sized ice germs that overcome the energy barrier associated with the phase transition (Pruppacher and Klett, 1997; Vali and Stransbury, 1966). A homogenous ice nucleation rate for a given volume of supercooled water can therefore be defined from a Boltzmann type formulation:

$$J(T) = C\exp\left(-\frac{\Delta G}{kT}\right) \qquad (1)$$

where J is the ice nucleation rate and has units of freezing events/(time × volume). ΔG is the energy barrier to crystallization from liquid water as defined in Pruppacher & Klett (1997) and Zobrist et al. (2007). T is temperature, k the Boltzmann constant, and C is a constant. For typical cloud droplet volumes, a temperature of about -38 °C is typically required for the homogeneous ice nucleation rate to become significantly fast such that freezing occurs within minutes or less. At temperatures between -38 and 0 °C a catalyst is required to initiate freezing of cloud droplets. Certain rare aerosol particles – ice nucleating particles – can act as these catalysts and induce heterogeneous ice nucleation in the atmosphere.

In expanding to heterogeneous ice nucleation the simplest approach is to assume that instead of ice germ formation occurring randomly throughout a bulk volume of supercooled water, ice nucleation is initiated on a surface. The surface reduces the nucleation energy barrier ΔG by a factor f, dependent on the contact angle between liquid water and the material. The contact angle θ $[0, \pi]$ is actually a proxy for the water-surface interaction system, with smaller values of θ indicating that the surface is a better nucleant. The surface's measured water contact angle cannot

actually be simply used to predict its ice nucleation efficiency. The extreme limit of a contact angle of 0° is therefore a perfect ice nucleant, diminishing the energy barrier fully and immediately inducing freezing at the thermodynamic freezing point of water at 0 °C. The heterogeneous ice nucleation rate for a volume of water containing a total surface area of ice nucleating particles (INP) therefore can be defined as (Pruppacher and Klett, 1997):

$$J(T) = C\exp\left(-\frac{f(\theta)\Delta G}{kT}\right) \qquad (2)$$

where J in this case would be expressed as freezing events/(time × surface area).

The simplest stochastic formulation hypothesizes that the nucleation rate is uniform across the ice nucleating particle's surface, i.e. makes a single contact angle assumption. For a large statistical ensemble of droplet-INP pairings the number of frozen droplets after some time t resembles a first order chemical decay (Pruppacher and Klett, 1997):

$$N_f(T,t) = N(1 - \exp(-J(T)At)) \qquad (3)$$

where N_f is the fraction of droplets frozen after time t at temperature T, N is the total number of particle-droplet pairings and A is the surface area of each individual ice nucleating particle (assumed to be the same for all particles). Furthermore, a probability of ice nucleation, P_f, at the single droplet-particle level can be defined as:

$$P_f = 1 - \exp(-JAt) \qquad (4)$$

2.3 Formulation of g: a continuum approach of active site activity to describe heterogeneous ice nucleation

Given the large variability in particle surface composition and structure across any one particle, which in turn determines the activity (or contact angle, θ) of a potential ice nucleating site, a different approach is to assume that the heterogonous nucleation rate will vary along the particle-droplet interface. Since the critical nucleation area (~nm^2) is much smaller than the total particle area (~μm^2), we apply a continuum assumption for the ice active site activity (θ) available across a particle's surface without assumptions about the size or number of active sites per particle surface area. The new resulting probability of freezing is:

$$P_f = 1 - \exp\left(-t \int J \, dA\right) \qquad (5)$$

where J is now a freezing rate that is allowed to vary for each specific small segment of the particle's surface area, dA. To define the freezing probability as a function of a contact angle distribution, the surface integral (Eq. 5) is transformed into a line integral via the newly defined g parameter and normalized to the total available surface area:

$$g(\theta) = \frac{1}{A}\frac{dA}{d\theta} \qquad (6)$$

and the freezing probability for a droplet-particle pair becomes:

$$P_f = 1 - \exp\left(-tA \int_0^{\pi} J(\theta) g(\theta) d\theta\right) \qquad (7)$$

g is a probability density function describing the continuous active site density of the ice nucleating particle's surface. This is the first use of a continuum description of ice nucleating activity to describe the freezing behavior of an individual particle to our knowledge. Some key unique features of our approach are that the number or size of the individual active sites do not have to be assumed or retrieved in order to predict the freezing probabilities. The causes of these unique features in our framework and the choice of a normal distribution for the contact angle will be explored and justified in a following section.

In this work the *internal* variability of an individual ice nucleating particle expresses the heterogeneity of its ice nucleating surface. A wider (larger σ) g distribution describes a greater particle internal variability of ice active surface site properties or contact angles present on that one particle. This is in contrast to the *external* variability of an ice nucleating species or type, which expresses how diverse a population of particles is in their ice nucleation activities. External variability accounts for differences in the g distributions of individual particles between particles of the same type (such as particles composed of the same mineral phases).

We hypothesize that experimentally probed systems can be interpreted as exhibiting internal and external variability based on differences in freezing temperatures of different droplets containing the same material, i.e. the freezing temperature spectrum of a droplet array. The model will be shown to provide a conceptual explanation of what this variability, be it internal or external, stems from. We provide this as a potential explanation for discrepancies in the measured values of the popular deterministic scheme n_s (Hoose and Möhler, 2012; Vali, 2014) for different particle concentrations and consequently different measurements methods. In the following sections the model is developed further to shed light on the impact of the g distribution on time dependent

freezing, the contrasting internally and externally variable nature of a species' ice nucleating activity, and the dependence of g on particle size.

2.4 Internal variability and its impact on time dependent freezing

To explore the importance of accounting for ice nucleating variability along a single particle's surface (internal variability) we examined the temperature dependent freezing curves of droplets with single large ash particles immersed in them from Fornea et al. (2009). Their experiments were performed with cooling rates of 1 °C/min. Figure 2.1 displays their experimental data (red dots), a single contact angle (θ) fit to their data (red solid line) that assumes no internal variability, and a g distribution fit using multiple θ'*s* (solid blue line) that allows for internal variability. Fornea et al. retrieved their experimental data points by averaging the observed freezing temperature of the same ash particle-droplet pair after multiple freezing cycles. The averaged values are denoted freezing probabilities since they represent the chance of freezing occurring at that temperature. The ash particle diameter was around 300 μm, clearly much larger than atmospheric particle sizes. Five different particle samples of Mount St. Helens Ash were probed in the study; the one that exhibited the broadest range of freezing temperature was chosen for the examination conducted in this section.

To fit a g distribution to an empirical freezing curve, a least square error approach is implemented. A matrix of freezing probabilities is generated for all possible g distributions. If the experimental freezing curve has been retrieved from experiments in which the temperature is dictated by a non-constant cooling rate, an expression that satisfies this condition must be used:

$$P_f = 1 - \exp\left(-A \int_0^t \int_0^\pi J(T(t), \theta) g(\theta) d\theta dt\right) \qquad (8)$$

In equation (8) J is a function of time because temperature varies with time. If the cooling rate $\dot{T}$ is constant, a simple change of variable can be applied:

$$P_f = 1 - \exp\left(-\frac{A}{\dot{T}} \int_{T_i}^{T_f} \int_0^\pi J(T, \theta) g(\theta) d\theta dT\right) \qquad (9)$$

Equation (9) is therefore used to fit the constant cooling rate dataset from Fornea et al. (2009) considered here as well as datasets considered later in the paper. $J(T, \theta)$ is evaluated using CNT parameters presented in Zobrist et al. (2007).

The g fit performs much better in capturing the behavior of the observed freezing temperature spectrum in Fig. 2.1, as expected given the greater degrees of freedom allowed for the multiple θ fit. The single θ fit has a steeper dependence on temperature; the double exponential temperature dependence of the freezing probability in Eq. (4) (J is an exponential function of temperature in itself as can be seen in Eq. (2)) results in an approximately temperature step function. The diversity of nucleating ability on the particle surface captured by the g parameter offsets some of the steepness and yields a more gradual freezing curve, more similar to the actual experimental freezing probability curve.

Two droplet freezing probability fits (dotted lines) are also plotted in Fig. 2.1 using the single and multiple θ fits but with a larger cooling rate of 10 K/min. One fit uses the same g distribution used previously, while the additional single θ fit is approximated as a normal distribution with a

near zero standard deviation, similar to a Delta Dirac function. The resultant freezing probabilities are then computed and plotted for every T using Eq. (9). It can be seen that the g fit retains much stronger cooling rate dependence, with the g freezing probability curve shifting about 2 K colder and the single θ curve shifting just 0.5 K colder for the faster 10 K/min cooling rate. The 2 K prediction presented here is still smaller than the one retrieved experimentally by Fornea et al. (2009) for varying the cooling rate from 1 K/min to 10 K/min, which was measured to be 3.6 K. However, it is unclear which of the samples presented in their work corresponds to this change in median freezing temperature as it is only mentioned as an average decrease in temperature for all of the different samples tested.

This numerical exercise shows that wider g distributions theoretically yield stronger time dependence due to the partial offset of the strong temperature dependence that the nucleation rate in Eq. (2) exhibits. The result emphasizes that how the active sites are modeled has consequences on what physical parameters (e.g. time, temperature, cooling rate) can influence the freezing outcome and predicted droplet freezing temperature

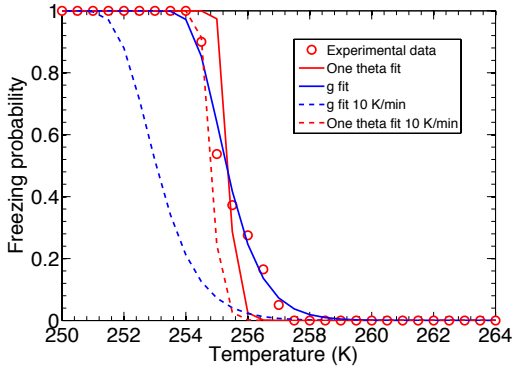

Figure 2.1. Experimentally determined freezing probabilities and fits from freezing of a droplet containing a single large ~300 μm diameter volcanic ash particle, from Fornea et al. (2009). Red

dots are experimental freezing probabilities retrieved from repeated droplet freezing measurements. The red line is a fit to the data using classical nucleation theory and the assumption of a single contact angle (θ). The blue line is a fit to the data using the g framework developed here, which describes a Gaussian distribution of θ. The g fit has a least square error sum of 0.0197, $\mu = 1.65$, and $\sigma = 0.135$. The dotted red line is the simulated freezing curve resulting from a single θ distribution for a simulated cooling rate of 10 K/min. The dotted blue line is the freezing curve from a multiple θ distribution described by g after the same simulated cooling rate.

spectrum (Broadley et al., 2012) and that model parameters need to be tested under different environmental conditions (e.g. different cooling rates) to properly test their validity. In Fig. 2.1 a wider g distribution resulted in a higher sensitivity to cooling rate, which resulted in a shift of the freezing curve to lower temperatures as the system was cooled at a faster rate. This significant change in the freezing probability's sensitivity to temperature is the cause of the more gradual rise in the freezing probability for the system when applying a non-Delta Dirac g distribution. This is effectively enhancing the stochastic element in the particle's ice nucleation properties. The enhancement of the stochastic element brings about a more important role for time as shown in Fig. 2.1. The finding of this exercise is consistent with previously published work on time dependent freezing such as those reported by Barahona (2012), Wright and Petters (2013), and Herbert et al. (2014) amongst others.

2.5 Defining g as a normal distribution of ice nucleation activity

The fit for a particle-freezing curve such as the one considered in the previous section (Fig. 2.1) does not have a unique solution. There are, mathematically speaking, infinite solutions for the g

distributions that produce a representative freezing curve. In any considered distribution an ascending tail with increasing contact angle represents a competition between more active but less frequent surface sites, and less active but more frequent sites. Sites with lower activity and lower frequency have essentially zero chance of contributing to the overall freezing probability, primarily due to the nucleation rate's, J, exponential dependence on the energy barrier to nucleation and the freezing probability's exponential dependence on J as shown in Eqs. (2) and (7). It is therefore sufficient to conceptualize that the particle has a well-defined monotonic spectrum of active sites increasing in frequency while decreasing in strength. The spectrum is modeled as a continuum of ice nucleation activity described by the g distribution, as depicted on the upper right hand corner in Fig. 2.2. Figure 2.2 also shows part of the g distribution (the ascending part representing the monotonic spectrum of active sites) retrieved for the case example in section 2.1 (log scale) discretized into numerical bins, where the height of each bin represents the abundance of that θ

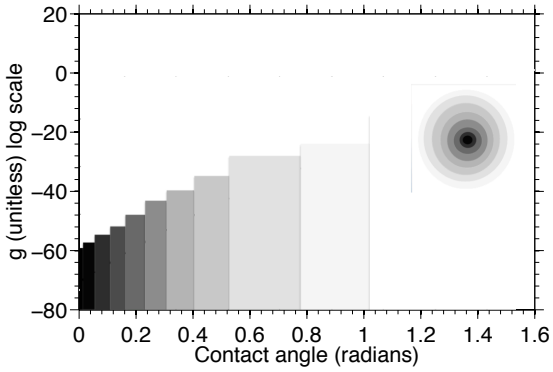

Figure 2.2. Upper right inset displays the distribution of ice nucleation activity (contact angle, θ) for a representative spectrum of a particle's ice nucleating activity. The less active (white) surface sites have more surface coverage while the more active (black) surface sites have less coverage. The probability distribution function for the g distribution ($\mu = 1.65$, and $\sigma = 0.135$, retrieved in

Section 2.2) ascent in log space is plotted with numerical bins. The darker colors are used to highlight the stronger ice nucleating activity at smaller contact angles (θ).

across the particle's surface. The area in each column thus represents the total surface area with that value of θ. As in Fig. 2's inset the darker colors are used to emphasize more active ice nucleating activity at the smaller contact angles.

The ascending part of the curve of the normal g distribution covering the smallest (most active) values of θ in Fig. 2 can therefore capture this active site model. The wider the defined g distribution (i.e. for a larger standard deviation, σ) the more diverse the considered system is in its internal variability of ice nucleation activity. Since the freezing probability is determined solely by a fraction of the ascent of the normal distribution – as this captures the rare but most active sites that determine the actual freezing rate J and freezing probability P_f – the following approximation to Eq. (9) can be made:

$$P_f = 1 - \exp\left(-\frac{A}{\dot{T}}\int_{T_i}^{T_f}\int_{0}^{\pi} J(T,\theta)g(\theta)d\theta dT\right)$$

$$\approx 1 - \exp\left(-\frac{A}{\dot{T}}\int_{T_i}^{T_f}\int_{\theta_{c_1}}^{\theta_{c_2}} J(T,\theta)g(\theta)d\theta dT\right) \qquad (10)$$

where θ_{c_1} and θ_{c_2} are the approximate cutoff points in the g distribution that contain the critical range of the most active contact angles. Outside $[\theta_{c_1}, \theta_{c_2}]$ the less active contact angles have a negligible contribution to the actual manifested freezing rate and freezing probability. The critical contact angle range is a strong function of the area of the particle.

The critical contact angles are determined numerically by identifying the range $[\theta_{c_1}, \theta_{c_2}]$ for which the freezing probability can be approximated using Eq. (10). Figure 2.3(a) illustrates the process of identifying θ_{c2}. The blue curves represent freezing probabilities computed via integrating Eq. (10) from 0 to a variable θ_{c2}. The red curve is the freezing probability computed from integrating across the full θ range. As θ_{c2} is increased the resultant curve (blue) approaches the curve computed from the full θ range (red). For the example studied in Fig. 2.3 (same system examined in Section 2.1), a value of θ_{c2} = 0.79 rad results in a least square error below 0.01 for the freezing probability retrieved from Eq. (10) assessed against the freezing probability retrieved from Eq. (9). An identical approach is followed to determine θ_{c1}.

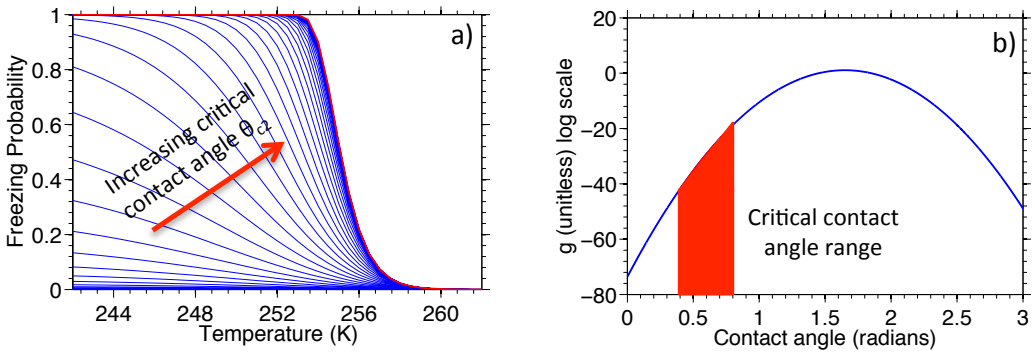

Figure 2.3. Left (a): Identifying the critical contact angle range. The thin blue curves are retrieved from application of the simplified Eq. (10), which approximates the freezing probability by integrating over a smaller contact angle range, $[\theta_{c_1}, \theta_{c_2}]$, while the thick red curve is obtained from application of the complete Eq. (7), which integrates over the full contact angle range. Both approaches use the same g distribution retrieved for the case example in section 3.1 with $\mu = 1.65$, and $\sigma = 0.135$. **Right (b):** The g distribution from the case example in Section 3.1 plotted in log scale and showing the critical contact angle range retrieved in Section 3.2 ($\theta_{c1} \approx 0.4$ rad and $\theta_{c2} \approx 0.79$) in red.

Furthermore, the critical contact angle range can be used to estimate a hypothetical nucleating area of the particle – the total active site surface area where nucleation will take place. The nucleation area $A_{nucleation}$ can be estimated as follows:

$$A_{nucleation} = A \int_{\theta_{c_1}}^{\theta_{c_2}} g(\theta) d\theta \qquad (11)$$

For the large ash particle system analyzed in the previous section (Fig. 2.1) it is estimated that for its estimated diameter of 300 μm and a cooling rate of 1 K/min $\theta_{c1} \approx 0.4$ rad and $\theta_{c2} \approx 0.79$ rad. Application of Eq. (11) yields a total ice active surface area estimate of 27 nm^2. Classical nucleation theory estimates that the area of a single active site is 6 nm^2 (Lüönd et al., 2010; Marcolli et al., 2007). The estimated total area of nucleation is therefore consistent with this value and supports the argument that competition between sites along the critical range of θ is taking place. However, the surface area where ice nucleation is occurring remains a very tiny fraction of the total particle surface. This further justifies the use of a continuum of surface area to define g as $dA/d\theta$ (Eq. 6). The nucleating area is a function of both the g Gaussian distribution of θ, and the total surface area of the considered particle. Figure 2.3(b) shows the g distribution in log scale and highlights in red the fraction of the distribution covered by the critical contact angle range. It is important to emphasize that the critical contact angles are variable parameters and not a property of the ice nucleating species. Therefore, for the same g distribution the critical contact angles shift in the direction of decreasing activity (larger θ) for smaller surface areas and increasing activity (smaller θ) for larger surface areas.

2.6 Using critical area analysis to predict droplet freezing spectra obtained in cold plate experiments

Many droplet freezing array experimental methods such as those described in Broadley et al. (2012), Murray et al. (2011), Vali (2014), Wright & Petters (2013), and Hiranuma et al. (2015a) use atmospherically relevant particle sizes (hundreds of nanometers to a few microns in diameter) but create the droplet array from a prepared suspension of the particles of interest in water. The resultant particle concentrations are typically high and the number of particles present in each droplet has to be approximated using statistical methods. When total particle surface area is high enough we hypothesize that it is conceivable that a threshold is reached whereby most of the species' maximum possible external variability is already available within the particle-droplet system. At this point it is approximated that no additional diversity in external variability (ice active site ability or θ) is created by further increasing the total particle surface area in the water volume; the external variability has effectively saturated. For the application of this model to cold plate data where droplets are prepared from a suspension of the species being investigated, the particle population in each droplet is treated as one aggregate surface (and thus one large particle) and a mean surface area value is assumed for the particle material in all the droplets in the array. This estimate is retrieved from the weight percentage of the material in the water suspension and our best guess for a reliable surface area density which is how much surface area the particle material possesses relative to its mass (Hiranuma et al., 2015a, 2015b).

Past the hypothesized surface area threshold, which will be referred to as the critical area, each member of the system's population (droplets with particles immersed in them) become

approximately identical in their ice nucleation properties and the theoretical frozen fraction can be expressed as:

$$F = P_f(one\ \text{system}) = 1 - \prod_{i=1}^{n} P_{uf,i} \qquad (12)$$

where F is the droplet frozen fraction, n is the number of droplets, and $P_{uf,i}$ is the probability that the droplet i does not freeze. Further expanding the expression yields:

$$F = 1 - \exp\left[-t\left(\sum_{i=1}^{n} A_i \int_0^{\pi} J(\theta) g_i(\theta) d\theta\right)\right] = 1 - \exp\left[-t \int_0^{\pi} J(\theta) \sum_{i=1}^{n} (A_i g_i) d\theta\right] \quad (13)$$

Next the parameter $\bar{g}$ is defined:

$$\bar{g} = \frac{\sum_{i=1}^{n} (A_i g_i)}{A_t} \qquad (14)$$

where A_i is the sum of all particle surface area available inside a given droplet i, and A_i is the mean particle surface area per droplet. Equation (13) then becomes:

$$\Rightarrow F = 1 - \exp\left(-tA_t \int_0^{\pi} J(\theta) \overline{g(\theta)} d\theta\right) \qquad (15)$$

$\bar{g}$ is the arithmetic average of all the g distributions for ensemble of particles in the droplet (each particle has its own g distribution) with a cumulative area larger than the critical area of the species they belong to. Alternatively, $\bar{g}$ can be thought of as the probability density function for all possible ice nucleating activity of a given species or particle type. It is worth mentioning that $\bar{g}$ is a true continuous probability density function. While the g distribution of an individual particle is an

approximate continuous function – due to the very small size of ice nucleating active sites – $\bar{g}$ contains all possible values of contact angles that an ice nucleating species can exhibit.

Above a certain surface area threshold, it is conceptualized that the chance of an ice-nucleating particle surface not possessing the entire range of ice nucleating activity (θ) becomes very small. The model therefore assumes that any particle or population of particles having a total surface area larger than the critical area can be approximated as having $\bar{g}$ describe the actual g distribution of the individual particles. In other words, for large particles with more surface area than the critical area threshold, it is assumed that the external variability between individual particles will be very small such that the particle population can just be described by one average continuous distribution of the ice nucleation activity, $\bar{g}$.

To resolve the g distributions of the systems possessing particle surface areas smaller than the critical area the first step is to approximate the critical area. Experiments must start at very high particle mass concentrations to ensure the total surface area per droplet exceeds the critical area. For the illite mineral particle case study considered next, for example, high particle concentrations were those that resulted in total particle surface areas greater than about 2×10^{-6} cm^2. The particle number or surface area concentration is then decreased until the retrieved g distribution (from the measured droplet freezing temperature spectrum for an array of droplets containing particles) can no longer be reasonably predicted by $\bar{g}$. This point can identify the parameter A_c, the critical area of the species under study. A schematic of the procedure is summarized in Fig. 2.4.

Figure 2.5 shows experimental freezing curves (open symbols) taken from Broadley et al. (2012), with different particle surface area concentrations. 10-20 μm droplets were used and cooled at a cooling rate of 5 K/min. The curves from the highest particle concentration experiments,

7.42×10^{-6} cm^2 (6b) and 2.02×10^{-6} cm^2 (6a), are used to approximate the critical area of the system by first fitting the 6b curve with a g distribution and then successfully predicting the 6a curve with the same g distribution obtained from 6b and applying a particle surface area correction. The fit to the 6b curve is done using Eq. (9) and follows the same procedure of least square error fitting described in section 3.1. This g distribution is therefore assumed to be the $\bar{g}$ of the considered

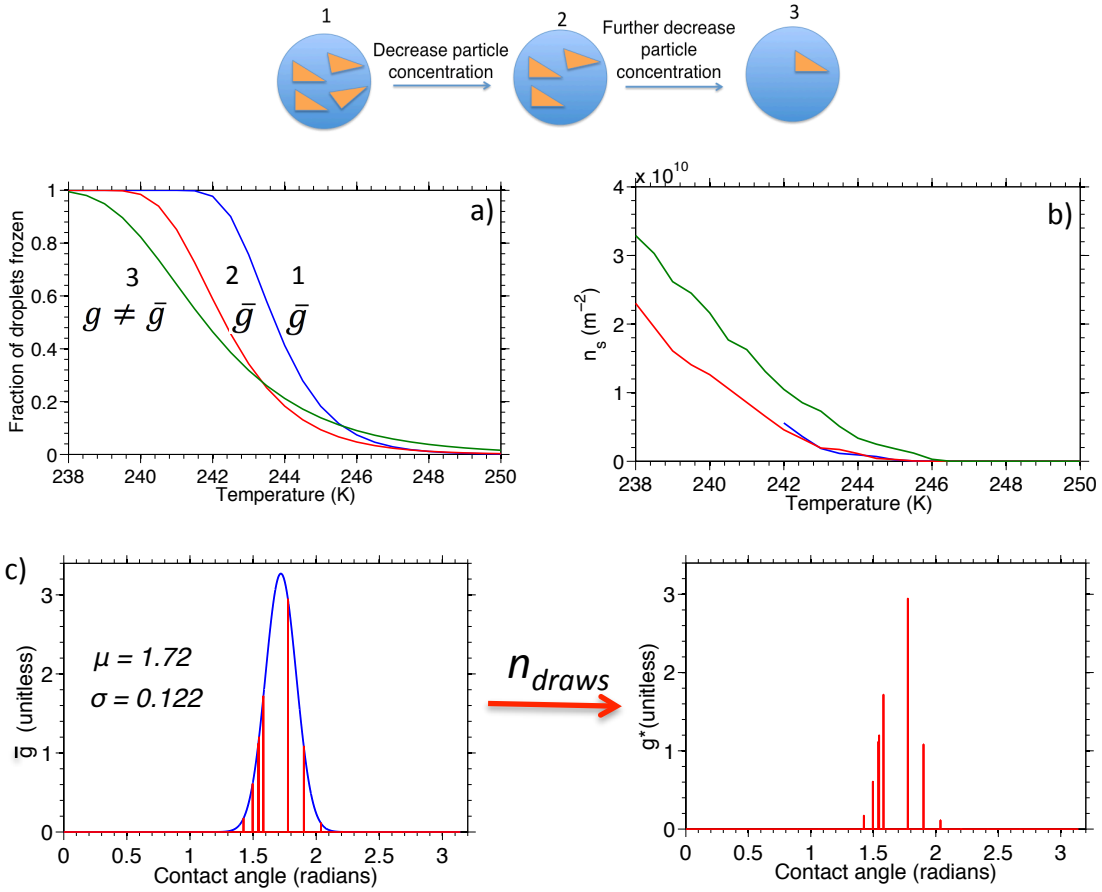

Figure 2.4. Top: Schematic summarizing the procedure for determining the critical area. **Left (a):** The frozen fraction freezing curves shift to lower temperatures initially due solely to the decrease in total surface area of the ice nucleating particles (curves 1 & 2). As the total surface area of the particles is decreased below the critical area threshold ($g \neq \bar{g}$) the slope of the freezing curve also broadens because the effective distribution of ice nucleating sites has changed – more external

variability has been introduced (curve 3). **Right (b):** Ice active site density (n_s) retrieved from the frozen fraction plots on the left for the same three particle concentration systems. Above the critical area limit ($g = \bar{g}$) the two n_s curves are essentially the same, but below the critical area threshold ($g \neq \bar{g}$) n_s increases, even though the same particle species was measured in all three experiments. These exemplary frozen fraction and n_s curves were produced by fitting a $\bar{g}$ distribution to droplet freezing measurements of illite mineral particles from Broadley et al. (2012). **Bottom (c):** Schematic summarizing how g^* is retrieved from $\bar{g}$ using n_{draws}. In each draw a random contact angle from the full range of contact angles [0, π] is chosen after which the value of g^* at that contact angle (right) is assigned the value of $\bar{g}$ at the same contact angle (left).

system with $\mu = 1.72$, and $\sigma = 0.122$. Note that above the threshold concentration A_c, approximated here as occurring between 7.42×10^{-6} cm^2 and 2.02×10^{-6} cm^2, a change in the total available surface area A is all that is required to account for how the change in particle concentration shifts the droplet freezing temperature curve. This is not the case when total area is less than the critical area A_c, as discussed next.

Moving to the lower concentration freezing curves (1.04×10^{-6} cm^2 – 5a; and 7.11×10^{-7} cm^2 – 4a) the transition to below the critical area begins to be observed. The solid lines attempt to predict the experimental data points using $\bar{g}$. Predicting experimental data points for the 1.04×10^{-6} cm^2 (5a) system with the same $\bar{g}$ distribution captures the 50% frozen fraction point but fails at accounting for the broadness on the two ends of the temperature spectrum. The prediction from $\bar{g}$ completely deteriorates in quality for the lowest concentration experiments (7.11×10^{-7} cm^2 – 4a) as it neither captures the temperature range over which freezing is occurring nor the 50% frozen fraction point.

We investigated a similar trend when freezing droplets containing commerical Snomax (York International), and MCC cellulose (Sigma-Aldrich) particles immersed in

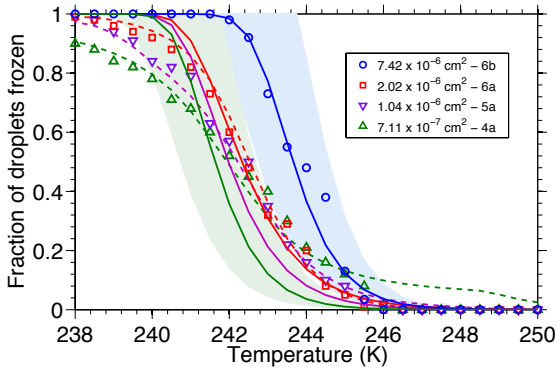

Figure 2.5. Experimental freezing curves for different surface area concentrations of illite mineral powder immersed in 10-20 μm diameter water droplets taken from Broadley et al. (2012) (circles). Lines are modeled predictions of the same data using the g^* distribution method. Solid lines are produced directly from the global $\bar{g}$ distribution first obtained from the high concentration system. The dashed lines are obtained by randomly sub-sampling the global $\bar{g}$ distribution to obtain g^* and following a surface area correction, as described in the text. The shaded region shows the predicted temperature range over which freezing of droplets occurs for the surface area variability associated with the droplet diameter range of 10-20 μm using $\bar{g}$ (i.e. running Eq. (9) with different values for A), for the highest and lowest particle concentration experiments.

oil in our in-house cold plate system, described by Polen et al. (2016). The relevant system details are that particle-containing water droplets of approximately 500-700 μm in diameter are immersed in squalane oil, analogous to the method of Wright et al. (2013), and the droplets' freezing temperature is determined optically during a constant 1 K/min cooling cycle. A new sample solution was prepared of the material being tested before every experiment to avoid potential

changes to the ice nucleation ability due to ageing. Ultrapure milli-Q water was used to minimize any background impurities that could provide a source of ice nucleants or solutes that would alter the freezing temperature of the water. Around 50 0.1 μL droplets were then produced with a pipette from this solution. Each freezing experiement was repeated at least twice, with about 50 droplets per run, to confrim that the independently retrieved frozen fractions fall within 1 K of each other for each replicate experiment. Figure 2.6a shows decreasing concentration freezing curves for droplets containing Snomax particles. Snomax is a freeze-dried powder manufactured from non-viable *Pseudomonas syringae* bacteria and is commonly used to make artificial snow due to its very mild freezing temperature of -3 to -7 °C. Its ice nucleation properties are attributed to large protein aggregates, and Snomax is often used as a proxy for atmospheric biological INP (Pandey et al., 2016; Polen et al., 2016; Wex et al., 2015). A similar approach was undertaken in which $\bar{g}$ was retrieved using the highest concentration freezing curve (solid blue line). The surface area density is assumed to be 1 m^2/g though it is recognized that given the protein aggregate based ice nucleating mechanism of Snomax it is difficult to attribute a surface area of nucleation to a mass of Snomax powder. However, a surface area value needs to be assumed to retrieve the ice nucleating properties using the framework presented here for the sake of comparing Snomax to the other systems. For an assumed critical area of 4×10^{-6} cm^2 (the surface area at 0.1 wt%) $\bar{g}$ was found to have $\mu = 0.66$, and $\sigma = 0.055$. Unlike the illite dataset considered first, only 50% of the freezing behavior of the second highest concentration freezing curve is captured by a frozen fraction retrieved from $\bar{g}$ (solid red line). Further lowering the concentration produces a similar trend previously observed for the droplets containing illite, with similar freezing onsets at higher temperatures but

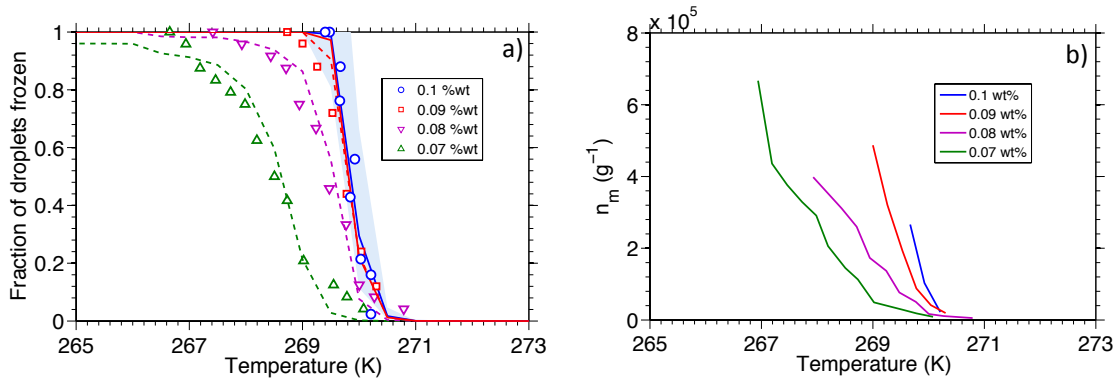

Figure 2.6. Left (a): Experimental freezing curves for different mass concentrations of commercial Snomax powder immersed in 500-700 µm diameter water droplets obtained using the CMU cold plate (circles). Solid lines are fits produced from randomly sampling from the $\bar{g}$ distribution retrieved from the highest concentration freezing curve (0.1 %wt). Dashed lines are fits produced from randomly sampling from the $\bar{g}$ distribution and a surface area correction. The second highest concentration freezing curve (0.09 %wt) is used to confirm the critical area threshold had been exceeded. The shaded region represents the effect of variability in surface area as in Fig. 2.5 but for a droplet diameter range of 500-700 µm, for the highest particle concentration. **Right (b):** Ice active site density (n_m) retrieved from the frozen fraction data on the left. A trend of decreasing n_m with decreasing concentration is observed for the droplets containing Snomax.

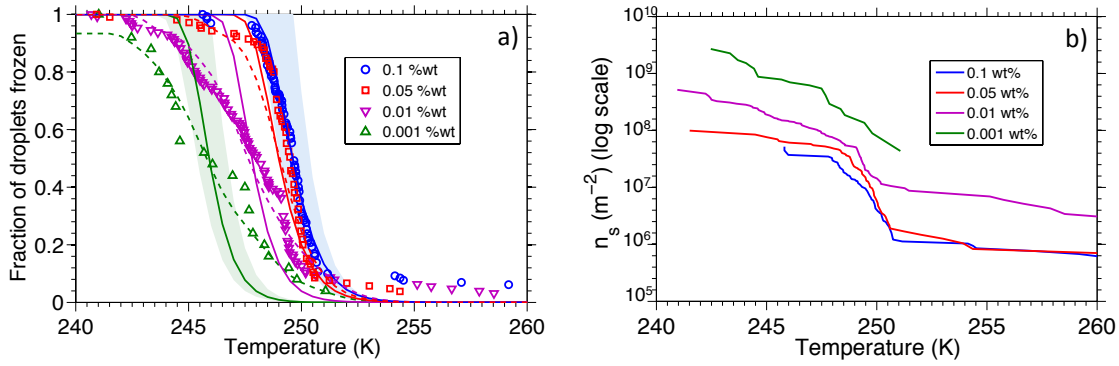

Figure 2.7. **Left (a)**: Experimental freezing curves for different mass concentrations of MCC cellulose powder immersed in 500-700 μm diameter water droplets obtained using the CMU cold plate (circles). Dashed lines are fits produced from randomly sampling from the $\bar{g}$ distribution retrieved from the highest concentration freezing curve (0.1 wt%, blue solid line) and a surface area correction. The second highest concentration freezing curve (0.05 wt%, red) is used to confirm the critical area threshold was exceeded. The shaded region represents the effect of variability in surface area as in Fig. 2.5 but for a droplet diameter range of 500-700 μm, for the highest and lowest particle concentration experiments. **Right (b)**: Ice active site density (n_s) retrieved from the frozen fraction data on the left. A trend of increasing n_s with decreasing concentration is observed.

significant divergence at lower temperatures (purple and green points). The frozen fractions retrieved from $\bar{g}$ for the 0.08 wt% and 0.07 wt% Snomax droplets (not plotted, as they almost overlap with the solid red line) do not capture any of the freezing behavior measured indicating a very sensitive dependence of ice nucleating activity on surface area. A notable difference from the droplets containing illite is that there is significant weakening in ice nucleation ability as the concentration/surface area of Snomax is reduced. This behavior matches what is known regarding the low abundance of the most efficient but fragile Type I ice nucleating proteins that freeze at -3 to -2 °C, versus the more abundant and resilient but less efficient Type III proteins that freeze around -8 to -7 °C (Polen et al., 2016; Turner et al., 1990; Yankofsky et al., 1981).

The freezing curves from droplets containing MCC cellulose powder (Hiranuma et al., 2015b) are shown in Fig. 2.7a. For the MCC cellulose freezing curves $\bar{g}$ was found to have $\mu = 1.63$, and $\sigma = 0.12$, from the 0.1 wt% curve. The freezing curve retrieved from droplets containing 0.1 wt% (blue) cellulose was estimated to be the critical area transition value. While the second highest

concentration freezing curve's (0.05 wt%, red) median freezing temperature is not captured by $\bar{g}$, the broadness of the curve is similar to that predicted by the model and the differences in the median freezing temperatures are within 1 K. Assuming a surface area density of 1.44 g/m^2 (Hiranuma et al., 2015a) the critical area for MCC cellulose is estimated to be around ~9.4×10^{-4} cm^2. MCC cellulose appears to exhibit ice nucleating capabilities reasonably stronger than illite and significantly weaker than Snomax, based on the observed freezing temperature spectra and the $\bar{g}$ values retrieved. $\bar{g}$ for Snomax was 0.66 ± 0.055, 1.72 ± 0.122 for illite NX, as compared to 1.63 ± 0.12 for MCC cellulose.

To predict the freezing curves of the droplets with particle surface areas lower than the estimated critical area for the systems considered here, the aggregate surface area of the entire particle population within each droplet is modeled as one large surface. A contact angle θ_r is randomly selected from the full contact angle range [0, π], and the value of the active site distribution g^* for the particle *i* being sampled for at θ_r is assigned the value of $\overline{g(\theta_r)}$:

$$\left(g_i^*(\theta_{r,n_{draw}})\right) = \overline{g(\theta_r)} \qquad (16)$$

The g^* distributions within this numerical model are given an asterisk to indicate that they are discrete distributions.

This process is repeated for a parameter n_{draws}, for each droplet in the array that produced the freezing curve being modeled. n_{draws} is the only parameter that is optimized for so the modeled freezing curves can predict the behavior of the experimental freezing curves. The value of n_{draws} typically ranges from 9 to 65 for the systems analyzed here and is therefore a relatively soft optimization parameter with small dynamic range. The sampled g^* distributions are normalized

with respect to the estimated total surface area for the freezing curve being modeled before being used to compute the freezing probability. The bottom part of Fig. 2.4 shows a schematic of how g^* is retrieved from $\bar{g}$ using $n_{draws.}$ With the sampled g^* distributions the freezing probability of each droplet is calculated using Eq. (9) and the frozen fraction curve is computed from the arithmetic average of the freezing probabilities:

$$F(below\ critical\ area) = \frac{1}{N}\sum_{i=1}^{N} P_{f_i} \qquad (17)$$

where N is the number of droplets in the cold plate array.

The behavior of the experimental curve is captured using the n_{draws} numerical model in which random sampling from the ice nucleating spectrum dictated by $\bar{g}$ is carried out to predict the freezing curve. The dotted lines in Figs. 2.5, 2.6a, and 2.7a are obtained by sampling from the $\bar{g}$ model to successfully predict the behavior of all the freezing curves. The early freezing onsets of the lower concentration systems as well as the broadness in the curves are both captured with the model. After $\bar{g}$ was obtained from the high concentration data above the critical area threshold, the only parameter that had to be optimized to produce these accurately predicted freezing curves was n_{draws}. The values of n_{draws} for the lower concentration freezing curves for each of the systems investigated here are 21 ($2.02\text{x}10^{-6}$ cm^2), 19 (1.04×10^{-6} cm^2), and 11 (7.11×10^{-7} cm^2) for the droplets containing illite; 65 (0.09 wt%), 48 (0.08 wt%), and 23 (0.07 wt%) for the droplets containing Snomax; and 21 (0.05 wt%), 11 (0.01 wt%), and 9 (0.001 wt%) for the droplets containing cellulose. It should also be noted that there is an n_{draws} value for each system above for which the sampled distribution mimics $\bar{g}$. For example, when n_{draws} is 25 for the illite system the retrieved distribution will produce a freezing curve equivalent to using $\bar{g}$.

Perhaps the most notable characteristic is how the freezing curves of all three systems analyzed ascend together early as temperature is decreased but then diverge as the temperature decreases further (Figs. 2.5, 2.6a, and 2.7a). The closeness of the data at warmer temperatures (the ascent) is interpreted by the framework as the continued presence of smaller contact angles (stronger active sites) within the g^* distributions of some of the particles under all the particle concentrations explored in these experiments. Due to the strength of the ice nucleating activity at small contact angles a smaller number of draws is required to capture this region of the contact angle range than the lower activity described by the larger contact angles. This results in a greater diversity in the larger (weaker) contact angles between the particles and is how the model successfully captures the increasing external variability with decreasing surface area. In a later section the claim of more external variability contributing to the broader curves below the critical area threshold is supported with a closer look at the numerical results from the model.

The droplets containing Snomax displayed an immediate shift in freezing behavior for small changes in concentration (from 0.1 wt% to 0.09 wt%) whereby a small drop in concentration and thus surface area resulted in a broader temperature range over which freezing of the droplets occurred (Fig. 2.6a). In the context of the model presented here this is due to the mode of the $\bar{g}$ distribution occurring at a very small (and thus very active) contact angle of 0.66. In this contact angle range the barrier to nucleation is greatly reduced causing freezing to be even more sensitive to the strongest active sites, and less sensitive to the competing active sites that are weaker but more abundant (depicted in Fig. 2.2), and therefore causing freezing curves to be quite steep versus T. A small change in the surface area of this material may have produced a significant reduction in the probability of droplets possessing this very strong range of ice nucleating activity, resulting

in the observed broadening of the freezing curves. This trend in Snomax is further investigated numerically in a following section.

Figure 2.4 also plots the popular exclusively deterministic scheme's ice active site density parameter n_s (Hiranuma et al., 2015a; Murray et al., 2012; Vali, 1971, 2008; Wex et al., 2015). n_s is an active site density function defined in the following equation:

$$F = 1 - \exp(-n_s(T)A) \qquad (18)$$

Equation (18) is similar in mathematical form to Eq. (15) and inherently assumes that active site density can be defined as uniform over a particle's surface and is therefore independent of the total surface area (it is multiplied by total surface area to estimate total heterogeneous ice nucleation activity). From this point onwards n_s is regarded as the deterministic analog of $\bar{g}$, where any time-dependent (stochastic) freezing is omitted. The justification presented for the definition and use of the critical area quantity also applies to the n_s framework, where it is argued that n_s ceases to become a proper representation of the ice nucleation activity below the critical area threshold.

The values of n_s were retrieved directly from freezing curves of droplets with illite particles immersed in them measured in a cold plate system by Broadley et al. (2012) and used to produce the right panel in Fig. 2.4. As the total particle surface area of the system under study is reduced from the blue to the red curve, the retrieved n_s values are similar indicating that variability of active sites remains constrained within droplets. Note that both the red and blue curves were obtained from systems we have determined were above the critical area threshold (Fig. 2.4). Further reduction of total surface area to below the critical area threshold shifts the n_s values noticeably, as seen by the significant increase in n_s(T) for the green curve. As all three curves were obtained by just varying the particle concentration of the same species the same n_s values should be retrieved

for all three curves at each temperature; the n_s scheme is designed to normalize for the total surface area or particle mass present. This is successful for the higher particle surface area systems (red and blue curves are similar) but not at lower particle area (green curve diverges). The large increase in n_s observed when total surface area is below the critical area threshold indicates that the observed droplet freezing temperature spectra do not just linearly scale with particle concentration or surface area. Further analysis will show this is not due to an enhancement of ice nucleating activity per surface area but is actually the random sampling process redistributing smaller and larger contact angles in such a way that some particles now have higher ice nucleating activity per surface area while others have a weaker ice nucleating activity per unit surface area. This is regarded as an increase in the external variability of the system.

We have observed other similarly large effects of particle concentration on the measured droplet freezing temperature spectrum and the retrieved n_s curves from our own cold plate measurements. Figures 2.6b and 2.7b display n_m (active site density per unit mass (Wex et al., 2015)) and n_s curves versus temperature for freezing droplets containing Snomax and MCC cellulose, respectively. Similar to the data in Fig. 2.4b, these two systems also exhibit a divergance in n_s (or n_m) as concentration (or surface area) is decreased. Droplets containing MCC cellulose exhibited a much stronger sensitivity to decreasing surface area than the droplets containing illite did, with changes in the values of n_s of up to four orders of magnitude. The droplets containing Snomax on the other hand were less sensitive to changes in surface area and exhibited an opposite trend in n_m, with the values of n_m *decreasing* with decreasing concnentration. This is consistent with the analysis of the Snomax freezing curves, where the ice nucleating activity experienced a substantial drop with decreasing surface area. It is further argued in a later section that this is due to the very sharp active

site density function g that Snomax particles appaear to possess, resulting in steep droplet freezing temperature curves.

In assessing the three systems investigated here, it appears that the critical area threshold depends a lot on the strength ($\overline{g(\theta)}$) of the ice nucleating activity for that system. Capturing the critical area transition for illite required probing droplets that were an order of magnitude smaller than the droplets containing Snomax and cellulose, indicating a very large difference in the scale of the critical area. One explanation for this behavior is that when ice nucleating activity is weak, nucleation can occur over a larger total nucleating surface area. This means there is a smaller chance of losing critical active sites in a droplet as the amount of material is reduced with decreasing particle concentration. This argument is supported by these three data sets that span almost the entire heterogeneous ice nucleation temperature range.

For the illite mineral suspensions Broadley et al. (2012) identified two total surface area regimes by analyzing their droplet freezing curves. In the lower surface area regime they observed a different freezing dependence on particle surface area than at higher surface areas. At higher surface areas they saw no dependence of the freezing curves on total particle surface area, which is inconsistent with both the stochastic and deterministic frameworks. For larger droplets the transition seemed to occur at higher total particle surface area indicating that there might be a particle concentration effect impacting the total particle surface area per droplet. We have conducted our own illite measurements on the same mineral sample used by Hiranuma et al. (2015) (Arginotec, NX nanopowder) to investigate this high concentration regime and further probe the applicability of $\bar{g}$ to freezing curves above the identified critical area threshold. Figure 2.2.

8 shows the frozen fractions versus temperature for an ensemble of droplets containing illite NX on our cold plate system. The concentrations used were 0.5 wt%, 0.3 wt, 0.25 wt%, 0.2 wt%, 0.1 wt%, 0.05 wt%, 0.03 wt%, 0.01 wt%, and 0.001 wt% and the droplets were cooled at a rate of 1 K/min. Average surface area estimates are made by assuming 600 μm diameter droplets and a surface area density of 104 m^2/g (Broadley et al., 2012). The solid lines are applications of Eq. (15) with the same $\bar{g}$ as the one found for the illite data set considered above. It can be seen that this $\bar{g}$ retrieved from cold plate experiments where droplets are on the order of 10-20 μm produces reasonable predictions of the freezing curves where droplets are on the order of 600 μm and thus contain particle surface areas up to five orders of magnitudes larger. Another important conclusion that can be drawn from this dataset is that high concentration data (0.25 wt%, 0.3 wt%, and 0.5 wt%) exhibited a similar plateauing in freezing temperatures despite additional amounts of illite. This is similar to the concentration range where Broadley et al. (2012) found a saturation effect when further increasing the concentration of illite (over 0.15 wt%). The fact that the

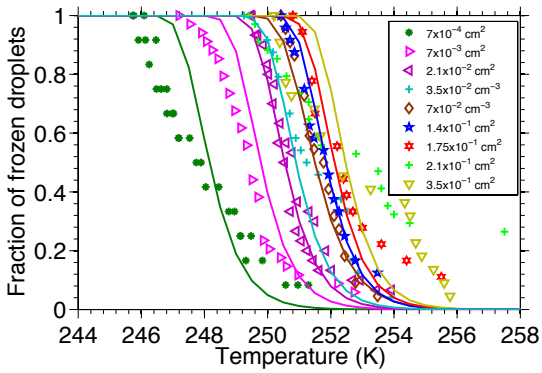

Figure 2.8. Experimental freezing curves for different mass concentrations of illite NX powder immersed in 500-700 µm diameter water droplets obtained using the CMU cold plate (circles). The solid lines are the predicted frozen fractions based on the $\bar{g}$ distribution retrieved from the Broadley et al. (2012) data and a surface area correction. A concentration saturation effect appears

to be present, whereby the blue, red, and gold experimental data points overlap despite being at different concentrations.

concentration where this saturation effect is so similar while the droplet volumes and consequently the amount of illite present between the two systems is quite different points to a physical explanation such as particle settling or coagulation due to the very high occupancy of illite in the water volume. These physical processes could reduce the available particle surface area in the droplet for ice nucleation. Additionally, the high concentration freezing curves show a good degree of broadening in the temperature range over which freezing occurs. These three curves share a close 50% frozen fraction temperature (with the 0.5 wt% oddly exhibiting a slightly lower 50% frozen fraction temperature than the other two). One explanation that is consistent with the hypothesis of particle settling and coagulation is that it becomes less likely that the droplets contain similar amounts of suspended material when they are generated from such a concentrated suspension (Emersic et al., 2015). This results in larger discrepancies in available surface area between the droplets and therefore a broader temperature range over which the droplets are observed to freeze.

One final thing to note is that the mathematical analysis presented here ignores the variability in total particle surface area present between droplets in each experiment. According to the range of droplet diameters mentioned in the Broadley et al. (2012) data of 10-20 μm surface area variability between the smallest and largest droplets in the experiment can be as high as a factor of 8. This assumes each droplet has the same particle concentration. While for the data presented from the CMU cold plate with droplet diameter varying from 500-700 μm, variability can be as high as a factor of 5. This assumes that the particle concentration is the same in each droplet, as

they were produced from well-mixed particle suspensions in water. This surface area variability can be the source of an alternative explanation to the broadness of the freezing curves, whereby an analysis along the lines of what is presented in Alpert and Knopf (2016) can be applied.

The shaded regions of Figs. 2.5, 2.6a, and 2.7a show the predicted temperature range over which freezing of droplets occurs for the surface area variability associated with the diameter range of the considered experiments using $\bar{g}$ (i.e. running Eq. (9) with different values for A). Figs. 2.5 and 2.7a show the predicted freezing variability for the highest and lowest mass concentrations while Fig. 2.6a only shows it for the highest concentration as the range predicted for the lowest concentration almost completely overlaps with the highest concentration. The prediction from surface area variability does contain the temperatures over which droplets freeze for the high concentration freezing curve but falls short of capturing the range for the low concentration-freezing curve. More importantly while the scatter in surface area between droplets can explain some of the broadness in the freezing curves, it is unable to explain why the curves become broader in the temperature range they span with decreasing surface area. Freezing temperature should respond linearly to surface area, if no other factors are changing (Eq. (9)). This observed trend is quite repeatable; according to Broadley et al. (2012) freezing temperatures were reproducible to within 1 K for their illite measurements, while for the CMU experiments for illite, MCC cellulose, and Snomax, the difference in freezing temperature spectra between at least two replicate experiments did not exceed 1 K. Therefore, if surface area scatter alone is proposed to explain the increasing variability of freezing temperatures with decreasing concentration/surface area, a cause for an increase in surface area scatter with decreasing concentration would have to be hypothesized. We recognize that such a surface area variability approach is also a viable one but

the framework presented here presents an increase in the variability in ice nucleation activity with decreasing concentration/surface area as the means for describing the observed trends.

2.7 Comparison between $\bar{g}$, n_s, and other existing parameterizations of heterogeneous ice nucleation

To our knowledge, this is the first heterogeneous ice nucleation parameterization that aims to attribute a surface area dependence to active site distributions of ice nucleating particles. The popular exclusively deterministic scheme (Broadley et al., 2012; Murray et al., 2012; Vali, 1994, 2008; amongst others) prescribes an ice active site density function n_s that is an intensive property of the species under study. Equation (15), derived from classical nucleation theory and used in the $\bar{g}$ model, and the deterministic-based Eq. (18) used in the n_s model, have a very close mathematical form. Both carry a negative exponential dependence on surface area, and the temperature dependence in the rest of the variables is inside the exponential.

Fitting freezing curves with droplets below the critical area threshold with n_s yields errors similar to fitting the curves with $\bar{g}$. Doing so has an inherent assumption of the ice nucleation activity being totally internally variable. This is clear in comparing Eqs. (15) and (18). That is $\bar{g}$ and n_s both offer incomplete information about the distribution of ice nucleation activity for a species. A similar conclusion along these lines was reached by Broadley et al. (2012) when the authors noted that the best fits to their freezing curves at low concentrations were achieved when the system was assumed to be totally externally variable. That is when each particle was assumed to have a single contact angle but a distribution assigned a spectrum of contact angles for each particle in the population.

There are other formulations that hypothesize an active site based or multi-component stochastic model such as the ones described in Vali & Stransbury (1966), Niedermeier et al. (2011), Wheeler and Bertram (2012), and Wright and Petters (2013). Vali and Stransbury (1966) were the first to recognize that ice nucleating surfaces are diverse and stochastic and thus active sites need to be assigned both a characteristic freezing temperature as well as a variability parameter around that temperature. Niedermerier et al. (2011) proposed the soccer ball model, in which a surface is partitioned into discrete active sites with each site conforming to classical nucleating theory. Marcolli et al. (2007) found a Gaussian distribution of contact angles could best describe their heterogeneous ice nucleation data in a completely deterministic framework. Welti et al. (2012) introduced the alpha-PDF model where a probability density function prescribes the distribution of contact angles that a particle population possesses, such that each particle is characterized by a single contact angle. Wright and Petters (2013) hypothesized the existence of a Gaussian probability density function for a specific species, which in essence is similar to the $\bar{g}$ framework described here. The notable difference is that their probability density function was retrieved via optimizing for all freezing curves, and not from independently fitting high concentration freezing curves as we have done here. Alpert and Knopf (2016) present a single component stochastic framework but successfully describe freezing behavior by considering surface area variability; more specifically defining a distribution of surface areas material in different droplets exhibits. A distribution of particle surface areas can provide a similar basis for variability in freezing temperatures between different particle containing droplets as a distribution of ice nucleating activity.

The n_s scheme is now more commonly used to describe and compare cold plate and other experimental ice nucleation data instead of the multi-component stochastic schemes (Hiranuma et

al., 2015a; Hoose and Möhler, 2012; Murray et al., 2012; Wex et al., 2015). This is in part due to the necessary inclusion of more variables required by other frameworks (such as prescribing a discrete number of active sites in the soccer ball model by Niedermeier et al. (2011)) than the simpler purely deterministic scheme of n_s. The new formulation described here requires only prescribing a species' heterogeneous ice nucleation ability as a function $\bar{g}$ along with finding the critical area, A_c, and n_{draws}. The critical area is determined by repeatedly measuring freezing curves for the same system or sample using different particle concentrations. Varying particle concentration is already routinely used in cold plate experiments to widen the droplet freezing temperature range that can be measured. An estimate of the total surface area of the particles under study must be made and associated with the retrieved freezing curves. While a process of random sampling using n_{draws} is initially necessary to predict the freezing curves at more atmospherically realistic concentrations below the critical area, in a following section we will introduce easy to apply parameterizations that derive from this sub-sampling of droplet freezing temperature spectra obtained above the critical area threshold.

2.8 Dependence of g on ice nucleating particle size

The particle size dependence of the freezing probability comes from the exponential dependence of the freezing probability on the surface area A as shown in Eq. (7). The freezing probability's sensitivity to surface area is the same as its sensitivity to time however the quadratic dependence of area on radius makes size a more sensitive parameter than time. Furthermore, there might be more subtle size dependencies in the g function itself. For a given particle type, whether size affects the diversity (internal variability) of nucleating sites is not something that can be trivially probed experimentally. To accurately test any potential size dependence, particles of

varying sizes need to be probed individually and compared. Measurements in which particles were size selected before assessing their ice nucleation ability have been performed, such as those using continuous flow diffusion chambers as described in Koehler et al. (2010), Lüönd et al. (2010), Sullivan et al. (2010a), Welti et al. (2009), among others. However, a similar limitation to the cold plate experiments presents itself in which the freezing onsets of many droplets containing a range of particle sizes are averaged to find a frozen fraction curve. The resultant curves have potential internal and external variability embedded, with not enough information to disentangle them. Hartmann et al. (2016) recently investigated the impact of surface area on active site density of size selected kaolinite particles by probing three different particle diameters. They concluded that kaolinite ice nucleating activity did not exhibit size dependence, similar to the trends reported here. However, a different mineral species was investigated than the illite we focus on here, and they probed a very different size range than in our experiments. We therefore think that our results provide incentive to pursue more of the quite insightful experiments presented by Hartmann et al. (2016) where particle size is varied over a large range.

The argument for the existence of a species' specific critical area can be made for either a total number of particles in a specific size range or a total particle surface area. Assuming that a single species' surface area does not undergo intensive changes in its ice nucleation properties (such as chemical processing as discussed in Sullivan et al. (2010a, 2010b)) a cut-off critical size can be defined. Above this critical size the active site distribution is $\bar{g}$ while below it is some distribution of g's that can be sampled from $\bar{g}$. In one of the cases studied here in Fig. 2.5 for illite mineral particles the critical surface area was around 10^{-6} cm^2. This corresponds to a single spherical particle with an equivalent diameter of around 10 μm, a size cutoff that is quite atmospherically relevant (DeMott et al., 2010). The vast majority of the atmospheric particle number and surface

area distributions are found at sizes smaller than 10 μm. Thus we conclude that for illite mineral particles, individual atmospheric particles will not contain the entire range of ice active site activity ($\bar{g}$) within that one particle, and each particle's ice nucleation ability is best described by an individual g distribution (that is a sub-sample of $\bar{g}$).

Application of Eq. (11) to find $A_{nucleation}$ for illite systems 6a (2.02×10^{-6} cm^2) and 5a (1.04×10^{-6} cm^2) from Broadley et al. (2012) gives insight into how the nucleating area is influencing the shape of the freezing curves. System 6a is where the critical area cutoff was found to occur while 5a started to exhibit the behavior of a broader freezing curve with a similar onset of freezing, indicating it is below the critical surface area. In Fig. 2.9 the average cumulative ice nucleating area computed from Eq. (11) is plotted against the critical contact angle range for the two systems. In examining the cumulative nucleating areas two regions can be identified. The first region (0.95 rad to 1.15 rad) includes the stronger active sites that contribute to the earlier warmer regions of the freezing curves, while the second region (1.15 to 1.2) contributes to the tail and colder end of the freezing curves. The first region is broader in contact angle range but smaller in total nucleating area. Therefore, statistically there is a higher chance of particles of smaller area to draw these contact angles in the random sampling process. The second region is narrower in the critical contact angle range but occupies a larger fraction of the total nucleating area. Therefore, more draws are necessary to replicate the nucleating behavior of this region and thus there is a stronger drop off in the nucleating area represented by these less active contact angles as the surface of the particles is reduced.

This helps to explain why the onset of freezing for the two curves is so similar. The diverging tail can be attributed to the divergence of the nucleating areas at higher contact angles in the critical contact angle range. The steeper rise of the average nucleating area

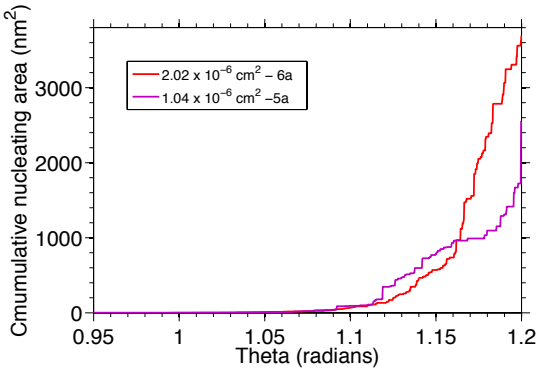

Figure 2.9. Cumulative ice nucleating surface areas from application of Eq. (11) to modeled average g distributions from systems 6a (red) and 5a (purple) in Fig. 2.5, taken from cold plate measurements of illite in droplets from Broadley et al. (2012), plotted against the critical contact angle range. At low contact angles the two systems have close total nucleating surface areas. This explains the similar onset of freezing before the eventual divergence at lower temperature (larger contact angle).

of system 6a is due to its greater chance of possessing active sites characterized by the second region of the critical contact angle range compared to system 5a due to the larger surface area present in 6a. This creates a larger spread in the freezing onset of droplets in system 5a after a few droplets initiated freezing in a similar manner to system 6a.

A similar nucleating area analysis was performed on the droplets containing Snomax and is shown in Fig. 2.10. The cumulative nucleating areas for the droplets with Snomax concentrations of 0.09 wt% and 0.08 wt% (red and green data in Fig. 2.6a, respectively) are calculated and shown

over the critical contact angle range with the same color scheme. Unlike the illite system, droplets containing Snomax exhibit a more straightforward trend in cumulative nucleating area vs. critical contact angle. The cumulative nucleating area is consistently smaller in the 0.08 wt% system

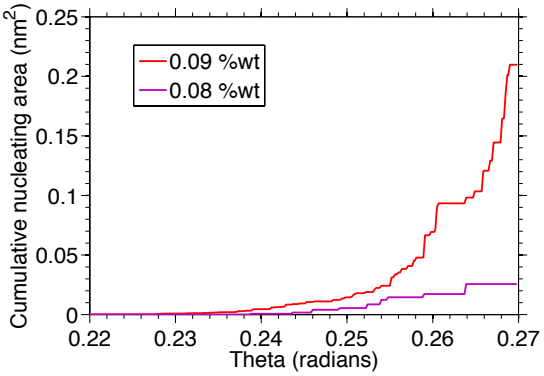

Figure 2.10. Cumulative ice nucleating surface areas from application of Eq. (11) to modeled average g distributions from droplets containing 0.09 wt% Snomax (red) and 0.08 wt% Snomax (purple) in Fig. 2.8 plotted against the critical contact angle range. This system does not exhibit similar nucleating areas at low contact angles, and thus does not show an increase in n_s with decreasing concentration (or surface area).

compared to the 0.09 wt% experiment, indicating that as the particle surface area is reduced the strong nucleators are reduced uniformly over the critical contact angle range. This supports the idea that the range of ice nucleating activity is much smaller for this very ice active system. The consistent decline in nucleating area is attributable to the very narrow critical contact angle range the nucleating area covers (only 0.05 rad). We propose that this is what explains the decrease in n_m with decreasing concentration observed in Fig. 2.5. We stress however that this explanation is not physical and is merely a mathematical interpretation of the experimental trend being observed.

The implications of this analysis on the size dependence of g is that below the critical surface area particles may or may not possess freezing behavior similar to the particles above the critical area threshold. The broadening of the freezing curves in the systems analyzed here as the surface area is reduced is interpreted as heterogeneity in ice nucleating ability between the different particles (external variability) and not due to the internal variability within the individual particles themselves. While the broadness of the curves above the critical surface area can be attributed to internal variability, the additional broadness in curves below the critical area cutoff are a result of external variability.

More detailed analysis studying various atmospherically relevant ice nucleating particles needs to be done to shed light on whether a particle size cutoff corresponding to a critical area threshold can be used to describe the behavior of different species. This has important implications on whether one active site density function (i.e. $\bar{g}$ or n_s) is sufficient to accurately represent the species' ice nucleating properties in cloud or atmospheric models. If not, a more detailed parameterization resolving the multi-dimensional variability may be necessary, such as a series of g distributions. For illite it seems that external variability is dominant and thus one active site distribution or n_s parameterization does not properly represent the species' ice nucleation behavior. The critical area effect is even more substantial for cellulose and Snomax as their ice nucleating activity is much stronger than illite. However, if a system's global $\bar{g}$ distribution is obtained then its full ice nucleation behavior is contained within and can be successfully subsampled from $\bar{g}$.

Cold plate experimental data potentially provides sufficient information to describe heterogeneous ice nucleation properties in cloud parcel and atmospheric models, however the analysis undertaken here suggests that retrieving one active site density parameterization (e.g. n_s)

and applying it to all surface areas can result in misrepresenting the freezing behavior. When samples are investigated, probing a wide concentration range enables the determination of both general active site density functions (e.g. $\bar{g}$) as well as the behavior of the species' under study at more atmospherically relevant concentrations below the critical area threshold. Once this analysis is undertaken more comprehensive parameterizations can be retrieved as will be developed in the next section.

The critical area analysis therefore emphasizes the dangers in extrapolating the freezing behavior of droplets containing a large concentration of particles to droplets containing smaller concentrations or just individual particles. Applying a parameterization such as n_s directly to systems below the critical area threshold in a cloud parcel model for example yields large differences in the predictions of the freezing outcome of the droplet population. As the concentration of the species within the droplets was decreased in the cold plate freezing spectra considered here the actual freezing temperature curves diverged more and more from those predicted when the systems were assumed to be above the critical area. This led to significant changes in the retrieved n_s values, as shown in Figs. 2.4, 2.6b, and 2.7b. The large effects of concentration on the droplet freezing temperature can be directly observed in the frozen fraction curves plotted in Figs. 2.5, 2.6a, and 2.7a. Differences between observed frozen fraction curves and ones that assumed uniform active site density yielded errors in the temperature range the droplets froze over as well as the median droplet freezing temperature. Therefore, a cloud parcel model would be unable to accurately predict the freezing onset or the temperature range over which freezing occurs using a single n_s curve obtained from high concentration data. This has important consequences for the accurate simulation of the microphysical evolution of the cloud system under

study such as the initiation of the Wegener–Bergeron–Findeisen and the consequent glaciation and precipitation rates (Ervens et al., 2011; Ervens and Feingold, 2012).

Figure 2.11 shows the range of n_s values for illite NX mineral compiled from seventeen measurements methods used by different research groups, the details of which are described by Hiranuma et al. (2014). The range of data is summarized into shaded sections to separate suspended droplet freezing techniques (such as a cold plate) from techniques where the material under investigation is aerosolized before its immersion freezing properties are assessed (such as the CFDC or AIDA cloud expansion chamber). The aerosol techniques tend to produce higher retrieved n_s values than those obtained by the wet suspension methods. n_s data spanning a surface area range of about five orders of magnitude retrieved exclusively from both our cold plate measurements and Broadley et al. (2012) measurements are also plotted. Data presented in Fig. 2.8 that was consistent with a $\bar{g}$ treatment is plotted as n_s (described in the CMU column in Fig. 2.11). These two datasets along with what was identified as the critical area dataset from the Broadley et al. experiments follow a consistent n_s line that lies within the range of the suspended droplet techniques. The blue triangles are low surface area data points retrieved from dataset 4a from the Broadley et al. measurements. As was argued earlier, this system exhibits higher n_s values, an artifact of the increased active site density of some of the particles. While this data is retrieved with a cold plate, it falls within the range of the aerosolized methods where particle surface areas are small. Finally, more of the suspension method range of retrieved n_s can be spanned by data where the concentration

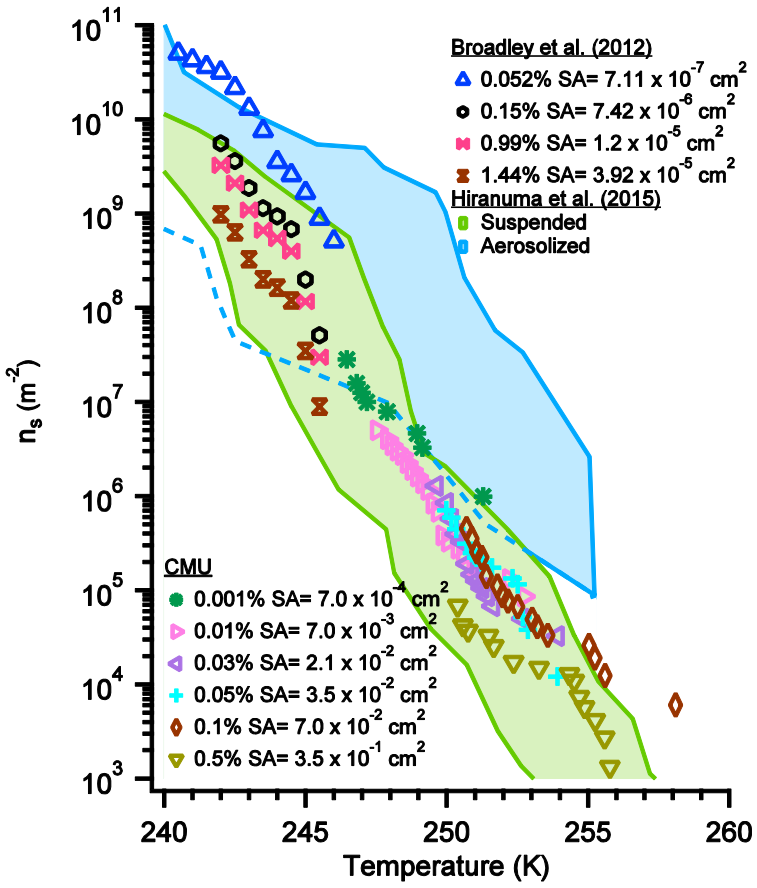

Figure 2.11. Range of n_s values for illite NX mineral dust compiled from seventeen measurement methods used by different research groups, the details of which are described by Hiranuma et al. (2015). The range of data is summarized into shaded sections to separate suspended droplet techniques (such as the cold plate) from techniques where the material under investigation is aerosolized before immersion freezing analysis. Data from both the Broadley et al. (2012) and the CMU cold plate systems are also plotted to show how much of the range can be spanned via the critical area effect (blue triangles) and the concentration saturation effect (purple hexagons and red and brown bow ties).

saturation effect takes place. Data that exhibited this behavior from the CMU cold plate system (golden triangles) and the Broadley et al. system (red and brown bowties) are plotted. This effect

tends to underestimate n_s since additional material is added while the freezing behavior remains the same. Thus just by varying particle concentration and surface area of illite in the droplets, cold plate measurements can span the range of n_s values obtained by the various aerosol and wet suspension measurement methods. We emphasize again than n_s(T) should be the same for the same system, and this metric is often used as the major means to compare and evaluate different INP measurement methods.

Various research groups using wet suspension methods typically vary particle concentrations to span a wider range of measureable droplet freezing temperature (Broadley et al., 2012; Murray et al., 2012; Wright and Petters, 2013). Our analysis indicates that by doing so different n_s values are in fact retrieved, just due to changes in concentration. This highlights the importance of obtaining n_s values that overlap in temperature space, to evaluate if n_s is in fact consistent as concentration is changed. We therefore provide the critical area framework presented here whereby ice nucleating surface area dependence is more complex than depicted in traditional deterministic and stochastic models, as a potential source of the discrepancy in n_s values for the various measurement techniques. This commonly observed discrepancy in n_s between droplet suspension and aerosol INP measurement methods is the subject of ongoing investigations, such as the INUIT project that is currently focusing on cellulose particles, a system we have included here. As the results from this multi-investigator project have not yet been published we cannot present them here. They show a similar trend as for the illite NX data, where the aerosol methods retrieve higher n_s values than the droplet suspension methods do. By changing particle in droplet concentration we can span much of the difference in n_s between the two groups of methods, as was shown for the illite NX measurements.

2.9 Application of the g parameterization to cloud models

Particle type-specific $\bar{g}$ distributions and critical areas can be used in larger cloud and atmospheric models to predict freezing onset and the rate of continued ice formation. The simplest parameterization is one that calculates the frozen fraction of droplets, F, for an atmospherically realistic system in which one ice nucleating particle is present in each supercooled droplet, the aerosol particle distribution is monodisperse (all particles therefore have the same surface area A), there is only one species present (therefore one $\bar{g}$ distribution is used), and the surface area of the individual particles is larger than that species' critical area. In this case Eq. (15) can be used:

$$F = 1 - \exp\left(-tA\int_0^{\pi} J(\theta,T)\overline{g(\theta)}d\theta\right) \qquad (15)$$

If the surface area of the individual particles is smaller than the critical area a modified version of Eq. (19) can be used instead:

$$F = 1 - \exp\left(-tA_c\int_0^{\pi} \left(J(\theta,T)\overline{g(\theta)}d\theta\right)h(A,T)\right) \quad (19)$$

where $h(A,T)$ is an empirically derived parameterization that corrects for the individual particle surface areas of the considered monodisperse aerosol population being smaller than the critical area. Therefore $h(A_c,T) = 1$.

An example of retrieving values of $h(A,T)$ would be in correcting the solid line for system 4a (7.11×10^{-6} cm^2) to the dotted line in Fig. 2.5. The solid line is the basic use of Eq. (15) however it was shown that the considered experimentally retrieved freezing spectrum was below the critical

area threshold. By taking the ratio of the dotted and solid lines values of *h* can be retrieved for that surface area at each temperature point.

If the aerosol particle population is polydisperse and its size distribution can be expressed as a function of surface area, the frozen fraction can be written as:

$$F = \int_{A_i}^{A_f} n_A(A)\left[1 - \exp\left(-tA\int_0^{\pi}\left(J(\theta,T)\overline{g(\theta)}d\theta\right)h(A,T)\right)\right]dA \qquad (20)$$

where A_i and A_f are the minimum and maximum values of the surface areas of the aerosol particle distribution and $n_A(A)$ is the number size distribution of the aerosol population expressed as a function of surface area.

If the aerosol ice nucleating population is composed of multiple species, two $\bar{g}$ parameterizations can be formulated for the two cases of an internally mixed (every particle is composed of all the different species) and externally mixed (every particle is composed of just one species). For the case of an internally mixed system Eqs. (15), (19), and (20) can be applied with a $\bar{g}$ distribution that is the surface area weighted average of the $\bar{g}$ distributions of all the considered species. This can be expressed as:

$$\bar{g}_{average} = \frac{1}{A}\sum_{i=1}^{m} A_i \bar{g}_i \qquad (21)$$

where A_i is the surface area of the species i, $\bar{g}_i$ is the $\bar{g}$ distribution of the species i, and m is the total number of species. If the system is externally mixed, the frozen fraction can be expressed as:

$$F = \frac{1}{m}\sum_{i=1}^{m} F_i \qquad (22)$$

where F_i is the frozen fraction of droplets containing particles of species i and can be retrieved from Eq. (19) or (20).

2.10 Conclusions

Cold plate droplet freezing spectra were carefully examined to investigate a surface area dependence of ice nucleation ability whereby one active site density function such as n_s cannot be extrapolated from high particle surface area to low particle surface area conditions. A method based on the notion of a critical surface area threshold was presented. It is argued that a species' entire ice nucleating spectrum can be confined within a global probability density function $\bar{g}$. For a system, be it one particle or an ensemble of particles, to have a total surface area greater than the critical area is a question of whether the surface is large enough to express all the variability in that particle species' ice active surface site ability. By analyzing droplets containing illite minerals, MCC cellulose, and commercial Snomax bacterial particles, it was shown that freezing curves above a certain critical surface area threshold could be predicted directly from the global $\bar{g}$ distribution obtained from the high particle concentration data alone. The lower particle concentration freezing curves were accurately predicted by randomly sampling active site abilities (θ) from $\bar{g}$ and averaging their resultant freezing probabilities. This framework provides a new method for extrapolating droplet freezing temperature spectra from cold plate experimental data under high particle concentrations to atmospherically realistic dilute particle-droplet systems.

We found that the shifts to colder freezing temperatures caused by reducing the particle concentration or total surface area present in droplets cannot be fully accounted for by simply normalizing to the available surface area, as is done in the ice active site density (n_s) analysis framework. When the surface area is below the critical area threshold the retrieved values of n_s can

increase significantly for the same particle species when the particle concentration is decreased. Above the critical area threshold the same n_s curves are retrieved when particle concentration is changed. Atmospheric cloud droplets typically contain just one particle each. Therefore, this effect of particle concentration on droplet freezing temperature spectra and the retrieved n_s values has important implications for the extrapolation of cold plate droplet freezing measurements to describe the ice nucleation properties of realistic atmospheric particles.

Systems that probe populations of droplets each containing one particle such as the CFDC are unable to probe a large particles-in-droplet concentration range but are powerful tools for the real-time investigations of ice nucleating particles at the realistic individual particle level (DeMott et al., 2010; Sullivan et al., 2010a; Welti et al., 2009). The frozen fraction curves produced from such an instrument do not provide enough information to associate the observed variability in ice nucleation ability to internal or external factors. However, future laboratory studies using the critical area-cold plate technique we have introduced here (e.g. Fig. 2.4) will provide new insight into the critical area thresholds of internal variability in ice active site ability for different species. This will produce more informed assumptions regarding the variability in ice nucleation properties observed through online field instruments, specifically when the measurements are made in conjunction with single particle chemical analysis techniques (Creamean et al., 2013; DeMott et al., 2003, 2010; Prather et al., 2013; Worringen et al., 2015).

Atmospherically relevant particle sizes may very well fall below the critical area threshold for an individual particle, at least for some species such as illite mineral particles considered here. Therefore, average ice nucleation spectra or active site distributions such as n_s and $\bar{g}$ may not be applicable for representing the ice nucleation properties of particles in cloud and atmospheric

models. However careful examination of the surface area dependence of ice nucleating ability of a species allows more accurate retrievals of active site density distributions that properly encompass this dependence.

Acknowledgements

This research was partially supported by the National Science Foundation (Award CHE-1213718), and M.P. was supported by a NSF Graduate Research Fellowship. The authors thank Dr. Paul DeMott for valuable discussions regarding an earlier version of this framework. Dr. Naruki Hiranuma at AIDA is acknowledged for providing us with the MCC cellulose and illite NX samples, as part of the INUIT project.

References

Alpert, P. A. and Knopf, D. A.: Analysis of isothermal and cooling-rate-dependent immersion freezing by a unifying stochastic ice nucleation model, Atmos. Chem. Phys., 16(4), 2083–2107, doi:10.5194/acp-16-2083-2016, 2016.

Andreae, M. O. and Rosenfeld, D.: Aerosol–cloud–precipitation interactions. Part 1. The nature and sources of cloud-active aerosols, Earth-Science Rev., 89(1–2), 13–41, doi:10.1016/j.earscirev.2008.03.001, 2008.

Baker, M. B. and Peter, T.: Small-scale cloud processes and climate., Nature, 451(7176), 299–300, doi:10.1038/nature06594, 2008.

Barahona, D.: On the ice nucleation spectrum, Atmos. Chem. Phys., 12(8), 3733–3752, 2012.

Broadley, S. L., Murray, B. J., Herbert, R. J., Atkinson, J. D., Dobbie, S., Malkin, T. L., Condliffe, E. and Neve, L.: Immersion mode heterogeneous ice nucleation by an illite rich powder representative of atmospheric mineral dust, Atmos. Chem. Phys., 12, 287–307, doi:10.5194/acp-12-287-2012, 2012.

Cantrell, W. and Heymsfield, A.: Production of Ice in Tropospheric Clouds: A Review, Bull. Am. Meteorol. Soc., 86(6), 795–807, doi:10.1175/BAMS-86-6-795, 2005.

Creamean, J. M., Suski, K. J., Rosenfeld, D., Cazorla, A., DeMott, P. J., Sullivan, R. C., White, A. B., Ralph, F. M., Minnis, P., Comstock, J. M., Tomlinson, J. M. and Prather, K. a: Dust and biological aerosols from the Sahara and Asia influence precipitation in the western U.S., Science, 339(6127), 1572–8, doi:10.1126/science.1227279, 2013.

DeMott, P. J., Cziczo, D. J., Prenni, A. J., Murphy, D. M., Kreidenweis, S. M., Thomson, D. S., Borys, R. and Rogers, D. C.: Measurements of the concentration and composition of nuclei for cirrus formation., Proc. Natl. Acad. Sci. U. S. A., 100(25), 14655–60, doi:10.1073/pnas.2532677100, 2003.

DeMott, P. J., Prenni, A. J., Liu, X., Kreidenweis, S. M., Petters, M. D., Twohy, C. H. and Richardson, M. S.: Predicting global atmospheric ice nuclei distributions and their impacts on climate, PNAS, 107(25), 11217–11222, doi:10.1073/pnas.0910818107, 2010.

Eidhammer, T., DeMott, P. J. and Kreidenweis, S. M.: A comparison of heterogeneous ice nucleation parameterizations using a parcel model framework, J. Geophys. Res., 114, D06202, doi:10.1029/2008jd011095, 2009.

Emersic, C., Connolly, P. J., Boult, S., Campana, M. and Li, Z.: Investigating the discrepancy between wet suspension and dry-dispersion derived ice nucleation efficiency of mineral particles, Atmos. Chem. Phys., 15(19), 11311–11326, doi:10.5194/acp-15-11311-2015, 2015.

Ervens, B. and Feingold, G.: On the representation of immersion and condensation freezing in cloud models using different nucleation schemes, Atmos. Chem. Phys., 12, 5807–5826,

doi:10.5194/acp-12-5807-2012, 2012.

Ervens, B. and Feingold, G.: Sensitivities of immersion freezing: Reconciling classical nucleation theory and deterministic expressions, Geophys. Res. Lett., 40(April), 3320–3324, doi:10.1002/grl.50580, 2013.

Ervens, B., Feingold, G., Sulia, K. and Harrington, J.: The impact of microphysical parameters, ice nucleation mode, and habit growth on the ice/liquid partitioning in mixed-phase Arctic clouds, J. Geophys. Res., 116(D17), D17205, doi:10.1029/2011JD015729, 2011.

Fletcher, N. H.: Active Sites and Ice Crystal Nucleation, J. Atmos. Sci., 26(6), 1266–1271, doi:10.1175/1520-0469(1969)026<1266:ASAICN>2.0.CO;2, 1969.

Fornea, A. P., Brooks, S. D., Dooley, J. B. and Saha, A.: Heterogeneous freezing of ice on atmospheric aerosols containing ash, soot, and soil, J. Geophys. Res., 114(D13), D13201, doi:10.1029/2009JD011958, 2009.

Hartmann, S., Wex, H., Clauss, T., Augustin-Bauditz, S., Niedermeier, D., Rösch, M. and Stratmann, F.: Immersion Freezing of Kaolinite: Scaling with Particle Surface Area, J. Atmos. Sci., 73(1), 263–278 [online] Available from: http://journals.ametsoc.org/doi/abs/10.1175/JAS-D-15-0057.1, 2016.

Herbert, R. J., Murray, B. J., Whale, T. F., Dobbie, S. J. and Atkinson, J. D.: Representing time-dependent freezing behaviour in immersion mode ice nucleation, Atmos. Chem. Phys., 14(16), 8501–8520, 2014.

Hiranuma, N., Augustin-Bauditz, S., Bingemer, H., Budke, C., Curtius, J., Danielczok, A., Diehl, K., Dreischmeier, K., Ebert, M., Frank, F., Hoffmann, N., Kandler, K., Kiselev, A., Koop, T., Leisner, T., Möhler, O., Nillius, B., Peckhaus, A., Rose, D., Weinbruch, S., Wex, H., Boose, Y., DeMott, P. J., Hader, J. D., Hill, T. C. J., Kanji, Z. A., Kulkarni, G., Levin, E. J. T., McCluskey, C. S., Murakami, M., Murray, B. J., Niedermeier, D., Petters, M. D., O'Sullivan, D., Saito, A., Schill, G. P., Tajiri, T., Tolbert, M. A., Welti, A., Whale, T. F., Wright, T. P. and Yamashita, K.: A comprehensive laboratory study on the immersion freezing behavior of illite NX particles: a comparison of 17 ice nucleation measurement techniques, Atmos. Chem. Phys., 15(5), 2489–2518, doi:10.5194/acp-15-2489-2015, 2015a.

Hiranuma, N., Möhler, O., Yamashita, K., Tajiri, T., Saito, A., Kiselev, A., Hoffmann, N., Hoose, C., Jantsch, E., Koop, T. and Murakami, M.: Ice nucleation by cellulose and its potential contribution to ice formation in clouds, Nat. Geosci., 8(4), 273–277, doi:10.1038/ngeo2374, 2015b.

Hoose, C. and Möhler, O.: Heterogeneous ice nucleation on atmospheric aerosols: A review of results from laboratory experiments, Atmos. Chem. Phys., 12(20), 9817–9854, 2012.

Hoose, C., Lohmann, U., Erdin, R. and Tegen, I.: The global influence of dust mineralogical composition on heterogeneous ice nucleation in mixed-phase clouds, Environ. Res. Lett., 3(2), 25003, doi:10.1088/1748-9326/3/2/025003, 2008.

Hoose, C., Kristjánsson, J. E., Chen, J.-P. and Hazra, A.: A Classical-Theory-Based Parameterization of Heterogeneous Ice Nucleation by Mineral Dust, Soot, and Biological Particles in a Global Climate Model, J. Atmos. Sci., 67(8), 2483–2503, 2010.

Koehler, K. a., Kreidenweis, S. M., DeMott, P. J., Petters, M. D., Prenni, a. J. and Möhler, O.: Laboratory investigations of the impact of mineral dust aerosol on cold cloud formation, Atmos. Chem. Phys., 10(23), 11955–11968, doi:10.5194/acp-10-11955-2010, 2010.

Koop, T., Luo, B., Tsias, a and Peter, T.: Water activity as the determinant for homogeneous ice nucleation in aqueous solutions, Nature, 406(6796), 611–4, doi:10.1038/35020537, 2000.

Levine, J.: Statistical explanation of spontaneous freezing of water droplets, NACA Tech, (Note), 2234, 1950.

Liu, X. and Penner, J. E.: Ice nucleation parameterization for global models, Meteorol. Zeitschrift, 14(4), 499–514, 2005.

Lüönd, F., Stetzer, O., Welti, A. and Lohmann, U.: Experimental study on the ice nucleation ability of size-selected kaolinite particles in the immersion mode, J. Geophys. Res., 115(D14), D14201, doi:10.1029/2009JD012959, 2010.

Marcolli, C., Gedamke, S., Peter, T. and Zobrist, B.: Efficiency of immersion mode ice nucleation on surrogates of mineral dust, Atmos. Chem. Phys., 7(19), 5081–5091, 2007.

Meyers, M. P., DeMott, P. J. and Cotton, W. R.: New Primary Ice-Nucleation Parameterizations in an Explicit Cloud Model, J. Appl. Meteorol., 31(7), 708–721, doi:10.1175/1520-0450(1992)031<0708:NPINPI>2.0.CO;2, 1992.

Mülmenstädt, J., Sourdeval, O., Delanoë, J. and Quaas, J.: Frequency of occurrence of rain from liquid-, mixed-, and ice-phase clouds derived from A-Train satellite retrievals, Geophys. Res. Lett., 42(15), 6502–6509, doi:10.1002/2015GL064604, 2015.

Murray, B. J., Broadley, S. L., Wilson, T. W., Atkinson, J. D. and Wills, R. H.: Heterogeneous freezing of water droplets containing kaolinite particles, Atmos. Chem. Phys., 11(9), 4191–4207, 2011.

Murray, B. J., O'Sullivan, D., Atkinson, J. D. and Webb, M. E.: Ice nucleation by particles immersed in supercooled cloud droplets, Chem. Soc. Rev., 41(19), 6519, doi:10.1039/c2cs35200a, 2012.

Niedermeier, D., Shaw, R. a., Hartmann, S., Wex, H., Clauss, T., Voigtländer, J. and Stratmann, F.: Heterogeneous ice nucleation: exploring the transition from stochastic to singular freezing behavior, Atmos. Chem. Phys., 11(16), 8767–8775, doi:10.5194/acp-11-8767-2011, 2011.

Pandey, R., Usui, K., Livingstone, R. A., Fischer, S. A., Pfaendtner, J., Backus, E. H. G., Nagata, Y., Fröhlich-nowoisky, J., Schmüser, L., Mauri, S., Scheel, J. F., Knopf, D. A., Pöschl, U., Bonn, M. and Weidner, T.: Ice-nucleating bacteria control the order and dynamics of interfacial water, Sci. Adv., 2(4), 1–9, doi:10.1126/sciadv.1501630, 2016.

Phillips, V. T. J., DeMott, P. J. and Andronache, C.: An Empirical Parameterization of Heterogeneous Ice Nucleation for Multiple Chemical Species of Aerosol, J. Atmos. Sci., 65(9), 2757–2783, doi:10.1175/2007JAS2546.1, 2008.

Phillips, V. T. J., Demott, P. J., Andronache, C., Pratt, K. A., Prather, K. A., Subramanian, R. and Twohy, C.: Improvements to an Empirical Parameterization of Heterogeneous Ice Nucleation and its Comparison with Observations, J. Atmos. Sci., 120927133920007, 2012.

Polen, M., Lawlis, E. and Sullivan, R. C.: The unstable ice nucleation properties of Snomax(R) bacterial particles, J. Geophys. Res. 121, 11,666–11,678, doi:10.1002/ 2016JD025251, 2016.

Prather, K. a, Bertram, T. H., Grassian, V. H., Deane, G. B., Stokes, M. D., Demott, P. J., Aluwihare, L. I., Palenik, B. P., Azam, F., Seinfeld, J. H., Moffet, R. C., Molina, M. J., Cappa, C. D., Geiger, F. M., Roberts, G. C., Russell, L. M., Ault, A. P., Baltrusaitis, J., Collins, D. B., Corrigan, C. E., Cuadra-Rodriguez, L. a, Ebben, C. J., Forestieri, S. D., Guasco, T. L., Hersey, S. P., Kim, M. J., Lambert, W. F., Modini, R. L., Mui, W., Pedler, B. E., Ruppel, M. J., Ryder, O. S., Schoepp, N. G., Sullivan, R. C. and Zhao, D.: Bringing the ocean into the laboratory to probe the chemical complexity of sea spray aerosol., Proc. Natl. Acad. Sci. U. S. A., 110(19), 7550–5, doi:10.1073/pnas.1300262110, 2013.

Pruppacher, H. R. and Klett, J. D.: Microphysics of Clouds and Precipitation, edited by R. D. Rosen, Kluwer Academic Publishers., 1997.

Rosenfeld, D., Lohmann, U., Raga, G. B., O'Dowd, C. D., Kulmala, M., Fuzzi, S., Reissell, A. and Andreae, M. O.: Flood or Drought: How Do Aerosols Affect Precipitation?, Science (80-.)., 321(5894), 1309–1313, doi:10.1126/science.1160606, 2008.

Sear, R. P.: Generalisation of Levine ' s prediction for the distribution of freezing temperatures of droplets : a general singular model for ice nucleation, Atmos. Chem. Phys., 13, 7215–7223, doi:10.5194/acp-13-7215-2013, 2013.

Sullivan, R. C., Miñambres, L., DeMott, P. J., Prenni, A. J., Carrico, C. M., Levin, E. J. T. and Kreidenweis, S. M.: Chemical processing does not always impair heterogeneous ice nucleation of mineral dust particles, Geophys. Res. Lett., 37(24), doi:10.1029/2010GL045540, 2010a.

Sullivan, R. C., Petters, M. D., DeMott, P. J., Kreidenweis, S. M., Wex, H., Niedermeier, D., Hartmann, S., Clauss, T., Stratmann, F., Reitz, P., Schneider, J. and Sierau, B.: Irreversible loss of ice nucleation active sites in mineral dust particles caused by sulphuric acid condensation, Atmos. Chem. Phys., 10(23), 11471–11487, 2010b.

Turner, M. A., Arellano, F. and Kozloff, L. M.: Three separate classes of bacterial ice nucleation structures, J. Bacteriol., 172(5), 2521–2526, 1990.

Vali, G.: Quantitative Evaluation of Experimental Results an the Heterogeneous Freezing Nucleation of Supercooled Liquids, J. Atmos. Sci., 28(3), 402–409, doi:10.1175/1520-0469(1971)028<0402:QEOERA>2.0.CO;2, 1971.

Vali, G.: Freezing Rate Due to Heterogeneous Nucleation, J. Atmos. Sci., 51(13), 1843–1856,

doi:10.1175/1520-0469(1994)051<1843:FRDTHN>2.0.CO;2, 1994.

Vali, G.: Repeatability and randomness in heterogeneous freezing nucleation, Atmos. Chem. Phys., 8(16), 5017–5031, doi:10.5194/acp-8-5017-2008, 2008.

Vali, G.: Interpretation of freezing nucleation experiments: Singular and stochastic; Sites and surfaces, Atmos. Chem. Phys., 14(11), 5271–5294, 2014.

Vali, G. and Snider, J. R.: Time-dependent freezing rate parcel model, Atmos. Chem. Phys., 15(4), 2071–2079, doi:10.5194/acp-15-2071-2015, 2015.

Vali, G. and Stransbury, E. J.: Time Dependant Charactirisitcs of the Heterogeneous Nucleation of Ice, Can. J. Phys., 44(3), 477–502, 1966.

Vali, G., DeMott, P. J., Möhler, O. and Whale, T. F.: Technical Note: A proposal for ice nucleation terminology, Atmos. Chem. Phys., 15(18), 10263–10270, doi:10.5194/acp-15-10263-2015, 2015.

Welti, A., Lund, F., Stetzer, O. and Lohmann, U.: Influence of particle size on the ice nucleating ability of mineral dusts, Atmos. Chem. Phys., 9(18), 6705–6715, 2009.

Welti, A., Lüönd, F., Kanji, Z. A., Stetzer, O. and Lohmann, U.: Time dependence of immersion freezing: an experimental study on size selected kaolinite particles, Atmos. Chem. Phys., 12(20), 9893–9907, doi:10.5194/acp-12-9893-2012, 2012.

Wex, H., Augustin-Bauditz, S., Boose, Y., Budke, C., Curtius, J., Diehl, K., Dreyer, a., Frank, F., Hartmann, S., Hiranuma, N., Jantsch, E., Kanji, Z. a., Kiselev, a., Koop, T., Möhler, O., Niedermeier, D., Nillius, B., Rösch, M., Rose, D., Schmidt, C., Steinke, I. and Stratmann, F.: Intercomparing different devices for the investigation of ice nucleating particles using Snomax® as test substance, Atmos. Chem. Phys., 15(3), 1463–1485, doi:10.5194/acp-15-1463-2015, 2015.

Wheeler, M. J. and Bertram, A. K.: Deposition nucleation on mineral dust particles: A case against classical nucleation theory with the assumption of a single contact angle, Atmos. Chem. Phys., 12(2), 1189–1201, doi:10.5194/acp-12-1189-2012, 2012.

Worringen, a., Kandler, K., Benker, N., Dirsch, T., Mertes, S., Schenk, L., Kästner, U., Frank, F., Nillius, B., Bundke, U., Rose, D., Curtius, J., Kupiszewski, P., Weingartner, E., Vochezer, P., Schneider, J., Schmidt, S., Weinbruch, S. and Ebert, M.: Single-particle characterization of ice-nucleating particles and ice particle residuals sampled by three different techniques, Atmos. Chem. Phys., 15(8), 4161–4178, doi:10.5194/acp-15-4161-2015, 2015.

Wright, T. P. and Petters, M. D.: The role of time in heterogeneous freezing nucleation, J. Geophys. Res. Atmos., 118(9), 3731–3743, 2013.

Wright, T. P., Petters, M. D., Hader, J. D., Morton, T. and Holder, A. L.: Minimal cooling rate dependence of ice nuclei activity in the immersion mode, J. Geophys. Res. Atmos., 118(18), 10,535-10,543, doi:10.1002/jgrd.50810, 2013.

Yankofsky, S. a., Levin, Z., Bertold, T. and Sandlerman, N.: Some Basic Characteristics of Bacterial Freezing Nuclei, J. Appl. Meteorol., 20(9), 1013–1019, doi:10.1175/1520-0450(1981)020<1013:SBCOBF>2.0.CO;2, 1981.

Zobrist, B., Koop, T., Luo, B. P., Marcolli, C. and Peter, T.: Heterogeneous ice nucleation rate coefficient of water droplets coated by a nonadecanol monolayer, J. Phys. Chem. C, 111(1), 2149–2155, doi:10.1021/jp066080w, 2007.

Chapter 3: On the peculiar freezing behavior of Snomax bacterial particles and heterogeneous ice nucleating mixtures

Abstract

Some biological particles, such as Snomax, have been shown to be very efficient ice nuclei, inducing heterogeneous freezing in supercooled water at temperatures above -15 °C and up to -2 °C. Despite their exceptional freezing abilities, large uncertainties remain about the abundance of biological ice nucleating particles, and their contribution to atmospheric ice nucleation and consequent impacts on mixed phase clouds. It has been suggested that small biological ice nucleating macromolecules or fragments can be deposited on dust surfaces to form a mixture with the ice nucleating abilities of the original biological particles.

Starting from the new $\bar{g}$ framework developed in the previous chapter, a heterogeneous ice nucleation mixing model is developed that can predict the freezing behavior of multi-component particle surfaces immersed in droplets. The model successfully predicts the behavior of Snomax bacterial particle containing droplets across a concentration range of 7 orders of magnitude, by assuming that Snomax is comprised of two distinct distributions of heterogeneous ice nucleating activity. Furthermore, the model successfully predicts the freezing behavior of a mixture of low concentration Snomax and illite mineral particles, a proxy for the biological-dust mixtures observed in atmospheric aerosol measurements. It is shown that even at the limit of Snomax availability, the freezing behavior of the droplets freezing at higher temperatures are still determined by the stronger nucleating range of the second more active Snomax distribution of ice active sites, while droplets freezing at lower temperatures are determined by the ice active site distribution of illite. The result emphasizes that in this proxy system, biological particles do not

compromise their ice nucleating efficiency upon mixing with dust and no new range of freezing temperatures associated with the mixture temperatures is produced.

3.1 Introduction

The potential role certain biological particles may play in cloud physics, meteorology, and global climate has been an active area of research for decades (Ariya et al., 2009; Franc and Demott, 1998; Möhler et al., 2007; Morris et al., 2004; Schnell and Vali, 1976). Biological particles such as *Pseudomonas syringae* bacteria can induce freezing in supercooled water at temperatures as high as -2 °C (Hartmann et al., 2012; Wex et al., 2015). While mineral dust particles are the leading candidate for the most abundant and effective ice nuclei in the atmosphere (Hoose et al., 2008; Murray et al., 2012), lidar and radar measurements (Bühl et al., 2013), precipitation samples (Christner et al., 2008; Petters and Wright, 2015), and *in situ* ice crystal residual sampling (Pratt et al., 2009) have all shown that droplet freezing can occur at temperatures higher than -12 °C. This is a temperature range no investigated mineral samples (or other non-biological particles) can induce freezing in (Cantrell and Heymsfield, 2005). All this evidence points to some potentially important role of biological particles in atmospheric ice nucleation, however significant constraints are still needed to properly account for its contribution to the total atmospheric ice nuclei (IN) burden and distribution (Möhler et al., 2007).

Schnell and Vali (1976) hypothesized that mineral dust particles can act as inert carriers of biological IN. Decades later the hypothesis is still gaining support with recent findings suggesting that biological particles release small ice nucleating macromolecules or fragments which can be easily lofted and transported on mineral dust surfaces (Augustin-Bauditz et al., 2016; O'Sullivan et al., 2015; Prather et al., 2013). Given all this emerging evidence of the existence of a heterogeneous ice nucleating (HIN) bio-dust mixture, research on quantifying the HIN properties of bio-dust mixtures in the laboratory remains sparse. Recently, Augustin-Bauditz et al. (2016)

investigated the mixing state and HIN activity of illite NX mineral particles mixed with birch pollen wash water using the Leipzig Aerosol Cloud Interaction Simulator (LACIS). They found that when birch pollen existed on the dust surface, the freezing was determined by the biological material. While a seemingly obvious result, it is a worthwhile endeavor to investigate whether a mixture as such can produce a freezing regime (a range of freezing temperatures) that isn't observed when each of the IN species is probed individually. This helps to determine if the chemical mixing state can modify each individual component's distribution of HIN activity, or if the total activity is just a linear addition of that of the individual components.

In Chapter 2, the concepts of internal variability and external variability in HIN activity were introduced and were shown to have a dramatic impact on the temperature range a droplet population freezes in. If the same distribution of HIN activity is contained within each particle in an aerosol population, then the range of temperatures over which these particles cause freezing in the droplets they are contained in is at most a couple of degrees Celcius. On the other hand, if the distribution of ice nucleating activity is completely distributed among the different particles, then the range of temperatures over which these particles induce freezing could be 5 degrees or more. This was best exemplified when analyzing systems like NX illite, in which upon reducing the surface area the external variability was increased and the range of temperatures over which droplets froze increased. Ervens and Feingold (2012) conducted a unique comprehensive numerical study in which different HIN treatments were compared in a cloud air parcel model. A close examination of the impact of variability in HIN activity was performed, whereby different HIN schemes – that inherently make assumptions about whether HIN activity is externally variable or internally variable – were compared. For example the alpha-PDF scheme (Welti et al., 2012) assumes total external variability, while an internally mixed soccer ball model (Niedermeier et al.,

2011) assumes total internal variability (both treatments were reviewed in the previous chapter). The different schemes resulted in a difference of a factor of 3 in the ice crystal concentration following cloud glaciation. The ice water content (IWC) distribution with height was also different, whereby the alpha-PDF scheme resulted in higher variability in IWC with height due to it causing droplet freezing over a wider temperature range.

While the chemical mixing state and HIN variability are not one in the same, the two properties are certainly relatable. If an aerosol population is chemically diverse and this diversity is externally distributed, then the freezing capabilities of the entire particle population would need to be defined by many different distributions of HIN activity. This becomes more significant with components exhibiting very different HIN properties. A completely internally mixed aerosol particle population on the other hand can imply total internal variability in HIN activity. In considering illite NX for example, this widely used proxy for atmospheric mineral dust is composed of illite clay along with other amounts of kaolinite, quartz, calcite, and feldspars minerals (Hiranuma et al., 2015). Despite this chemically diverse profile, one distribution of HIN activity $\bar{g}$ was sufficient to accurately describe the freezing behavior of illite NX over many orders of magnitude of particle surface area (above a certain critical total surface area threshold) as was shown in the previous chapter. While it remains to be shown, the increase of external variability with decreasing surface area may have been due to the alteration of the chemical mixing state of the different chemical species making up NX illite. Going back to bio-dust mixtures, it would be likely that in a totally internally variable mixture the HIN activity is simply determined by the biological particles given their much higher HIN activity. But what is less clear is what happens in the limit of very low biological particle concentrations and relatively high mineral dust particle concentrations. Does the system then behave as an externally variable system in which the droplets containing biological

particles freeze according to the HIN activity of the biological surfaces while the rest of the droplets freeze as dictated by the dust? Or do the low biological particle concentrations generate a new range of ice nucleation critical temperatures lying between the characteristic temperatures of the two individual and separated particle components?

This chapter extends the heterogeneous ice nucleation model presented in the previous chapter to droplet systems comprised of different HIN components. The extended treatment is then used to model the freezing behavior of Snomax, a freeze-dried powder manufactured from nonviable *Pseudomonas syringae* bacteria, immersed in droplets and placed a cold plate. Snomax's ice nucleation properties are attributed to large protein aggregates, and it is often used as a proxy for atmospheric biological ice nuclei (Pandey et al., 2016; Polen et al., 2016; Wex et al., 2015). It is argued that Snomax in itself is a mixture and necessitates the extended mixing model to properly encompass its entire freezing spectrum. The notion that Snomax is a mixture of nuclei of different strengths is consistent with the hypothesis that the substance is composed of proteins of different strengths and abundances, particularly the Type I and Type III protein aggregates, that exhibit different freezing temperatures (Hartmann et al., 2012; Turner et al., 1990; Yankofsky et al., 1981). The extended model is then applied to a mixture of illite and Snomax at varying abundances of the latter to shed light on how well can these two different regimes of HIN activity remain indistinguishable and what the consequent atmospheric implications are.

3.2 Methods

3.2.1 Experimental ice nucleation measurements

The cold plate assay used to retrieve the freezing spectra for this study is similar to what was described in the previous chapter and in Polen et al. (2016). Some upgrades to the system have taken place, mainly the use of a two-stage thermoelectric cooling (TEC) system comprised of an enclosed air cooled three-stage cascade cold plate (TECA AHP-1200CAS) mounted below a single-stage TEC module (TeTech VT-127-1.0-1.3-71) and the custom-built cold plate chamber. An aluminum dish is placed in the chamber inside which a hydrophobic glass coverslip is immersed in squalene oil. An electronic 0.1 μl pipette (Sartorius eLINE) has also been recently introduced to help keep droplet sizes more consistent, which aids in reducing the total particle surface area variability between individual droplets.

A solution of ultapure Milli-Q water and the particle material being investigated is prepared, from which 40-50 0.1 μl droplets are generated using the electronic pipette and placed on the coverslip immersed in the oil. A cooling rate of 1 K/min is used and images of the droplet array are collected at a rate of 1 image/second using an optical microscope and CMOS camera. The images are then used to deduce the fraction of droplets frozen at each temperature. The droplets appear black when frozen. Each freezing experiment was repeated at least twice to confirm that the independently retrieved frozen fractions fall within 1 K (the temperature measurement uncertainty) of each other for each replicate experiment. The samples used in this study were commercial Snomax and NX illite (Arginotec, NX nanopowder). The illite samples are identical to the ones analyzed in the previous chapter and therefore the HIN properties derived there are reused for the analysis here. However, the Snomax samples in this study exhibit different HIN properties than the ones from the previous chapter due to the Snomax sample used here being more recently acquired. As shown in Polen et al. (2016), over time the freezing properties of Snomax are altered, where the most active IN that freeze at the warmest temperatures near -4 °C degrade

during storage over months. Hence the frozen fraction curves retrieved from droplets containing Snomax are reanalyzed in this chapter.

3.2.2. Mixing model

The mixing model extends the HIN framework developed earlier in this dissertation to account for multiple ice nucleation activities caused by multiple IN species inside a single droplet as well as the homogenous ice nucleation probability defined in Section 2.2. It is assumed that every probability is independent of the other, an approach similar to the one taken by Augustin-Bauditz et al. (2016). The freezing probability of an individual droplet containing some mixture of components n_c+n_{sc}, where n_c is the number of components with surface areas greater than their corresponding critical surfaces and n_{sc} is the number of components with surface areas lower than their corresponding critical surface areas, is:

$$P_f = 1 - P_{uf,hom} \prod_{k=1}^{n_c} P_{uf\_c,k}(\bar{g}_k, A_k) \prod_{j=1}^{n_{sc}} P_{uf\_sc,j}(g^*{}_j, A_j) \qquad (1)$$

where $P_{uf,hom}$ is the probability freezing does not occur due to homogenous nucleation, $P_{uf\_c,k}$ is the probability freezing does not occur due to component k possessing a surface area A_k lying above this component's critical area and thus can be evaluated with $\bar{g}_k$, and $P_{uf\_sc,j}$ is the probability freezing does not occur due to component j possessing a surface area A_j lying below this component's critical surface area and thus requires random sampling from $\bar{g}_j$ to generate $g^*{}_j$ and be evaluated.

For a large ensemble of N droplets, the frozen fraction F is the mean of the individual droplet freezing probabilities. This yields the following expression for F:

$$F = 1 - \frac{1}{N}\sum_{i=1}^{N}\left|\exp\left(-\frac{1}{\dot{T}}\int_{T_i}^{T_f}\left(J_{hom}V + \sum_{k=1}^{n_c} A_k \int_0^{\pi} \bar{g}_k(\theta)J(\theta,T)\,d\theta + \sum_{j=1}^{n_{sc}} A_j \int_0^{\pi} g^*_{i,j}\left(\bar{g}_j, n_{draws,j}\right)J(\theta,T)d\theta\right)dT\right)\right| \quad (2)$$

where $\dot{T}$ is the cooling rate, T_i and T_f are the initial and final temperatures in a cooling experiment, J_{hom} is the homogenous nucleation rate, V is the droplet volume, and $n_{draws,j}$ is the number of times random sampling takes place from $\bar{g}_j$. An additional subscript i is added to g^* to indicate that the sub-critical area distribution for a component k will vary between droplets.

For the purposes of the analysis of the experiments presented in this chapter, Eq. (2) can be reduced to describe one component exhibiting behavior above the critical area, one component exhibiting behavior below the critical area, and the background HIN distribution of impurities in the species being examined or the Milli-Q water itself. The latter does not follow homogenous ice nucleation but causes freezing to happen at a much higher temperature. Eq. (2) is thus reduced to:

$$F = 1 - \frac{1}{N}\sum_{i=1}^{N}\left|\exp\left(-\frac{1}{\dot{T}}\int_{T_i}^{T_f}\left(A_1 \int_0^{\pi} g^*_{i,1}\left(\bar{g}_j, n_{draws,j}\right)J(\theta,T)d\theta + A_2 \int_0^{\pi} \bar{g}_2(\theta)J(\theta,T)\,d\theta + \int_0^{\pi} G_{bg}(\theta)J(\theta,T)d\theta\right)dT\right)\right| \quad (3)$$

It should be noted that the distribution of ice nucleating activity of the background impurities has been lumped with its particle surface area into one term G_{bg}. This simplification serves the same purpose of simply accounting for droplet freezing that could be occurring due to background

impurities. The contribution from this term becomes particularly important at low particle concentrations.

3.3 Snomax: Two distributions of heterogeneous ice nucleating activity

The HIN behavior of Snomax was investigated by varying the concentration of the prepared particle suspension to retrieve the full freezing temperature spectrum of the system. These measurements have been conducted and analyzed before as summarized in Wex et al. (2015). However, the analysis presented here is unique due to the application of the newly developed critical area method discussed in the previous chapter. Freezing spectra for Snomax mass concentrations of 0.1 wt%, 0.5 wt%, 0.3 wt%, 0.1 wt%, 0.05 wt%, 0.01 wt%, 0.005 wt%, 0.001 wt%, 0.0005 wt%, 0.0001 wt%, 0.00001 wt%, and 0.000001 wt% were obtained and are plotted in Fig. 3.1.

For concentrations 0.1 wt% through 0.0005 wt% the temperatures over which droplets freeze gradually broadens and decreases as the concentration of Snomax is decreased. This is consistent with the trend observed with the systems analyzed in the previous chapter in which the broadening is interpreted as particle surface areas becoming smaller than the species' critical area, which leads to external variability in the HIN activity of the particle surfaces. The first two concentrations (0.1 wt% and 0.05 wt%) can be fitted with the same g distribution (solid lines indicate a single g fit), but at concentrations lower than these a single g fit fails at capturing the freezing behavior of the freezing curves (the behavior is defined by the temperature at which 50% of the droplets freeze and the range of temperatures over which droplets freeze). The broadening trend continues with decreasing particle concentration until the 0.0001 wt% Snomax concentration, whereby a sharp (narrow range of freezing temperatures) freezing curve reemerges. The g distribution that fits this

low concentration freezing curve is different than the g distribution that fits the first two high concentration freezing curves (with the appropriate surface area correction). Furthermore, the g distribution of the 0.0001 wt% freezing curve also fits the 0.00001 wt% freezing curve before a new trend of frozen fraction curve broadening emerges starting with the 0.000001 wt% concentration. Figure 3.2 expands the temperature range of the frozen fraction curves to show the unique trend of the very low concentration freezing curves (0.0000005 wt% and 0.0000001 wt%). Only a part of these frozen fraction curves exhibits broadening and freezing at high temperatures beyond which there is an approximate plateau with further droplet freezing. The plateau ends around a similar temperature range for both low particle concentrations and they converge around what is probably HIN activity due to background impurities in the water or the sample.

Based on these observations, it is hypothesized that Snomax can be modelled as having two distinct distributions of HIN activity, each possessing its own critical area. Using the fits to the frozen fraction curves of the 0.1 %wt and the 0.05 wt% Snomax concentrations, the first distribution denoted $\bar{g}_1$ is a normal distribution with parameters $\mu_1 = 0.6$ and $\sigma_1 = 0.05$. Similarly, the fits to the frozen fraction curves of the 0.0001 wt% and 0.00001 wt% Snomax concentrations give the second distribution of HIN activity denoted $\bar{g}_2$ with parameters $\mu_2 = 0.52$ and $\sigma_2 = 0.0001$. For this analysis it is assumed that all HIN components of Snomax have surface area densities of 1 g/m^2, an identical assumption to the one made for the Snomax analysis in the previous chapter.

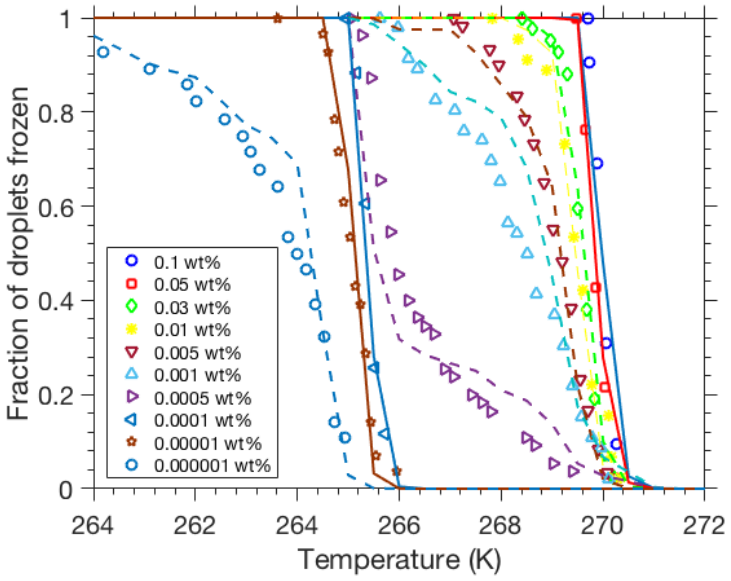

Figure 3.1. Frozen fraction temperature spectra for Snomax mass concentrations of 0.1 wt%, 0.5 wt%, 0.3 wt%, 0.1 wt%, 0.05 wt%, 0.01 wt%, 0.005 wt%, 0.001 wt%, 0.0005 wt%, 0.0001 wt%, 0.00001 wt%, and 0.000001 wt% (symbols). Critical area fits using two distinct Snomax distributions of HIN activity (solid lines) while the rest of the freezing curves are modelled with the mixing model (dashed lines).

The particle concentrations corresponding to the frozen fraction curves between the two steep sets of frozen fraction curves are thus considered to exhibit HIN distributions below the first critical area and above the second critical area. Modelling these freezing curves is thus the first application of the extended mixing model summarized in Eq. (3). The g^* distributions for the first term inside the exponential in Eq. (3) are retrieved by taking a number of random θ values, n_{draws}, from $\bar{g}_1$, whereby each frozen fraction curve will have a unique n_{draws} that produces a modelled frozen fraction curve closest to the measured one. In the case of the mixture of two Snomax HIN distributions, A_1 is assumed equal to A_2 and is calculated from the Snomax concentration and the assumed surface area density. The last term corresponding to the HIN activity of background

impurities can be safely neglected here as the freezing temperatures are much higher than temperatures at which the Milli-Q water typically freezes in this system. The consequent n_{draws} for each frozen fraction curve between the two Snomax critical areas are: 80 for the 0.03 wt%, 65 for 0.01 wt%, 40 for 0.005 wt%, 35 for 0.001 wt%, and 11 for 0.0005 wt%. The modelled frozen fraction curves are plotted in dotted lines in Fig. 3.1.

A similar analysis was performed to model the frozen fraction curves with surface areas below the second critical area, which correspond to Snomax concentrations of 0.000001 wt%, 0.0000005 wt%, and 0.0000001 wt%. In this case Eq. (3) is used without the contribution from a component with a surface area larger than its own critical area (the second term inside the exponential). Random sampling to produce the g^* distributions is done from $\bar{g}_2$. The HIN activity of background impurities has an important contribution here as can be seen in Fig. 3.2 with all three frozen fraction curves with surface areas below the second critical surface area finishing freezing along the same low temperature freezing line. This freezing line is assumed to be due to the HIN activity of the background impurities. It should be noted however that this freezing line is not reproducible when retrieving the frozen fraction curve of droplets made up only of Milli-Q water, which freeze 5 degrees colder. It was also not possible to reproduce this background frozen fraction with a newly acquired batch of Snomax. Therefore, it is likely that these impurities are associated with this particular Snomax sample, so their resultant frozen fraction curve will simply be added to the mixing model in the form of G_{bg}. G_{bg} is derived by extrapolating the low temperature part of the frozen fraction curve of the lowest Snomax concentration (solid blue line). The resultant parameters are $\mu_{bg} = 2.8$ and $\sigma_{bg} = 0.25$ and a pre-factor of $2.5\text{x}10^{-6}$. The consequent n_{draws} for each frozen fraction curve below the second Snomax critical area are: 8000 for 0.000001 wt%, 2800 for 0.0000005 wt%, and 750 for 0.0000001 wt%. The much higher n_{deaws} values for this

range of concentrations is due to the much narrower range of HIN activity distribution 2 covers compared to distribution 1 (σ_2 is much smaller than σ_1). A larger number of draws from $\bar{g}_2$ is therefore required to capture any HIN activity.

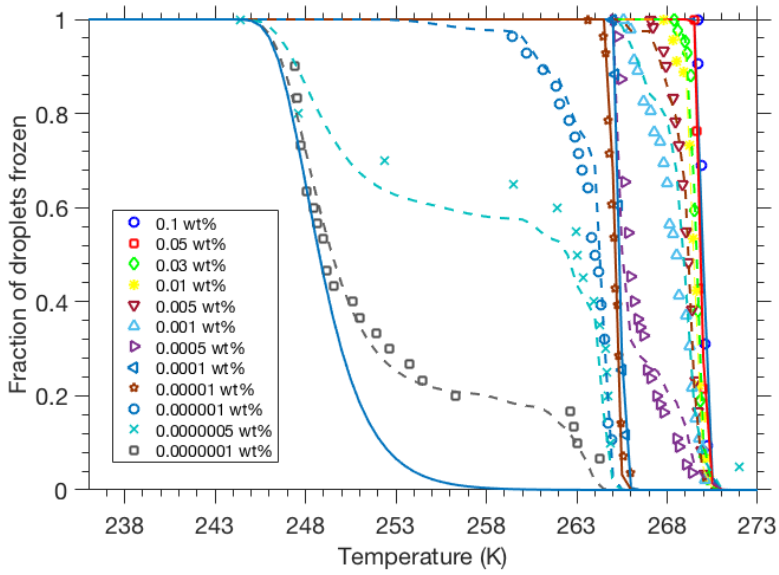

Figure 3.2. All frozen fraction curves shown in Fig. 3.1 in addition to the lowest Snomax concentration frozen fraction curves of 0.0000005 wt% and 0.0000001 wt%. The lowest concentration freezing curves are modelled using random sampling. The solid blue line is the assumed frozen fraction curve of the background impurities in the droplets.

Figure 3.3 shows the two Snomax $\bar{g}$ distributions plotted alongside each other for comparison. The most striking contrast is the σ for each distribution, which defines the range of contact angles a g distribution covers. Typically, a larger σ does lead to a broader range of temperatures a frozen fraction curve with a surface area larger than its critical area covers. However, for the same σ, frozen fraction curves at higher temperatures are steeper than at lower temperatures, due to the strength of the range of HIN activity causing higher temperature freezing. While merely looking

at the frozen fraction curves dictated exclusively by either $\bar{g}_1$ or $\bar{g}_2$ would hint at similar HIN activity contact angle breadth, it should be emphasized that the contact angle range for $\bar{g}_2$must be narrower due to it causing freezing at lower temperatures. In other words, if $\bar{g}_1$was used to try and fit the frozen fraction curves associated with $\bar{g}_2$, the consequent fit would not only overpredict the freezing temperature but also the range of temperatures over which freezing would occur. Figure 4.4 shows a fit for the 0.0001 wt% frozen fraction curve that uses $\bar{g}_1$instead of $\bar{g}_2$. The required surface area input for this fit is 8 orders of magnitude smaller than the surface area used for the 0.1 wt% frozen fraction curve instead of 3 orders of magnitude, which points to the much stronger HIN activity of $\bar{g}_1$. Further the range of temperatures over which freezing occurs is broader, which highlights the point made above. This analysis is done to further justify the resultant parameters of $\bar{g}_1$ and $\bar{g}_2$, particularly the σ of each.

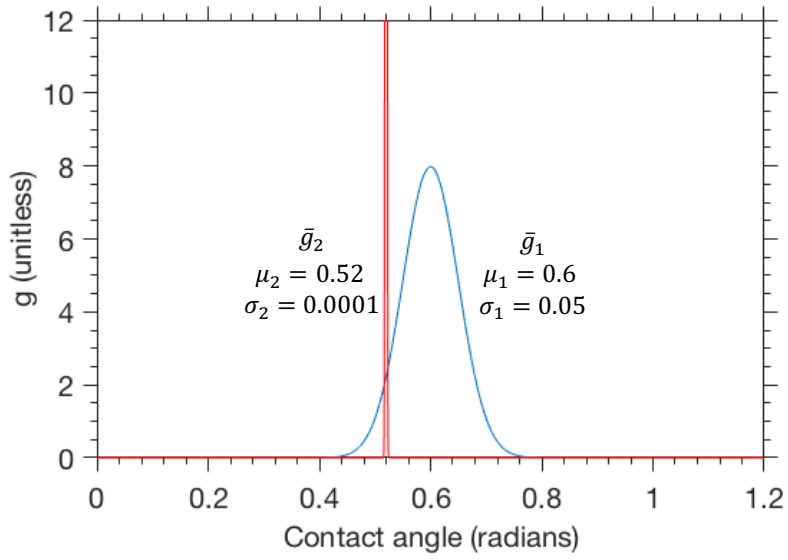

Figure 3.3. $\bar{g}_1$ and $\bar{g}_2$, the two distributions of HIN activity retrieved from the Snomax droplet freezing spectra (Figs. 1 & 2), plotted alongside each other for comparison.

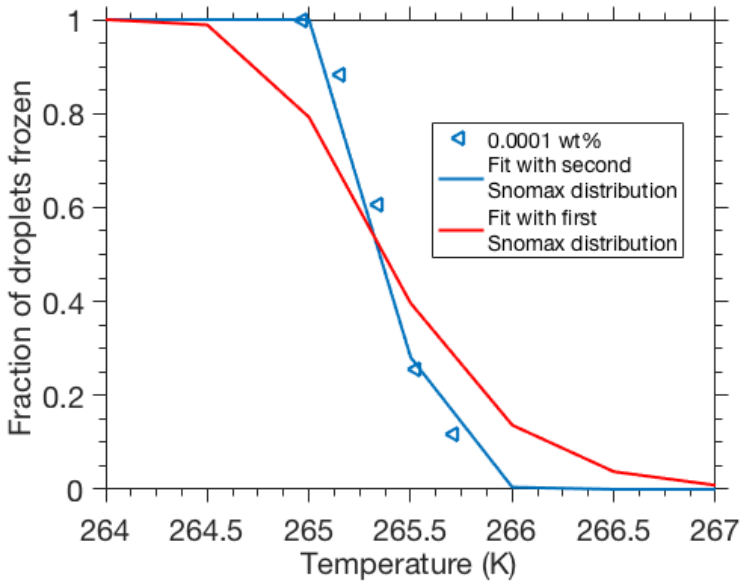

Figure 3.4. The 0.0001 wt% frozen fraction curve (first frozen fraction curve corresponding to freezing exclusively determined by the $\bar{g}_2$ distribution of HIN activity) shown with its $\bar{g}_2$ fit and a hypothetical fit corresponding to the activity of the $\bar{g}_1$ activity distribution.

A narrower σ for the $\bar{g}_2$distribution is also reflected in the very abrupt transition in freezing behavior that droplets containing low Snomax concentrations undergo with decreasing concentration. After a second Snomax critical area regime covers 2 orders of magnitude in concentration (0.0001 wt% and 0.00001 wt%) a sub-critical area regime begins (the broader 0.000001 wt% frozen fraction curve) followed by a very quick transition to (only a factor of 5) a loss of Snomax HIN activity in at least 60% of the droplets (0.0000005 wt% frozen fraction curve). While frozen fraction curves lying between critical area 1 and critical area 2 covered two orders of magnitude in concentration before partial loss of HIN activity due to $\bar{g}_1$, frozen fraction curves lying below critical area 2 covered only one order of magnitude. Furthermore, the continually dominant contribution from the contact angle range causing freezing at a high temperature of about -265 K to -263 K also points to a narrow second distribution of HIN activity. This can be seen in

the transition between 0.000001 wt% to 0.000005 wt% and eventually 0.0000001 wt% whereby the higher temperature freezing (265 K to 263 K) is retained better than lower temperature freezing (263 K to 258 K). However, it should be noted that the existence of some broadness in the temperature over which droplets freeze throughout the regime falling below the second critical area does necessitate that $\bar{g}_2$ still have a finite σ, albeit a small one.

3.4 Snomax-Illite mixtures

The second part of this study was to investigate the applicability of the mixing model to a mixture of Snomax and illite particles. Figure 3.5 shows two frozen fraction curves retrieved from droplets generated from a mixture of Snomax and illite: a 50:50 mixture of 0.0000005 wt% Snomax and 0.06 wt% illite and a 50:50 mixture of 0.0000001 wt% Snomax and 0.06 wt% illite. The two curves are plotted along with the other Snomax frozen fraction curves and a frozen fraction curve retrieved from droplets prepared from a 0.03 wt% Snomax suspension. As the Snomax-illite mixtures were prepared by mixing equal amounts of each component, the effective concentration of each is half its original concentration. That is why a 0.03 wt% illite frozen fraction curve is included in Fig. 2.5 as it should better resemble the illite concentration in the mixture. It was shown in the previous chapter that for this method and a 0.03 wt% illite concentration, the resultant freeze curve can be fitted using illite's retrieved $\bar{g}$ ($\mu_{illite} = 1.72, \sigma_{illite} = 0.122,$ and A_{illite}=2.0 x 10^{-2} cm^2). This fit using illite's $\bar{g}$ distribution is also shown in Fig. 2.5.

The mixing model summarized in Eq. (3) is applied to the droplet frozen fraction curves corresponding to a mixture of Snomax and illite. In this case the contribution from the background impurities is ignored, which is thought to be a good assumption as the tail of the frozen fraction curves aligns quite well with the frozen fraction curve for droplets containing 0.03 wt% illite.

Random sampling takes place from $\bar{g}_2$ to produce the g^* distributions needed for the first term inside the exponential in Eq. (3), while the second term uses $\bar{g}_{illite}$ and A_{illite} that were previously determined as discussed above. The consequent n_{draws} that result in the best fits for each of the frozen fraction curves produced from a Snomax-illite mixture are: 1190 for 0.0000005 wt% Snomax mixed with 0.06 wt% illite, and 500 for 0.0000001 wt% Snomax mixed with 0.06 wt% illite.

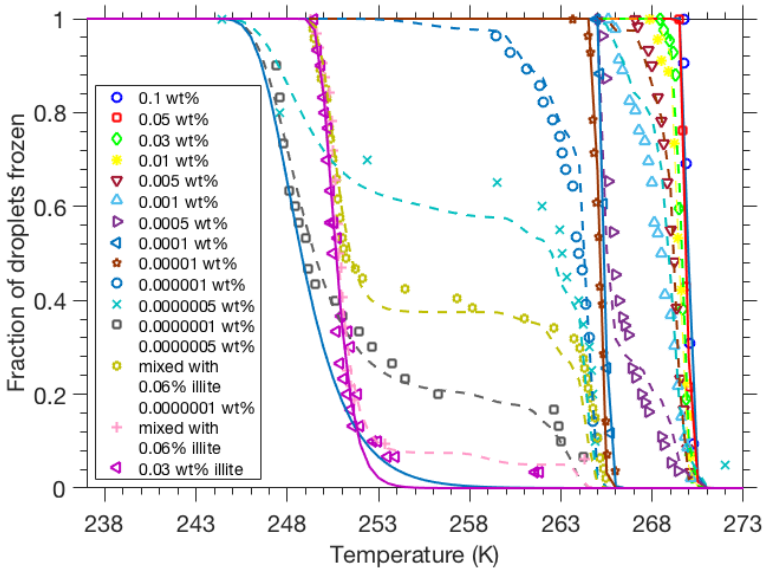

Figure 3.5. All droplet freezing spectra for Snomax-containing droplets shown in Fig. 3.2 along with the frozen fraction curves corresponding to 0.03 wt% illite, a 50:50 mixture of 0.0000005 wt% Snomax and 0.06 wt% illite, and a 50:50 mixture of 0.0000001 wt% Snomax and 0.06 wt% illite. The fit for the 0.03 wt% illite frozen fraction curve is also plotted (solid line) along with the fits for the frozen fraction curves corresponding to the illite-Snomax mixtures (dashed lines).

Due to Snomax's well-defined cutoff in HIN activity at low concentrations there is really no regime in which illite and Snomax ice nuclei compete. In other words, it is not possible to dilute Snomax to a point where its HIN activity is in the temperature range where illite's HIN activity becomes significant. The measurements do clearly indicate that there is a high temperature cutoff for Snomax's contribution to freezing and the model does a good job of producing this behavior. In theory, a converse measurement can be done in which the concentration/surface area of illite is increased to match the HIN activity of Snomax that would allow a direct measure of how much the HIN activity of Snomax is stronger than illite's. Such a measurement is difficult with the current method due to particle material saturation within the droplets that causes coagulation and sedimentation and thus loss of IN, as discussed in detail in the previous chapter. While the measurement can be insightful in the context of heterogeneous ice nucleation, it would not be atmospherically relevant as it would be examining illite particle sizes that are too large. Using the $\bar{g}_{illite}$ distribution of its HIN activity, illite particle surface areas need to be around 0.1 m^2 to match the HIN activity of the second Snomax distribution and 10000 m^2 to match that of the first distribution. These material surfaces no longer correspond to any kind of reasonable particle surface. Based on these theoretical estimates, it could be said that the HIN activity of the first Snomax distribution is 10^{13} times stronger than that of illite while the second Snomax distribution is 10^8 stronger than that of illite. However, these estimates aren't backed by observations and are merely academic as they do not shed any insight on biological particle-dust mixtures in the atmosphere.

Perhaps an atmospherically relevant frozen fraction curve examined that deserves greater attention is the one generated from droplets containing a 50:50 mixture of 0.0000001 wt% Snomax and 0.06 wt% illite. At this effective Snomax concentration of 0.00000005 wt%, the volume

equivalent diameter of total surface area of Snomax particles present is around 550 nm (for an assumed 1 g/cm^3 density). Hartmann et al. (2013) investigated the HIN activity of size selected Snomax particles using the LACIS cloud simulator (Stratmann et al., 2004). Their results were somewhat consistent with what was found here as the 650 nm and 800 nm size-selected particles produced a frozen fraction curve that plateaued at 10% F_{frozen} below 263 K. Smaller Snomax particle sizes they investigated (100 nm, 300 nm, 400 nm) caused freezing at lower temperatures between 263 K and 258 K and were generally found to be rarer than the larger particles in the polydisperse aerosol size distribution. This may explain why upon decreasing Snomax concentrations in the experiments presented here, freezing at the higher temperatures persisted for longer than at the lower concentrations. Therefore, in the context of the atmosphere, at the limit of a very low probability of finding a biological particle, the higher temperature IN of the second Snomax distribution are the most likely to be found (in the limiting assumption of Snomax being a reasonable proxy of biological IN). This is what the lower Snomax concentration frozen fraction curve associated with the Snomax-illite mixture resembles; even when Snomax particles become really rare they retain a high freezing temperature in the small fraction of droplets that still contain them (around 5% in the frozen fraction curve being examined).

The question then of what ratios of Snomax and illite are needed for one to control the HIN activity over the other becomes irrelevant. The existence of any Snomax particle in a droplet will shift the resultant freezing to a much higher temperature regime and no amount of mineral dust can practically compete with that. This is not a ground-breaking finding by any means, but it provides more quantitative validation of the conventional wisdom that a relatively rare biological particle exhibits exceptional freezing behavior, overwhelming other non-biological components. While it remains a subject of further research how many $\bar{g}$ distributions are necessary to encompass

the freezing behavior at low temperatures, two distributions of HIN activity are necessary to distinguish between the dust and biological regimes.

Conclusions

A new heterogeneous ice nucleation mixing model was formulated in this chapter in an effort to better understand how systems with more than one distribution of HIN activity behave. The new model was used to gain insight on the freezing behavior of Snomax as well as a mixture of Snomax and NX-illite, a proxy for bio-dust mixtures in the atmosphere. Snomax was characterized by two distributions of HIN activity, a model consistent with Snomax's hypothesized ice nucleating Type I and Type III protein aggregates. The first distribution exhibited a broader contact angle range and therefore had a more gradual decay rate with decreasing concentration than the second distribution. Interestingly the second distribution exhibited a very narrow range of contact angles, significantly narrower than any other system analyzed by this framework. This went counter to this investigator's expectations, as it seems more intuitive to conceptualize the second distribution as a weaker background distribution with a less sharp and well defined range of HIN activity.

Upon examining droplets containing a mixture of low Snomax concentrations and illite mineral particles, the resultant frozen fractions merely followed freezing determined by the distributions of HIN activity of each component. This result is similar to the one reported in Augustin-Bauditz et al. (2016) using a mixture of birch pollen wash water and illite. The absence of a broad range of nucleating temperatures connecting the two HIN regimes is partly due to the sharpness of the second Snomax distribution of HIN activity. In fact, the weaker ice nucleants in the second Snomax distribution decayed quicker than the stronger nucleants, indicating that at the limit of very low Snomax availability the higher temperature freezers are what are more likely to be found.

Therefore, in the limiting assumption that the system examined here is a close proxy to real atmospheric bio-dust mixtures, it would be safe to assume that the limiter to high temperature heterogeneous freezing in the atmosphere is merely the existence of biological material in the mixture and more likely than not no compromise would be made in the quality of its HIN activity due to the presence of other particle components, such as the illite minerals studied here.

References

Ariya, P. a., Sun, J., Eltouny, N. a., Hudson, E. D., Hayes, C. T. and Kos, G.: Physical and chemical characterization of bioaerosols – Implications for nucleation processes., 28(1), 1-32, doi: org/10.1080/01442350802597438, 2009.

Augustin-Bauditz, S., Wex, H., Denjean, C., Hartmann, S., Schneider, J., Schmidt, S., Ebert, M. and Stratmann, F.: Laboratory-generated mixtures of mineral dust particles with biological substances: characterization of the particle mixing state and immersion freezing behavior, Atmos. Chem. Phys., 16(9), 5531–5543, doi:10.5194/acp-16-5531-2016, 2016.

Bühl, J., Ansmann, A., Seifert, P., Baars, H. and Engelmann, R.: Toward a quantitative characterization of heterogeneous ice formation with lidar/radar: Comparison of CALIPSO/CloudSat with ground-based observations, Geophys. Res. Lett., 40(16), 4404–4408, doi:10.1002/grl.50792, 2013.

Cantrell, W. and Heymsfield, A.: Production of Ice in Tropospheric Clouds: A Review, Bull. Am. Meteorol. Soc., 86(6), 795–807, doi:10.1175/BAMS-86-6-795, 2005.

Christner, B. C., Morris, C. E., Foreman, C. M., Cai, R. and Sands, D. C.: Ubiquity of Biological Ice Nucleators in Snowfall, Science (80-.)., 319(5867), 1214–1214, doi:10.1126/science.1149757, 2008.

Ervens, B. and Feingold, G.: On the representation of immersion and condensation freezing in cloud models using different nucleation schemes, Atmos. Chem. Phys., 12, 5807–5826, doi:10.5194/acp-12-5807-2012, 2012.

Franc, G. D. and Demott, P. J.: Cloud Activation Characteristics of Airborne Erwinia carotovora Cells, J. Appl. Meteorol., 37(10), 1293–1300 [online] Available from: http://journals.ametsoc.org/doi/abs/10.1175/1520-0450(1998)037%3C1293:CACOAE%3E2.0.CO;2, 1998.

Hartmann, S., Augustin, S., Clauss, T., Voigtländer, J., Niedermeier, D., Wex, H. and Stratmann, F.: Immersion freezing of ice nucleating active protein complexes, Atmos. Chem. Phys. Discuss., 12(8), 21321–21353, doi:10.5194/acpd-12-21321-2012, 2012.

Hartmann, S., Augustin, S., Clauss, T., Wex, H., Šantl-Temkiv, T., Voigtländer, J., Niedermeier, D. and Stratmann, F.: Immersion freezing of ice nucleation active protein complexes, Atmos. Chem. Phys., 13(11), 5751–5766, doi:10.5194/acp-13-5751-2013, 2013.

Hiranuma, N., Augustin-Bauditz, S., Bingemer, H., Budke, C., Curtius, J., Danielczok, A., Diehl, K., Dreischmeier, K., Ebert, M., Frank, F., Hoffmann, N., Kandler, K., Kiselev, A., Koop, T., Leisner, T., Möhler, O., Nillius, B., Peckhaus, A., Rose, D., Weinbruch, S., Wex, H., Boose, Y., DeMott, P. J., Hader, J. D., Hill, T. C. J., Kanji, Z. A., Kulkarni, G., Levin, E. J. T., McCluskey, C. S., Murakami, M., Murray, B. J., Niedermeier, D., Petters, M. D., O'Sullivan, D., Saito, A., Schill, G. P., Tajiri, T., Tolbert, M. A., Welti, A., Whale, T. F., Wright, T. P. and Yamashita, K.: A comprehensive laboratory study on the immersion freezing behavior of illite NX particles: a

comparison of 17 ice nucleation measurement techniques, Atmos. Chem. Phys., 15(5), 2489–2518, doi:10.5194/acp-15-2489-2015, 2015.

Hoose, C., Lohmann, U., Erdin, R. and Tegen, I.: The global influence of dust mineralogical composition on heterogeneous ice nucleation in mixed-phase clouds, Environ. Res. Lett., 3(2), 25003, doi:10.1088/1748-9326/3/2/025003, 2008.

Möhler, O., DeMott, P. J., Vali, G. and Levin, Z.: Microbiology and atmospheric processes: the role of biological particles in cloud physics, Biogeosciences Discuss., 4(4), 2559–2591, doi:hal-00297909, 2007.

Morris, C. E., Georgakopoulos, D. G. and Sands, D. C.: Ice nucleation active bacteria and their potential role in precipitation, J. Phys. IV, 121, 87–103, doi:10.1051/jp4:2004121004, 2004.

Murray, B. J., O'Sullivan, D., Atkinson, J. D. and Webb, M. E.: Ice nucleation by particles immersed in supercooled cloud droplets, Chem. Soc. Rev., 41(19), 6519, doi:10.1039/c2cs35200a, 2012.

Niedermeier, D., Shaw, R. a., Hartmann, S., Wex, H., Clauss, T., Voigtländer, J. and Stratmann, F.: Heterogeneous ice nucleation: exploring the transition from stochastic to singular freezing behavior, Atmos. Chem. Phys., 11(16), 8767–8775, doi:10.5194/acp-11-8767-2011, 2011.

O'Sullivan, D., Murray, B. J., Ross, J. F., Whale, T. F., Price, H. C., Atkinson, J. D., Umo, N. S. and Webb, M. E.: The relevance of nanoscale biological fragments for ice nucleation in clouds, Sci. Rep., 5, 8082, doi:10.1038/srep08082, 2015.

Petters, M. D. and Wright, T. P.: Revisiting ice nucleation from precipitation samples, Geophys. Res. Lett., 42(20), 8758–8766, doi:10.1002/2015GL065733, 2015.

Polen, M., Lawlis, E. and Sullivan, R. C.: The unstable ice nucleation properties of Snomax(R) bacterial particles, J. Geophys. Res. - Atmos., 121, 11,666–11,678, doi:10.1002/ 2016JD025251, 2016.

Prather, K. a, Bertram, T. H., Grassian, V. H., Deane, G. B., Stokes, M. D., Demott, P. J., Aluwihare, L. I., Palenik, B. P., Azam, F., Seinfeld, J. H., Moffet, R. C., Molina, M. J., Cappa, C. D., Geiger, F. M., Roberts, G. C., Russell, L. M., Ault, A. P., Baltrusaitis, J., Collins, D. B., Corrigan, C. E., Cuadra-Rodriguez, L. a, Ebben, C. J., Forestieri, S. D., Guasco, T. L., Hersey, S. P., Kim, M. J., Lambert, W. F., Modini, R. L., Mui, W., Pedler, B. E., Ruppel, M. J., Ryder, O. S., Schoepp, N. G., Sullivan, R. C. and Zhao, D.: Bringing the ocean into the laboratory to probe the chemical complexity of sea spray aerosol., Proc. Natl. Acad. Sci. U. S. A., 110(19), 7550–5, doi:10.1073/pnas.1300262110, 2013.

Pratt, K. a., DeMott, P. J., French, J. R., Wang, Z., Westphal, D. L., Heymsfield, A. J., Twohy, C. H., Prenni, A. J. and Prather, K. a.: In situ detection of biological particles in cloud ice-crystals, Nat. Geosci., 2(6), 398–401, doi: org/10.1038/ngeo521, 2009.

Schnell, R. C. and Vali, G.: Biogenic Ice Nuclei: Part I. Terrestrial and Marine Sources, J.

Atmos. Sci., 33(8), 1554–1564, doi:10.1175/1520-0469(1976)033<1554:BINPIT>2.0.CO;2, 1976.

Turner, M. A., Arellano, F. and Kozloff, L. M.: Three separate classes of bacterial ice nucleation structures, J. Bacteriol., 172(5), 2521–2526, doi:PMC208892, 1990.

Welti, A., Lüönd, F., Kanji, Z. A., Stetzer, O. and Lohmann, U.: Time dependence of immersion freezing: an experimental study on size selected kaolinite particles, Atmos. Chem. Phys., 12(20), 9893–9907, doi:10.5194/acp-12-9893-2012, 2012.

Wex, H., Augustin-Bauditz, S., Boose, Y., Budke, C., Curtius, J., Diehl, K., Dreyer, a., Frank, F., Hartmann, S., Hiranuma, N., Jantsch, E., Kanji, Z. a., Kiselev, a., Koop, T., Möhler, O., Niedermeier, D., Nillius, B., Rösch, M., Rose, D., Schmidt, C., Steinke, I. and Stratmann, F.: Intercomparing different devices for the investigation of ice nucleating particles using Snomax® as test substance, Atmos. Chem. Phys., 15(3), 1463–1485, doi:10.5194/acp-15-1463-2015, 2015.

Yankofsky, S. a., Levin, Z., Bertold, T. and Sandlerman, N.: Some Basic Characteristics of Bacterial Freezing Nuclei, J. Appl. Meteorol., 20(9), 1013–1019, doi:10.1175/1520-0450(1981)020<1013:SBCOBF>2.0.CO;2, 1981.

Chapter 4: The design and implementation of a novel chilled optical aerosol tweezers (COAT)

Abstract

Of all heterogeneous ice nucleation modes contact freezing remains the most poorly quantified. This is in large part due to the challenges of controllably colliding a particle and a cloud droplet and observing any consequent freezing. The optical tweezers, which can trap cloud relevant water droplets indefinitely, presents a potential remedy for the challenging measurement as the surface enhanced Raman spectrum can act as a real time collision detector. This chapter presents a novel chilled optical aerosol tweezers (COAT) designed and implemented with the eventual goal of conducting contact freezing measurements. It is shown that the COAT is capable of trapping droplets stably down to subzero temperatures while retaining the cavity enhanced Raman signal. Tests in which a KCl droplet was trapped, cooled to subzero temperatures, and held at a steady freezing temperature validate the system's performance while presenting preliminary findings on a potential gradient in salt concentration from the bulk to the surface of the droplet. The system is shown to be capable of achieving ice supersaturated conditions, a challenging design feature necessary for heterogeneous ice nucleation experiments. Collision tests were conducted in which a stream of Arizona Test Dust (ATD) particles was exposed to a trapped droplet. Both the cavity enhanced Raman spectrum as well as the image of the droplet captured by a camera showed some sensitivity to detecting collisions though the extent to which this information can be converted to a collection efficiency remains to be conclusively determined. Critical COAT system design features, limitation of the current setup, and future directions are discussed.

4.1 Introduction

Great challenges in observing the actual heterogeneous ice nucleation nanoscale process is the main culprit impeding the formulation of a consistent and comprehensive framework that can accurately and efficiently represent heterogeneous ice nucleation in atmospheric models (Cantrell and Heymsfield, 2005). The handful of reliable measurement methods currently being used to study this critical atmospheric process all present significant limitations in their capability to probe the ice nucleating potential of proper proxies of atmospheric aerosol systems (DeMott et al., 2011; Murray et al., 2012). At the forefront of advanced heterogeneous ice nucleation measurement methods are two types of systems, what have been referred to as the wet and dry dispersion methods (Hiranuma et al., 2015). Wet methods are unable to conduct freezing tests on atmospherically relevant particle sizes, while dry methods can only measure the freezing temperatures of particle populations and not individual particles. Further these methods do not test the notoriously ambiguous contact freezing mode of heterogeneous ice nucleation, the proper examination of which requires the capability to controllably collide individual particles with cloud droplets (Gokhale and Spengler, 1972; Hoose and Möhler, 2012; Ladino et al., 2011).

Early experiments of contact freezing, from which much of the observational evidence of this mode's higher ice nucleating efficiency has risen, were conducted in a wind tunnel or using a cold plate in which rain sized drops were collided with particles hundreds of micron in size (Gokhale and Goold, 1968; Pitter and Pruppacher, 1973). Therefore, neither the sizes of the droplets themselves nor the particles were atmospherically relevant (DeMott et al., 2010). There is also some theoretical basis for contact freezing's potentially higher ice nucleating efficiency. A classical thermodynamic treatment does show that at the particle/droplet/air interfacial line the surface energy barrier to ice nucleation is lower than the particle/droplet surface interface inside

the droplet bulk, where immersion freezing would occur (Djikaev, and Ruckenstein, 2008). With one dimensional and more complex cloud models agreeing that significant alteration to cloud phase state and lifetime can result from small differences in the ice nucleating capabilities of the particle population (Ervens and Feingold, 2012; Gettelman et al., 2012; Vali and Snider, 2015), improved contact freezing measurements should arguably remain to be a high priority research endeavor for the atmospheric ice nucleation community.

While progress towards more reliable contact freezing measurements has been slow over the past two decades, there has been important progress in the last few years in reducing its deficient state of knowledge. The implementation of the electrodynamic balance (EDB) to study contact freezing (Hoffmann et al., 2013a, 2013b) has been particularly promising. Atmospherically relevant particle sizes were allowed to collide with an individually levitated water droplet. Through a robust analysis of the flow regimes inside the EDB, numerical estimates of the collision frequency were made and this led to quantifying the contact freezing abilities of size selected Arizona Test Dust and kaolinite mineral particles. The same system could also probe the immersion freezing abilities of the same types of particles which allowed direct comparison of the two ice nucleation modes. Consistent with traditional observations and theory, the contact freezing mode was found to be more efficient compared to immersion-mode freezing in the studies conducted. Ladino et al. (2011) reported a unique new method to study contact freezing termed the Collision Ice Nucleation Chamber (CLINCH). 26 μm diameter drops were collided with size-selected 400 or 800 nm kaolinite particles in a laminar flow, and hence the method provided the advantage of studying atmospherically relevant particle and droplet sizes. However, many assumptions had to go into relating the collision frequency to the contact freezing efficiency which are measured separately. The collision frequency is measured using the collected droplets at the

bottom of the flow tube which are actually the droplets that did not freeze. Freezing efficiencies higher than 1 did result because of the discrepancy. The CLINCH was also used in a recent study by Nagare et al. (2016) in which it was combined with the Immersion Mode Cooling Chamber–Zurich Ice Nucleation Chamber (IMCA–ZINC) to allow comparison with immersion mode freezing. The results did not confirm a general trend of higher efficiency in the contact versus immersion mode. This is an interesting finding as it does go counter to much of the existing evidence including the recent EDB approach. Another result that went counter to the hypothesis of contact freezing being more efficient was reported in Gurganus et al. (2013), albeit through indirect evidence. Novel high speed imaging was employed to examine if there is a preference of homogenous nucleation to happen on the contact line over the bulk. No preference was found, which did not support the hypothesis that there is a thermodynamic preference to crystal nucleation at the surface where the energy barrier is reduced. The big caveat of the study however is droplet size, which was 250 μm. It remains a plausible hypothesis that at smaller cloud relevant sizes of 10s of microns, a reduction to the energy barrier can still exist. Durant and Shaw (2005)conducted a cold plate study in which a droplet (3-4 mm diameter) containing a glass rich volcanic ash particle (hundreds of microns in diameter) was allowed to evaporate allowing the particle to come in contact with its surface. Freezing upon contact of the particle with the droplet surface occurred at higher temperatures compared to when freezing was induced within the bulk. This was termed freezing "inside out" and gave further evidence to the hypothesis that the energy barrier to ice nucleation at the surface is reduced compared to the droplet bulk. Another recent study pointing to an advantage of contact freezing over immersion freezing was conducted by Nieahuas and Cantrell (2016) whereby salt particles (NaCl and KCl among others, tens of microns in diameter) induced freezing upon collision with a droplet (hundreds of microns in diameter) placed on a cold

plate. This was a case in which salt particles are unable to induce freezing in the immersion mode as they would readily dissolve in the water. It was estimated that freezing must have occurred within a few nanoseconds of the collision (details of the method are reported in the cited publication).

The aerosol optical tweezers has been a powerful tool in studying the properties and behavior of individual particles in real time (Hopkins et al., 2004; Mitchem and Reid, 2008). With its ability to trap droplets indefinitely with a laser beam while acquiring their cavity enhanced Raman spectrum, measurements of unprecedented accuracy of properties such as droplet size, refractive index, rates of growth/evaporation, diffusivity, viscosity, water activity, and the morphologies of mixed particles have been achieved (Cai et al., 2015; Hargreaves et al., 2010; Power and Reid, 2014; Lienhard et al. 2014; Gorkowski et al. 2016). At discrete wavelengths, a spherical droplet can behave as an optical cavity, leading to standing electromagnetic waves on the droplet surface where the Raman scattered photon signal is amplified (Hopkins et al., 2004). This cavity enhanced Raman spectrum is commensurate with Whispering Gallery Modes (WGMs) (Chang, 1988). The unique WGM fingerprint of a droplet's size and chemical composition allows independent retrieval of the radius and refractive index to a very high accuracy (Miles et al., 2012; Preston and Reid, 2013, 2015).

Similar to the recent EDB approach, the optical tweezers provides an excellent opportunity to study contact freezing with the stably trapped droplet acting as a cloud droplet proxy while exposing it to a stream of particles, and observing droplet freezing events. There are however two key limitations to the EDB method that the optical tweezers can overcome. The first is the droplet size: droplets trapped in the optical tweezers are on the order of a few microns which is closer to cloud droplet sizes than the EDB's levitated hundred micron sized droplets. With theoretical

evidence indicating droplet curvature can play a role in reducing the energy barrier at the contact line, droplet size may be a critical parameter in contact freezing and this needs to be experimentally tested. The second advantage is the *in situ* detection of particle collisions whereby the surface sensitive cavity enhanced Raman spectra retrieved by the optical tweezers may prove to be a collision detector since any particle that penetrates the droplet's surface would disturb the WGMs that form in the droplet's surface layer. This would allow direct measure of the collision frequency and consequently the contact freezing efficiency.

Ishizaka et al. (2011) successfully used optical tweezers to probe aqueous ammonium sulfate droplets down to homogenous freezing temperatures. While the relative humidity in their system was too low for achieving water vapor pressure conditions relevant to mixed phase clouds (near liquid water saturation pressure (Morrison et al., 2011; Pruppacher and Klett, 1997)) the study did provide a proof of concept that trapping droplets at freezing temperatures is possible.

In an attempt to aid in overcoming traditional challenges in observing heterogeneous ice nucleation in general and contact freezing in particular, a novel refrigerated optical tweezers has been designed and implemented. While still in the development stage, the system has demonstrated its unique ability to trap aqueous water droplets below 0 °C and retrieve their properties. This extends the unique capabilities of the traditional aerosol optical tweezers into the sub-zero temperature range. Preliminary results also demonstrate that the newly developed system may be able to observe *in situ* individual particle-droplet collisions in real time. Details of the design and performance of this new subzero temperature controlled Chilled Optical Aerosol Tweezers (COAT) system are described in this chapter. Two generations of cooling experiments (early and recent), whereby aqueous water droplets are trapped and cooled down to subzero temperatures, are

presented and analyzed with a refractive index inter-comparison method. The method compares the measured refractive index from the WGMs to the expected refractive index from the change in droplet volume and thus solute concentration. The droplet volume is determined from the droplet's radius measurement obtained from fitting the WGMs. A consistent trend of diverging measured and expected refractive indices with cooling and consequent droplet evaporation is shown and discussed. Constraints on the relative humidity with respect to ice achieved in the systems at subzero are placed to assess the system's ability to achieve ice supersaturated and near supercooled liquid water saturation conditions.

4.2 Instrument design

The COAT is an extension of the aerosol optical tweezers described in Gorkowski et al. (2016) and Mitchem and Reid (2008). The operating principles are reviewed here and a schematic of the system built at Carnegie Mellon University is shown in Fig. 4.1. The most notable change from the traditional aerosol optical tweezers is the use of an ultra-long working distance microscope objective instead of an oil immersion microscope objective found in setups described in Gorkowski et al. (2016), Hopkins et al. (2004b), and Mitchem and Reid (2008) to focus the trapping laser beam. This is done to avoid contact of the objective with the cold chamber's exterior, as this temperature change can damage or distort the objective's optics. A 532 nm diode pumped solid state laser (Coherent Verdi G) with a 2.5 mm beam width is set to a power of around 150 mW, steered by mirrors, and expanded (using 60 mm and 100 mm plano-convex lenses) to slightly overfill the 3.8 mm diameter aperture of the ultra-long working distance objective (100X Mitutoyo Plan Apo Infinity Corrected Long WD Objective, 13 mm working distance, Edmund Optics). The objective tightly focuses the beam and creates a stable optical trap just above the focal point induced by a strongly restoring three-dimensional optical gradient force (Reid and Mitchem,

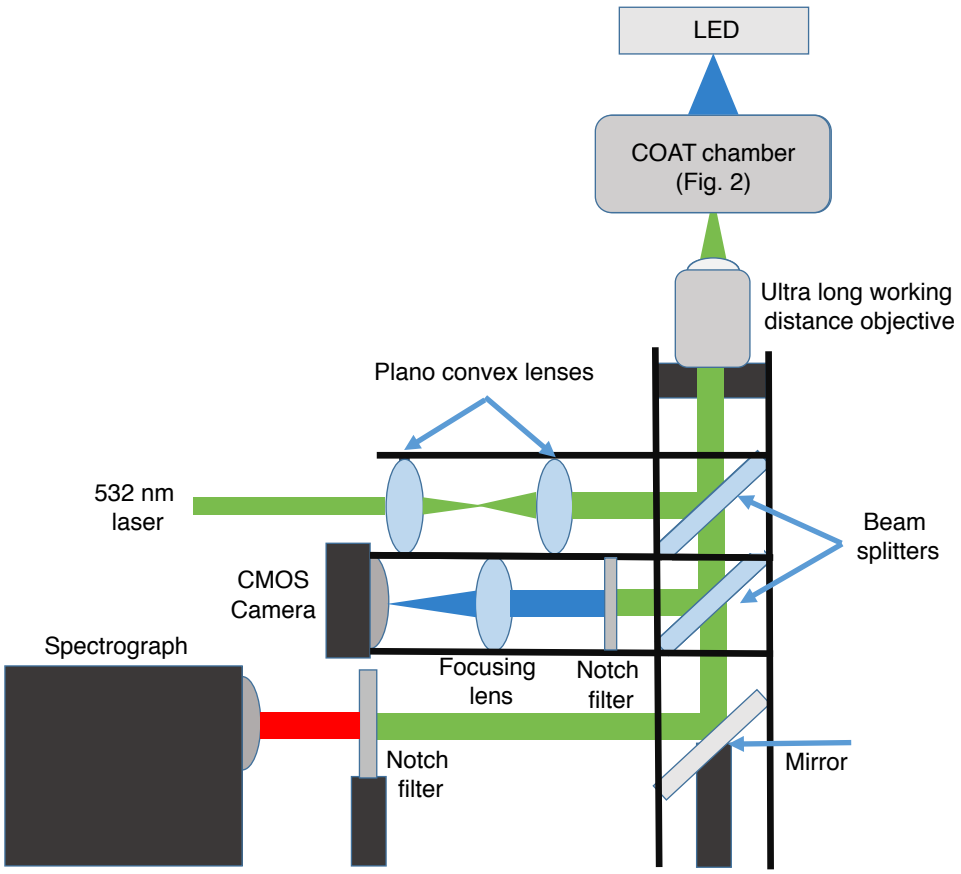

Figure 4.1. A schematic of the optical setup for the Chilled Optical Aerosol Tweezers (COAT) system. The instrument is optically a similar design to a traditional aerosol optical tweezers apart from the ultra-long working distance objective used in place of an oil immersion objective. The color of the beam corresponds to the wavelengths of light being transmitted.

2006). Using the ultra-long working distance objective, the droplet is trapped a few hundred microns above the surface of the glass cover slip as the beam passes through at the chamber's bottom (Fig. 4.1). The resultant optical trap is capable of trapping supermicron droplets indefinitely, without user intervention such as having to adjust the trapping laser beam's power. Aqueous droplets have a negligible absorption cross section at 532 nm and are heated by the laser beam by just a few mK in temperature (Hopkins et al., 2004).

A visual image of the droplet is also acquired in real-time. This is important for observing the droplet capture process when loading the optical trap, and for observing the droplet's stability in the trap. A royal blue LED (Rebel LED 447.5 nm, Luxeon) is mounted over the trapping chamber to illuminate the droplet for visual imaging. The same microscope objective magnifies the droplet image which is then captured by a CMOS camera (USB 2.0 CMOS camera, Thorlabs). A 532 nm notch filter (Semrock, bright line single-band bandpass filter) is placed before the CMOS camera and spectrograph to remove the intense green 532 nm trapping laser radiation. This is followed by a focusing lens (50 mm convex lens) to help sharpen the droplet image acquired by the CMOS camera.

Laser radiation ineleastically scattered from the trapped droplet is focused by the microscope objective to retrieve the droplet's Raman spectrum. The Raman signal is collected by a CCD coupled spectrograph (SP2500, Princeton Instruments) using a 1200 groves/mm grating blazed at 500 nm. Another 532 nm notch filter is placed at the entrance of the spectrograph to remove reflected radiation from the bright trapping laser beam. Raman spectra are collected with a one second acquisition time for the experiments discussed in this chapter.

Figure 4.2a details the design features of the temperature-controlled droplet trapping chamber used in the custom COAT system. A cylindrical aluminum chamber is used for the temperature controlled trapping chamber. Liquid coolant (Polycool HC-50) is cooled down to a set temperature with a recirculating chiller (Polyscience), and the coolant flows through the outer chamber wall and cools the surface of the inner aluminum walls. Dry and purified nitrogen gas flows through a helix between the coolant jacket and inner walls to cool down to the inner wall's temperature before mixing with a flow of humidified room temperature nitrogen gas to create a gas stream with a select ratio of dry to saturated flow that enters the inner trapping chamber above the tweezed

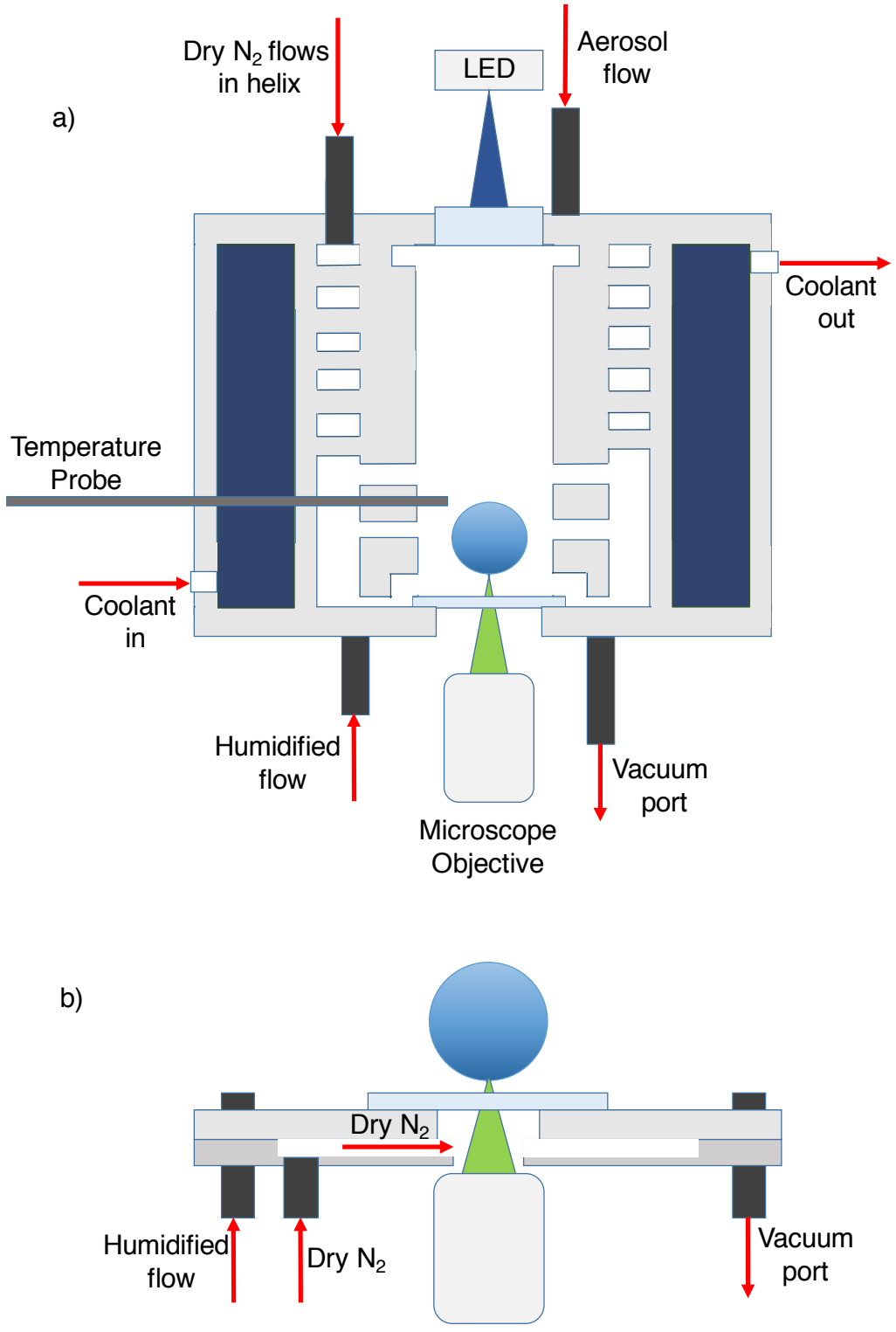

Figure 4.2. a) A cross section of the temperature-controlled droplet trapping chamber in the COAT system, showing air and refrigerant flow paths and droplet measurement design features. **b)** Design

features of the droplet trapping chamber window region. The schematic shows the principle design of the insert below the chamber that ensures a minimal temperature gradient across the glass coverslip and no condensation or frost deposition on the outer side of the window. Dry air or nitrogen gas that has equilibrated to the outer wall temperature is flowed over the outside of the glass coverslip to prevent fogging and frost formation. More stable temperatures (reduced temperatures fluctuations) are also attributable to the insert at subzero conditions.

droplet's position. The excess flow port is connected to a vacuum line to pull the nebulized aerosol introduced at the top of the chamber through the trapping position. Figure 4.2b shows the principle design of the insert below the chamber that ensures a minimal temperature gradient across the glass coverslip and no condensation or frost deposition on the outer side of the window exposed to ambient conditions. More stable temperatures (reduced temperatures fluctuations) are also attributable to the insert at subzero conditions, evidence of which is presented in contrasting older and recent experiments later in this chapter.

To prevent frost deposition on the coverslip, which would distort the symmetrical trapping laser and thus interfere with the trap beam, and also distort the droplet's retrieved Raman spectrum, the glass coverslip is first soaked overnight in a 50:50 Decon 90:water surfactant solution. This is followed by another overnight soaking in propylene glycol to create an antifreeze coating on the glass. The coating ensures the cover slip's surface remains homogenous to not interfere with the trapping and imaging processes. The surfactant promotes the spreading of droplets that land on the coverslip during the aerosol loading phase, while the antifreeze prevents frost deposition when working at subzero temperatures.

Frost deposition on the outside part of the glass coverslip exposed to ambient conditions is

prevented via a different mechanism. The insert has a dry nitrogen flow port and is given a 2 mm clearance from the coverslip (Fig. 4.2b). The gas enters the insert and cools down to the outer wall temperature via conduction before flowing just below the glass coverslip. In addition to keeping the bottom of the window dry the flow minimizes the temperature gradient the thin coverslip window otherwise would be vulnerable to as it exposed to the ambient temperature. This is important as the droplet is trapped less than one mm above the coverslip, and we want to isolate it from heat transfer from outside the chamber.

The recirculating chiller is set at a temperature a few degrees lower than the target temperature inside the chamber due to heat gain from the lines and outer chamber wall. An RTD temperature sensor (OMEGA Pt100 RTD sensor) is inserted into the chamber 10 mm above the coverslip and close to the trapped droplet's position. Due to the proximity (around 200 μm) of the droplet to the coverslip it was important to verify that temperature variation from the RTD's point of measurement all the way down to the glass coverslip was minimal. To do so an Omega surface thermocouple (OMEGA K type) was attached to the surface of the glass coverslip while the system was cooled down from room temperature to -30 °C. Figure 4.3 plots the temperature measured at three distinct points: the chiller temperature, the RTD temperature above the droplet, and the glass coverslip temperature below the droplet as the system was cooled at a steady rate of 0.3 °C/min. The temperatures measured by the RTD and the thermocouple are almost within the measurement uncertainty range of each measuring device (±1 °C). For the purposes of the experiments presented in this chapter, the temperature referred to is the temperature recorded by the RTD sensor above the trapped droplet.

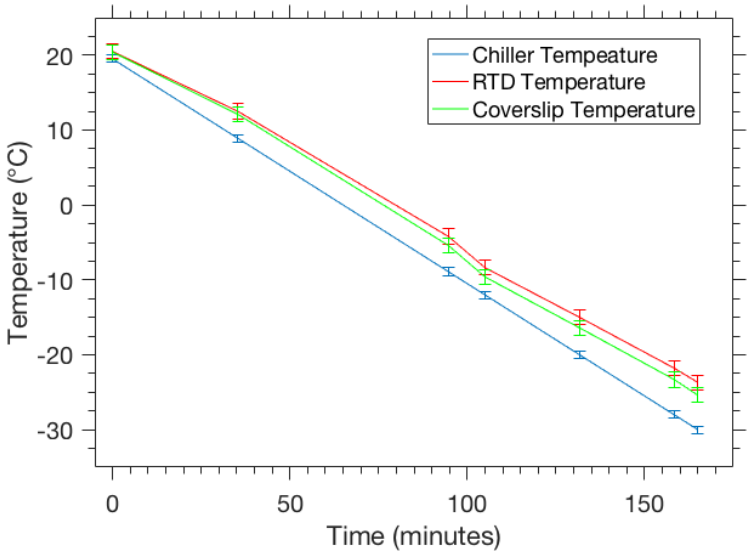

Figure 4.3. Three independent measured temperature profiles of the COAT system as it was cooled at 0.3 °C/min: temperature of the chiller's recirculating fluid, RTD temperature measured 1 cm above the droplet trapping region, and the temperature of the glass coverslip.

To trap a droplet, the vacuum flow is set at 0.3 SLPM while the conditioned air flow is temporarily turned off. A medical nebulizer (Omron NE U22) generates an aerosol flow from an aqueous KCl solution, typically around 0.1 M concentration, that is pulled into the chamber by the vacuum flow and is forced to pass through the trapping region due to the position of the vacuum flow port (Fig. 4.2). The vacuum flow is turned off after 3 to 5 seconds which helps reduce the velocity of the droplets in the trapping region to make it easier for the optical trap to become loaded. At this point the first droplet is trapped and multiple droplet collisions with the now trapped droplet typically follow. Trapping is confirmed using the visual imaging described above. The laser power is then adjusted to accommodate the growing trapped droplet. Within 10 to 20 seconds the collisions stop and the droplet sits stably in the trap. Directly following the conditioned air flow is resumed and set at 0.3-0.4 SLPM and the vacuum flow is restored to 0.3 SLPM. This is a

recently optimized trapping protocol that was not used in the early experiments. Originally trapping was done by continually flowing aerosol into the chamber. It was later realized that this method was very inefficient as the droplets' speeds were too high around the trap region due to continuous pulling through the vacuum flow. The aerosol stream was too concentrated which probably led to droplets knocking each other out of the trap.

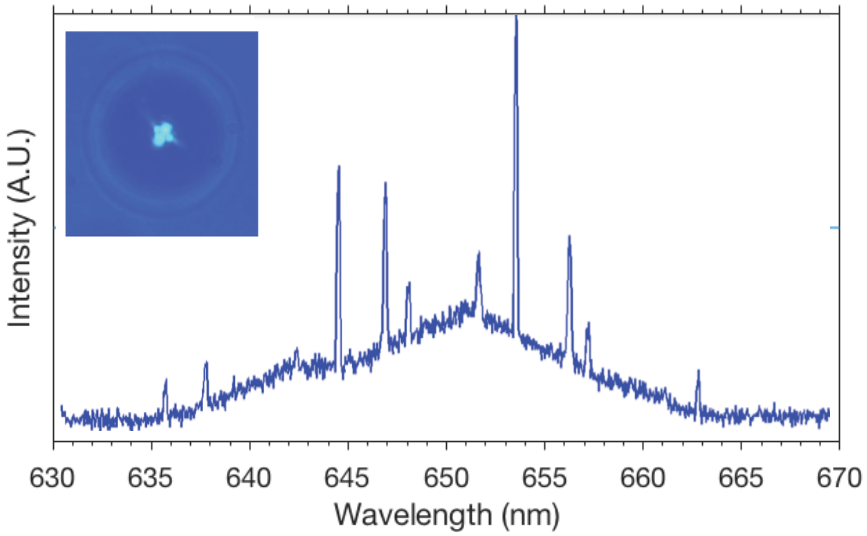

Figure 4.4. Example Raman spectrum of a tweezed aqueous KCl(aq) droplet with a radius of 5.562 μm and a refractive index of 1.382 retrieved from analysis of the WGMs. The sharp peaks superimposed on the broad H_2O stretch Raman mode are WGMs occurring at discrete wavelengths that resonate with the droplet's circumference. The inset is an example visual image of an optically tweezed droplet obtained by the COAT system.

Figure 4.4 shows an example of a retrieved Raman spectrum for a tweezed KCl aqueous water droplet. The sharp peaks are WGMs occurring at discrete wavelengths corresponding to the wavelengths of Raman scattered photons that resonate with the droplet's circumference. The electric and magnetic signals of a stimulated photon of light in the cavity enhanced Raman signal

do not coincide, which causes a single WGM to have a pair of stimulated modes at two adjacent wavelengths termed transverse electric (TE) and transverse magnetic (TM) modes (Reid and Mitchem, 2006). For a given size, droplet composition or refractive index is sensitive only to the TE mode and not the TM mode of a WGM (Miles et al., 2012). This paves the way for independent size and refractive index retrieval, as the unique combination of wavelength positions of the WGMs allows accurate size determination while the spacing between consecutive TE and TM modes allows refractive index determination (Preston and Reid, 2013, 2015). The example WGMs from a KCl(aq) droplet trapped in the COAT shown in Fig. 4.4 were fit to a droplet radius of 5.562 μm and a refractive index of 1.382.

4.3 Method for inter-comparison of measured refractive index with predicted refractive index

Unique WGM droplet positions and spacing provide independent retrieval of the droplet's refractive index and the droplet size. Since the refractive index can be reliably related to the salt concentration through a linear volume mixing rule (Liu and Daum, 2008; Miles et al., 2012), it is then possible, after determination of the droplet salt concentration before cooling starts, to use the droplet change in volume throughout the experiment to calculate an expected or predicted refractive index.

The following refractive index linear volume mixing rule, which is detailed in Liu and Daum (2008), relates the salt volume fraction to the refractive index of the droplet and the refractive indices of pure water and that of the solute (pure molten salt):

$$\frac{n_{droplet}-1}{n_{droplet}+2} = f_s\frac{n_s-1}{n_s+2} + f_w\frac{n_w-1}{n_w+2} = f_s\frac{n_s-1}{n_s+2} + (1-f_s)\frac{n_w-1}{n_w+2} \qquad (1)$$

where $n_{droplet}$ is the effective refractive index of the droplet, n_s is the refractive index of the solute, n_w is the refractive index of pure water, and f_w and f_s are the volume fractions of water and solute respectively. The refractive indices of the pure water and the salt, which is KCl for the experiments shown in this chapter, are 1.33 and 1.49 at a wavelength of 650 nm respectively (Hecht, 2001). 650 nm is the center of the water Raman stretch mode where the WGMs that are fit are located (Fig. 4.4).

The estimated salt volume fraction f_s is evaluated using the initial salt volume fraction $f_{s,i}$ and the retrieved droplet radius, r:

$$f_s = f_{s,i}\frac{r^3}{{r_i}^3}\frac{\rho_s}{\rho_{s,i}} \qquad (2)$$

where r_i is the droplet radius determined from the WGMs retrieved before cooling started, r is the droplet radius determined from the WGMs throughout the cooling and hold phases of the experiment, and $\rho_{s,i}$ and ρ_s are the densities of the dissolved KCl in the droplet during the initial phase of the experiment and throughout the cooling/hold phases respectively. $f_{s,i}$ is approximated from the determined initial refractive index of the droplet using the linear volume mixing rule stated above (Liu and Daum, 2008):

$$f_{s,i} = \frac{\frac{n_{droplet,i}-1}{n_{droplet,i}+2} - \frac{n_w-1}{n_w+2}}{\frac{n_s-1}{n_s+2} - \frac{n_w-1}{n_w+2}} \qquad (3)$$

With the information gathered about droplet size and refractive index, insights on the RH of the air surrounding the droplet can be gained which helps determine the extent to which supersaturation with respect to the ice phase can be achieved in the current system design. Ice

supersaturation in the chamber is a necessary condition for achieving the thermodynamically metastable state of supercooled liquid water; ice has a lower saturated vapor pressure than supercooled water at a given temperature (Pruppacher and Klett, 1997). The first step in determining the RH of the surrounding gas phase is converting the salt volume fraction into a salt mole fraction X_s via the following mixing rule expression (Liu and Daum, 2008):

$$X_s = \frac{\rho_s}{\rho_{droplet}} \frac{M_{droplet}}{M_s} f_s \qquad (4)$$

where M_s is the molar mass of the solute and $M_{droplet}$ and $\rho_{droplet}$ are the effective molar mass and density of the mixed droplet, respectively, and can be evaluated with:

$$\rho_{droplet} = f_s \rho_s + (1 - f_s)\rho_w \qquad (5)$$

and

$$M_{droplet} = X_s M_s + (1 - X_s)M_w \qquad (6)$$

where ρ_w and M_w are the density and molar mass of pure water, respectively.

Using the salt molar fraction X_s the RH of the gas-phase in equilibrium with the aqueous salt droplet can be evaluated using (Seinfeld and Pandis, 2006):

$$RH = \gamma_w(1 - X_s) * 100 \qquad (7)$$

where γ_w is the activity coefficient of water. In all measurements presented here the molar ratio of water (0.85-0.95) was high enough to neglect γ_w and it is assumed to be 1 (i.e. an ideal solution). The RH with respect to the liquid phase can be converted to a RH with respect to the ice phase using the most up to date parametrizations summarized in Murphy and Koop (2005). The precision

in the retrieved radius and refractive index data points is calculated using a moving standard deviation for every 20 frames. A 95% data precision interval is then defined as twice the value of this standard deviation.

4.4 Early experiments on subzero droplets

Early experiments were conducted to test the capabilities of the COAT. Two tests that successfully cooled a droplet down to -12 °C are presented here. During these test a 0.1 M KCl solution was continually nebulized and pulled with a 0.3 SLPM vacuum flow. The average time it took to stably trap a droplet was between 5 and 10 minutes. Once the droplet was trapped the fully saturated RH flow (measured to be 100% RH before entering the chamber using a hygrometer (Vaisala)) was reintroduced into the chamber at a flow rate of 0.4 SLPM. The chiller was then turned on and set at a cooling rate of 0.8 K/min for the first experiment and 0.5 K/min for the second experiment. Figure 4.5 show the retrieved Raman spectra, a time series plot of the droplet radius (r), and a time series plot of the refractive index (n) for experiments 1 and 2 respectively. Cooling started at t = 0 from a temperature of 20 °C.

In examining the Raman spectra in Fig. 4.5 for experiment 1 (left) the first noticeable feature is the initially steady WGMs, which can be distinguished by bright yellow lines due to their high intensity, down to a temperature of around 13 °C. After which the WGMs start to shift to lower wavelengths, which is indicative of droplet evaporation. Droplet shrinking is expected due to increases in thermal gradients throughout the conditioned flow lines and chamber walls which

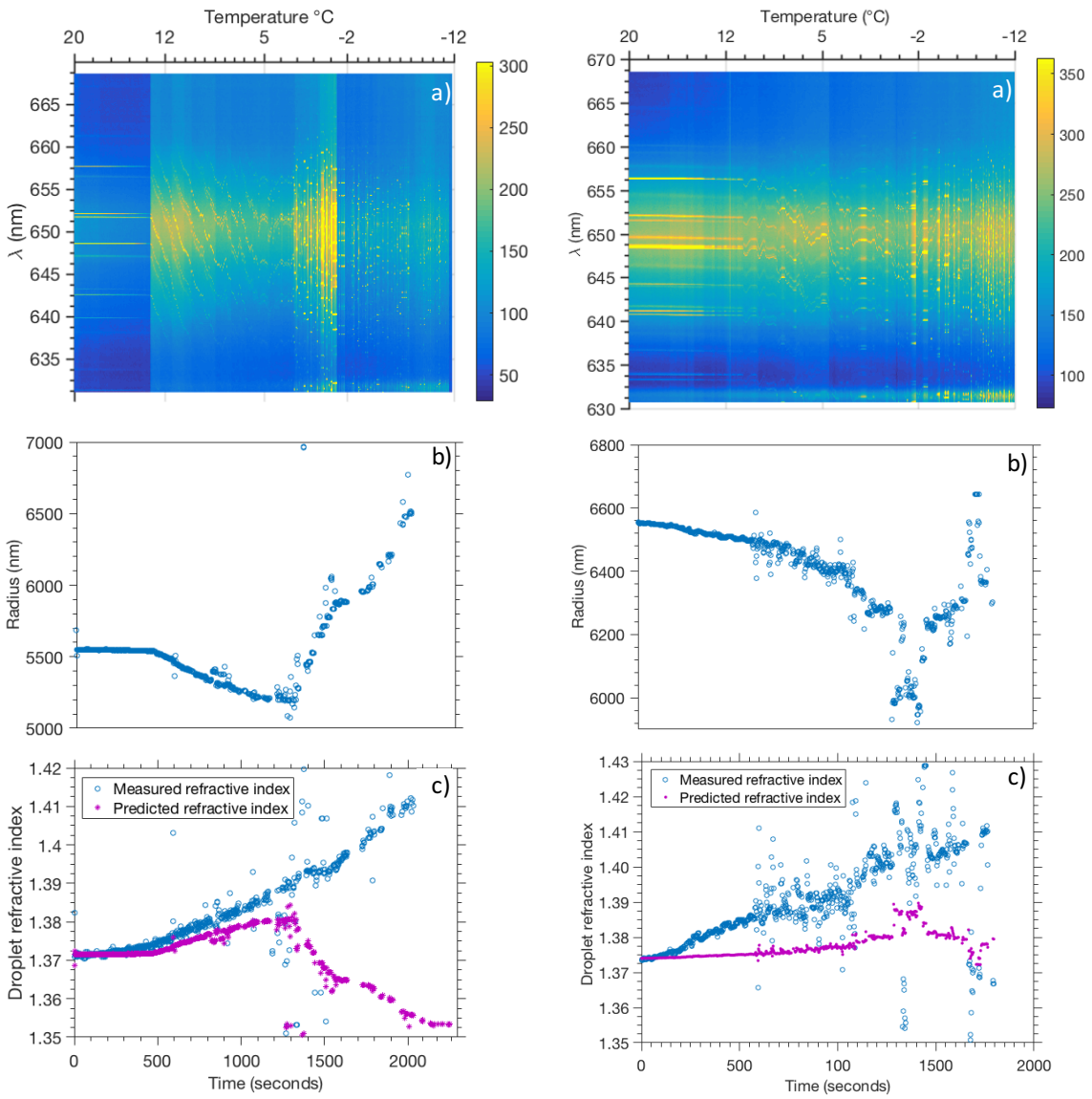

Figure 4.5. Left: Cooling experiment 1 on a KCl(aq) droplet with an initial radius of 0.5549 μm and refractive index of 1.372. **Right:** Cooling experiment 2 on a KCl(aq) droplet with an initial radius of 0.1520 μm and refractive index of 1.374. **a)** Contour time-series plot showing the retrieved droplet Raman spectra as a function of time throughout cooling experiment. The sharp bright lines represent the WGMs which occur at approximately discrete wavelengths corresponding sensitively to the droplet's size and refractive index. The shift of the WGMs to lower wavelengths indicates droplet evaporation while no change in their position indicates the

droplet is stable in size and composition. **b)** Estimated radius time series for the cooling KCl experiment. **c.** Estimated refractive index time series for the cooling KCl experiment (blue circles) plotted with a predicted refractive index using the radius estimates from Fig. 4.5b.

causes loss of water vapor in the conditioned air before reaching the droplet. It is unclear why the WGMs would experience such an abrupt transition. The radius time series in Fig. 4.5 for experiment 2 (right) is consistent with this interpretation of the WGMs, as at about the same time the abrupt transition of the WGMs takes place the rate of evaporation of the droplet suddenly increased (indicated by the change in slope in the radius time series plot). The increase in the measured refractive index n shown in Fig. 4.5 is also consistent with droplet evaporation, as the n of KCl is larger than the n of H_2O and the molar ratio of the salt becomes larger with loss of water. The WGMs retrieved experience a clear deterioration in quality at around 1400 seconds or 3 °C. At that point the original WGMs are no longer apparent so a trend (size decrease or increase) can no longer be directly observed from the spectra. The size fits become sparse (only 1 in 10 fits successfully returning a radius fit) and the trend of size increase goes counter to the continued loss of water vapor reaching the droplet with decreasing temperature. Furthermore, the refractive index estimates from the fits to the WGMs do not experience any shift in trend as they continue to increase past the WGM deterioration point.

The inter-comparison method presented previously is used to retrieve the predicted refractive index which is plotted alongside the measured refractive index in Fig. 4.5. Before the deterioration point the trends in the measured and predicted n are quite similar though there is a clear divergence in the values with decreasing temperature. This is a consistent result with all of the experiments presented here and will be discussed in further detail at a later point in the chapter. After the

deterioration point the trends in the measured and predicted *n* diverge. This is due to the inconsistent increase in size the droplet radius measurements exhibit which leads to a decrease in the predicted *n*.

The Raman spectra of experiment 2, plotted on Fig. 4.5 (right), exhibit some similar features to those of experiment 1. The WGMs are quite steady in the initial phase of cooling before an abrupt transition to less steady behavior at around 10 °C. A WGM deterioration point can also be seen at around 0 °C after which the original WGMs are no longer apparent. The WGMs during cooling do look steadier than in experiment 1, which may be explained by the smaller cooling rate which leads to a lower evaporation rate. The radius time series in Fig. 4.5 (right) shows a steady evaporation trend even during the seemingly steady initial phase of the experiment. The refractive index time series shown in Fig 4.5 (right) does show an increasing trend. However, as indicated by the predicted *n* plotted alongside the measured *n*, the difference in the rate of change is more substantial in experiment 2 than in experiment 1. After the WGM deterioration point, similar to experiment 1, the radius fits do suffer more than the refractive index fits with a significant reduction in the frequency of successful radius fits per frame (only around 1 in 10 frames were fitted to a radius). There is a data gap in the radius fits right after the deterioration point followed by a slightly increasing trend in droplet radius. The retrieved refractive index continues to increase, which is inconsistent with the radius fits and similar to the results from experiment 1.

Some insights into the relative humidity (RH) achieved in the system can also be made for the two experiments using the method presented in Section 4.3. For experiment 1 the RH with respect to liquid water at the start of cooling is calculated to be 89.5% (∓0.5%), 85% (∓1%) at 3 °C (before WGM deterioration point) using the measured *n*, and 87% (∓1%) at 3 °C using the

predicted *n*. For experiment 2 the RH at the start of cooling is calculated to be 88% (∓0.5%), 83% (∓1%) at -2 °C using the measured *n* (before WGM deterioration point), and 87% (∓1%) at -2 °C using the predicted *n*. From the perspective of supercooled water these RH estimates indicate the system is too dry, an RH of 87% at -2 °C corresponds to an RH of 88% with respect to the ice phase which is well below ice saturation conditions. So even pure ice would evaporate. Further droplet experiments were generally unstable; a limited amount of probing time was practically available before droplets fell out of the trap (around 1 hour for a cooling experiment). Tests in which a droplet was allowed to equilibrate to one respective temperature, i.e. temperature hold tests, were not possible because of this unstable trapping. In the next section a more recent experiment is shown in which these hurdles of dryness and trap instability were partially overcome. Overcoming droplet instability is attributable to the addition of the insert described in Fig. 4.2b earlier. The explanation for improved stability is that smaller exposed area of the glass to the outside ambient conditions and the more laminar flow of air flowing beneath it led to reduced turbulence in and around the coverslip. This explanation was never directly tested by comparing trapping stability with and without the insert, but the system has exhibited more stable droplet traps since the addition of the insert. Further the new trapping protocol which allows for a droplet to be trapped within a minute using only a pulse of aerosol means reduced deposition of concentrated KCl solution droplets on the coverslip. This excess salt deposition is probably what forced a lower equilibrium water vapor pressure on the droplet despite the efforts of maintaining high moisture levels with the conditioned air; the salt on the cover slip close to the tweezed droplet would absorb water vapor.

4.5 Recent COAT system testing and validation using a single KCl aqueous droplet

In this section a recent experiment, which incorporated the new insert and new trapping protocol, is presented. A 0.1 M solution of KCl was nebulized and trapped with the new trapping protocol. After which the recirculating chiller was turned on at and set to a temperature of 20 °C before trapping to avoid perturbation of the trap due to sudden vibrations induced by the chiller compressor through the fluid lines. After loading the trap, the droplet was allowed to equilibrate to the surrounding environmental temperature and RH conditions. Equilibration is indicated when the retrieved WGMs stabilize, indicating no further change in droplet size and composition (Reid and Mitchem, 2006; Symes et al., 2004). Droplet Raman spectra were continually retrieved with a 1 second acquisition time. The experiment consisted of two cooling phases (from 20 °C to 0 °C at a cooling rate of 0.3 °C/min and later from 0 °C to -12 °C at a cooling rate of 0.18 °C/min) and two temperature hold phases (at 0 °C and -12 °C). Figure 4.6a is a contour plot showing the retrieved droplet spectra throughout the cooling and hold phases of the experiment. The sharp bright lines represent the WGMs which occur at approximately discrete wavelengths. During the cooling phases of the experiment the WGMs were shifting to shorter wavelengths indicating a decrease in the size of the droplet (Reid & Mitchem, 2006). Droplet shrinking is expected due to increases in thermal gradients throughout the conditioned flow lines and chamber walls which causes loss of water vapor in the conditioned air before reaching the droplet. The extent to which this water vapor loss occurs will be evaluated in the upcoming analysis. During the hold phases of the experiments the system was able to successfully allow the droplet to equilibrate as can be seen with the steady wavelength positions of the WGMs between 4000-6000 seconds and 10500-12000 seconds in Fig. 4.6a.

The WGM fitting method described in Preston and Reid (2013) and Gorkowski at al. (2016) is used to independently retrieve the droplet radius and refractive index (n). As mentioned previously independent retrieval of the refractive index is based on resolving the transverse electric and transverse magnetic modes comprising each WGM. Therefore, the fitted refractive index is generally more sensitive to the resolution of the WGMs typically leading to a larger scatter (thus larger precision intervals) in the fits per frame compared to the radius. The WGMs of the Raman spectra retrieved after equilibration at room temperature before the cooling started are used to determine the initial droplet radius and refractive index.

Figures 4.6b and 4.6c show the determined droplet radius and refractive index throughout the cooling and hold phases of the experiment. The radius time series shows that the droplet is shrinking with cooling which is consistent with the WGMs shifting to lower wavelengths and the reduction in the RH around the droplet due to water vapor loss as discussed above. The precision interval in the determined radius is largest in the beginning of the first cooling phase and the second cooling phase (80 nm). The larger scatter during the cooling phases is due to the decrease in measured WGM resolution as the droplet is shrinking over the 1 second acquisition time of the droplet's Raman spectrum. The WGMs could not be resolved towards the end of the second cooling phase (9200-10000 seconds, -8 to -12 °C) as can be seen in Fig. 4.6a. Therefore, radius and refractive index could not be determined for that period.

The droplet's refractive index increases with decreasing temperature which is consistent with the droplet's loss of water due to evaporation. As water evaporates, the KCl concentration increases which increases the refractive index of the aqueous droplet mixture due to the higher refractive index of KCl compared to water as stated previously. The precision of the retrieved refractive index is relatively larger than that of the radius due to its higher sensitivity to WGM

resolution as discussed earlier, with values of $2\sigma = 0.01$ in the first cooling phase, 0.0035 for the first hold phase, 0.02 for the second cooling phase, and 0.005 for the second hold phase. Furthermore, a predicted RI is calculated and plotted in Fig. 4.6c (purple line) to compare with the measured RI. The purple line is generated using equations (1), (2), and (3) and assumes that the salt density in the mixture is constant with temperature.

In comparing the refractive index retrieved from the WGMs (referred to from here on as the measured refractive index) to the one predicted from the radius it can be seen that during the cooling phases of the experiment the measured and predicted *n* diverge, with the measured refractive index being noticeably higher than the predicted value. This is particularly evident in the last 1000 seconds of the first cooling phase (10 °C to 0 °C) and the entire second cooling phase (0 °C to -12 °C). In the first hold phase the predicted *n* is on average lower than the measured *n* but falls well within the interval of confidence of the latter and is strikingly close in the middle 500 seconds (4500-5500 seconds, at a temperature of 0 °C). In the second cooling phase, despite the measured *n's* large degree of scatter, the predicted *n* is significantly smaller. The return of the predicted *n* to falling within the scatter range of the measured *n* during the second hold phase supports a hypothesis that during cooling there is some transient effect of droplet evaporation on the salt concentration at the surface. As the WGMs occur in the surface layer of the droplet (radial penetration depth of the WGMs is approximately 30% of the droplet radius (Gorkowski et al., 2016; Van De Hulst, 1981)), the consequent estimated refractive index is therefore a droplet surface measurement. The potential gradient in salt concentration between the surface and the bulk during evaporation/cooling is a topic of ongoing research. It should be noted this transient change in refractive index has been a consistent observation in all of the droplet cooling experiments conducted in the COAT. If there is indeed a salt gradient in the radial profile of the droplet the

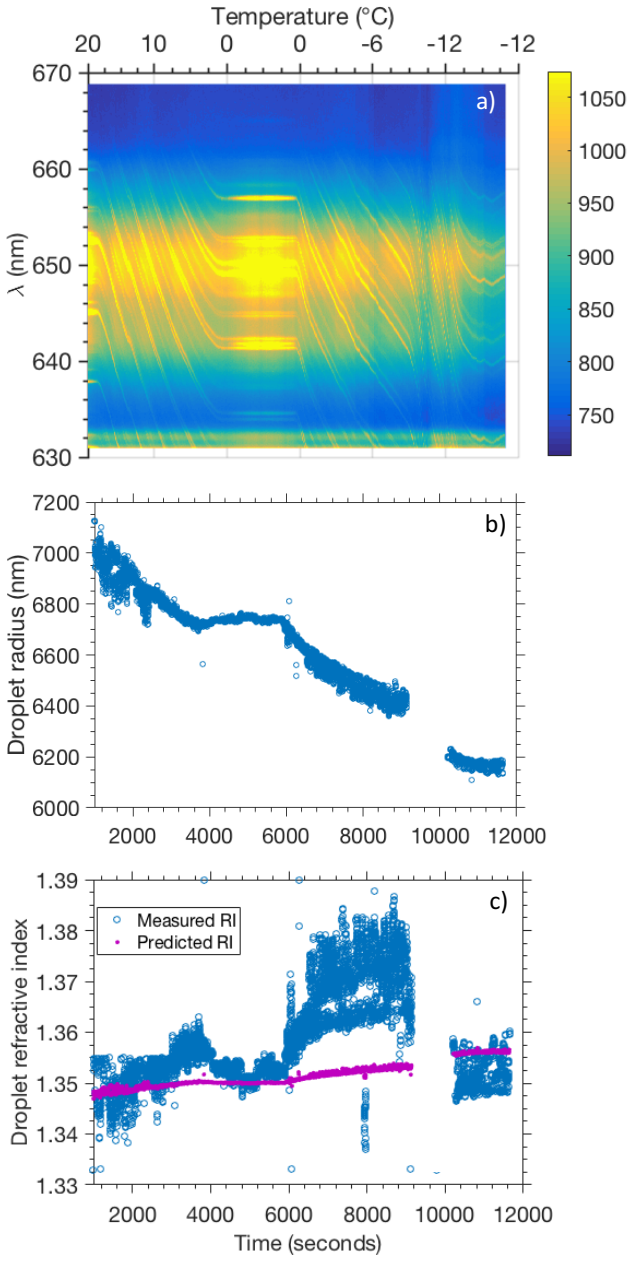

Figure 4.6. a) Contour time-series plot showing the retrieved droplet Raman spectra as a function of time throughout the cooling and temperature hold phases of the experiment on a KCl(aq) droplet with an initial radius of 0.701 μm and refractive index of 1.345. The sharp bright lines represent WGMs which occur at approximately discrete wavelengths corresponding sensitively to the droplet's size and refractive index. The shift of the WGMs to lower wavelengths indicates droplet

evaporation while no change in their position indicates the droplet is stable in size and composition**.** **b)** Estimated radius time series for the cooling KCl experiment. The decreasing radius through cooling is consistent with the WGMs' shift to lower wavelengths. **c)** Estimated refractive index time series for the cooling KCl experiment (blue circles) plotted with a predicted refractive index using the radius estimates in b).

phenomenon would be similar to observations of bromide surface segregation in bromide doped NaCl droplets (Ghosal et al., 2000; Hess et al., 2007), which has been shown to have important implications on Arctic atmospheric chemistry due to the significantly faster reaction rates of Br^- with atmospheric oxidants, compared to Cl^- (Antonsson et al., 2015).

The resultant RH estimates using the measured refractive index are: 94.5% (∓1%) before cooling starts, 93.5% (∓1%) for the first hold phase, and 93.5% (∓1.5%) for the second hold phase. Despite the larger scatter of the estimated RH in the second hold phase, it seems unlikely that with the significant evaporation between the first and second phases that the RH will remain unchanged. One potential culprit for this is the constant salt density with temperature assumption made in Eq. (2). If it is assumed that the discrepancy between the measured *n* and the estimated *n* in the second hold phase is due to an increase in the density of the dissolved salt with temperature, this higher density can be used in an alternative RH estimate. This higher salt density is estimated from the ratio of the salt volume fraction estimated from the refractive index and the salt volume fraction estimated from the radius:

$$\rho_{s,c} = \rho_s \frac{f_{s,p}}{f_{s,m}} \qquad (8)$$

where $f_{s,m}$ is the salt volume fraction retrieved from the measured refractive index, $f_{s,p}$ is the salt volume fraction estimated from the change of droplet size assuming constant salt density, and $\rho_{s,c}$ is the density of salt at the low hold temperature of -12 °C. If $\rho_{s,c}$ is alternatively used in Eq. (4) to find the salt mole fraction (which provides the RH estimate via Eq. (7)) the RH would be 92%, compared to 93.5% using the other method. This estimate is more consistent with the loss of water from the first hold phase to the second hold phase. This RH correspond to a RH_{ice} of 103.5% which means the current design is capable of creating ice supersaturated conditions and is therefore probing supercooled water.

4.6 Collision tests

Collision tests were conducted in order to test the WGMs' sensitivity to dust particles penetrating the surface of a trapped droplet, as this should momentarily quench the WGMs resonating in the surface layer. Figure 4.7 shows the custom built dust generation system used to deliver dust particles to the COAT chamber. A 250 ml Erlenmeyer flask with a custom built 3/8" glass inlet on its side is partially filled (5 cm from the bottom up) with Arizona Test Dust (Powder Technology Inc.). A nozzle made from a plastic pipette tip (2 mm inner diameter) is placed at the entrance of the custom built side port. Laboratory compressed air enters the flask through the nozzle and lofts the dust to create an aerosol. The Erlenmeyer flask is placed in a vibrating ultrasonic water bath to alleviate in preventing dust build up on the inner walls of the flask. The dust particle rich air flow enters a 5 L aluminum dilution tank where it is diluted with clean air. The COAT chamber's set vacuum flow pulls a desired amount of aerosol flow. Part of the aerosol flow (1 SLPM) is also pulled into an Optical Particle Sizer (OPS, TSI 3330) to get an estimate of the concentration of particles in the air flow going into the COAT chamber as well as its particle

size distribution. The flow going into the OPS and to the COAT is made to pass through a 1 μm inertial impactor (TSI 103590) to remove very large particles that can knock the droplet from the trap. Optimal flow conditions that resulted in potential particle collisions occurring with the trapped droplet were: 2 SLPM through the dust containing Erlenmeyer flask, 2 SLPM through the dilution tanks, and 0.3 SLPM pulled through the COAT chamber. The size distribution retrieved by the OPS is plotted in Fig. 4.8 and confirms removal of most particles larger than 1 μm in size.

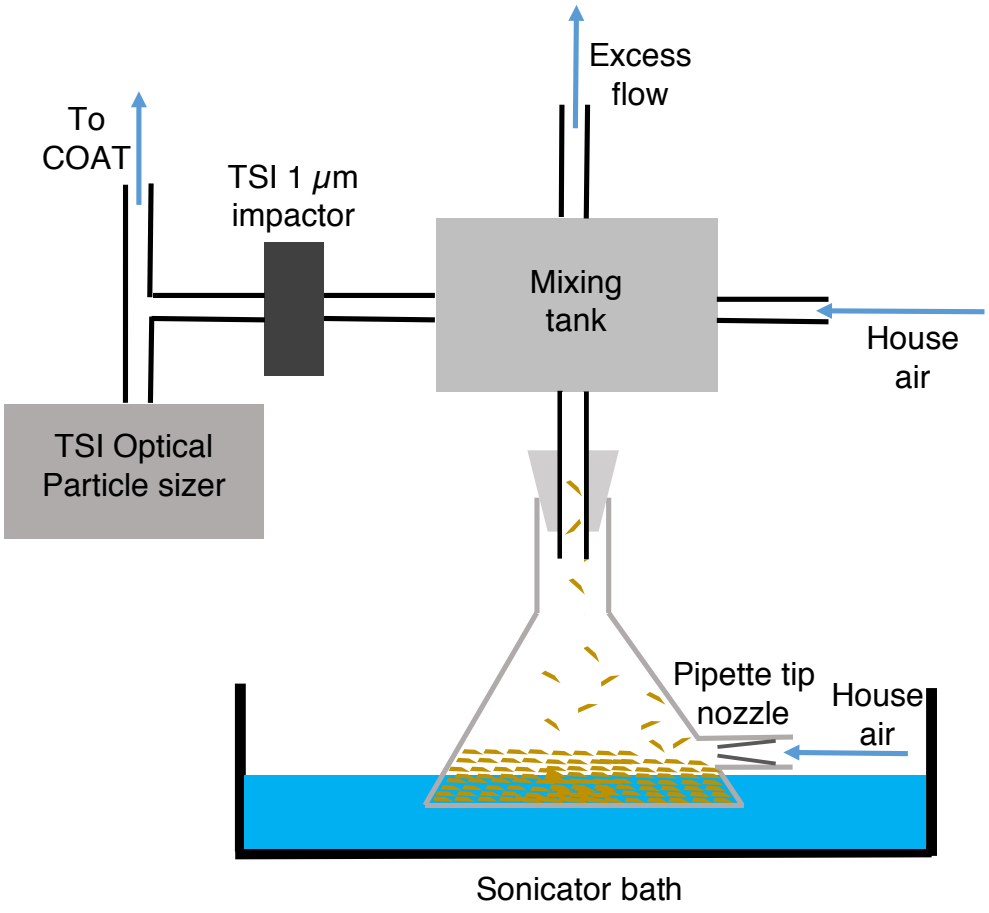

Figure 4.7. A schematic of the custom built dust generation system used for the collision tests. House air is accelerated via a nozzle to aerosolize ATD sitting in an Erlenmeyer flask. The aerosol is diluted in a 5 L mixing tank before being pulled into the COAT chamber.

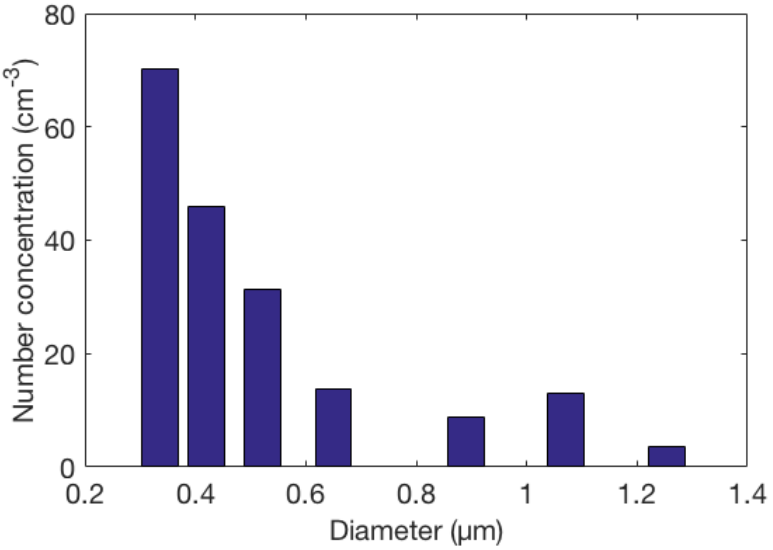

Figure 4.8. ATD size distribution retrieved from the optical particle sizer. The information was used to confirm removal of ATD particles larger than 1 μm in size.

In the experiment discussed here, evidence for collisions was found in both the interruption of the WGMs as well as a visual perturbation in the droplet image collected by the CMOS camera. Figure 4.8 shows an example of a visual evidence that coincided with an interruption of the WGMs. In comparing the images in Figs. 4.9a and 4.9b it can be seen that that the droplet underwent a perturbation in which the droplet's image went out of focus temporarily. The WGMs simply underwent a temporary weakening in their signal intensity. This makes sense as the collision can occur faster than the one second acquisition time of the spectrograph. As the spectrograph is acquiring a signal average over one second, it's conceivable that interruption of WGMs happened for only a fraction of this one second so on average the WGM signal is merely weakened and not completely lost. Furthermore, the possibility that a collision can be so fast that WGM interruption is too quick for a detectable weakening of the WGMs' intensity cannot be dismissed. Therefore, conceptually the method of real-time particle-droplet collisions through WGM perturbations isn't

without its caveats. The visual image of the droplet is probably the less reliable of the two detection methods, as it is likely that not every particle collision lead to a visible change in the image.

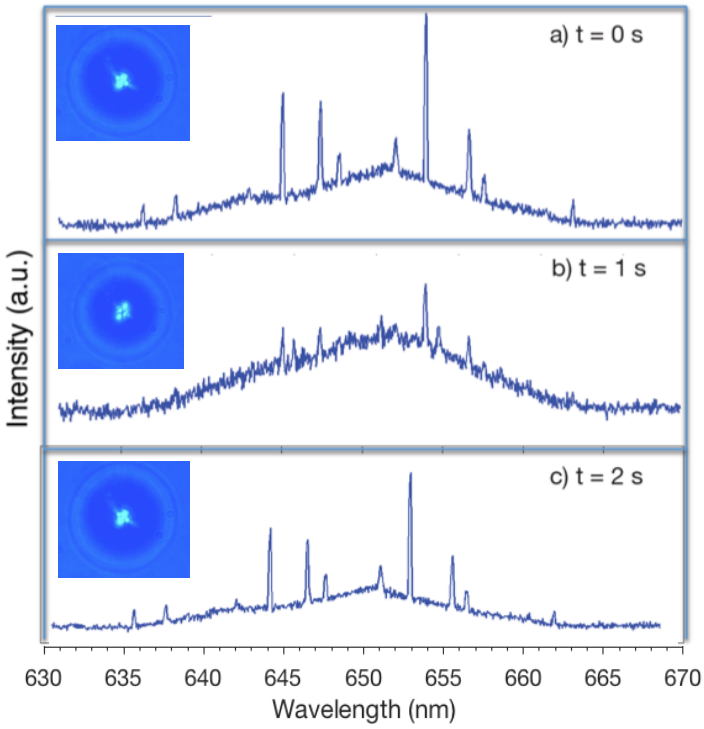

Figure 4.9. Raman spectra and droplet images during ATD particle collisions with a tweezed aqueous droplet. At 0 s (a) the droplet's image and Raman spectrum are acquired just before a collision is observed by the visual perturbation of the image coinciding with weakening WGMs (b). The droplet image at t = 1s is shifted out of focus as the WGMs weaken. A second later the WGMs as well as the image are restored to the state before the perturbation.

The specific WGM peak that resulted in the highest intensity recording on the spectrograph throughout a continuous set of Raman spectra retrievals was chosen and a ratio, denoted γ, of the recorded intensity of this WGM at each frame to the strongest intensity recorded for this WGM throughout all the frames considered was calculated. Figure 4.10 shows this ratio for 200 frames

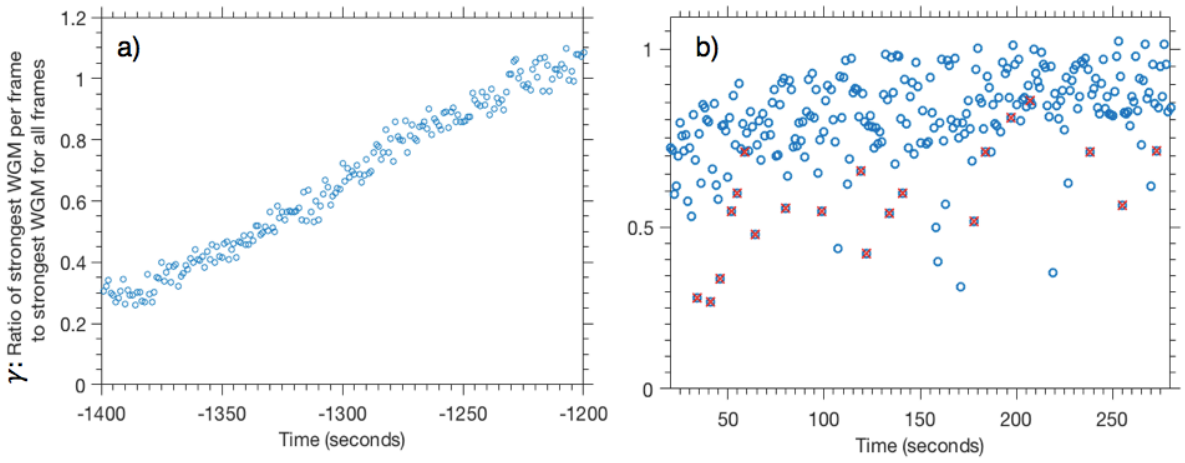

Figure 4.10. a) Ratio of strongest WGM per frame to strongest WGM for all frames γ before dust was introduced into the system. The increasing trend is typical of equilibrated droplets whereby their WGM intensity gradually increases as they become more stable resonators. **b**) γ values during the phase of detectable perturbations. Larger fluctuations are observed and many of the small γ values coincide with a visual perturbation of the droplet's image (red x's).

1400 seconds before collision detection began (left panel, Fig 4.10a) and the ratio over the period of time where visual perturbations were being observed (right panel, Fig 4.10b).

Figure 4.10a shows an increasing trend in γ which is typical for an experiment at steady state That is because the droplet begins to experience less and less perturbations to its size and thus the intensity of a given WGM keeps increasing due to strengthening resonance with the stable droplet. The narrow range of values that γ covers at any particular frame (less than 0.1) is the more important takeaway from Fig. 4.10a and what should be used to contrast with in Fig. 4.10b, when ATD particle collisions were introduced into the chamber. During the period of potential visual collision detection from perturbations to the droplet's image, the range of values γ covered

increased significantly, which corresponds to increased fluctuations of the WGM intensity on short timescales. These fluctuations are what a period of continuous particle collisions would likely lead to. A red x symbol is placed over the γ values that aligned with a visual perturbation (within a 2 second tolerance). There is some correlation between the visual perturbations and decreased WGM intensity, though it is far from perfect. Of the 20 visual perturbations, 14 line up with γ values lower than 0.6 while 8 γ values below that value did not align with any visual image. 2 visual perturbations (around 200 seconds) lined up with γ values that were within the average WGM reduction of all spectra shown in Fig. 4.10b.

The results from this experiment do provide evidence that the visual image and the WGMs have the potential to detect particle collisions but the evidence isn't conclusive. Visual perturbations that did not align with low γ values may have been too quick to detectably alter the WGM signal. Conversely a particle collision should not be expected to always perturb the image. A visual perturbation indicates droplet movement which a low velocity impact or a small low inertia particle may not be capable of instigating. Many more tests are needed to conduct an improved statistical analysis on the relation between low γ values and perturbed images. If γ is relatable to the collision frequency, it would provide a very unique capability to efficiently assess collision rates that would be needed for proper quantification of contact freezing.

4.7 Capabilities of the current COAT system, its limitations, and future work

While the achieved ice supersaturations present a significant stride towards achieving conditions close to those of mixed phase clouds (around 100% RH_w) they remain insufficiently low for studying the freezing of water droplets. At the estimated 92% RH_w for example, the equilibrium KCl molar ratio is around 8%. The resultant freezing point depression would be around

-10 °C (Haghighi et al. 2008), which could be accounted for during future ice nucleation experiments but would remain a large caveat in the interpretation of freezing data especially considering the much smaller expected discrepancies in freezing temperatures between immersion and contact freezing. An even more fundamental hurdle in the application of the developed system to freezing experiments is its inability to retain ice crystals in the optical trap. With oil immersion objectives (instead of the ultra-long working distance objective used in the COAT) non-spherical crystalline particles can be retained, at least for a few minutes, as shown in Ishizaka et al. (2011). Further an effloresced KCl particle had been also been retained in the system described here when an oil immersion objective was used. So there is some potential for overcoming this limitation with more careful testing of crystal stability in the trap. Individual detection of particle collisions does present a very unique feature of the method, and provides some incentive for continued development to achieve freezing abilities in the system.

The current generation of the COAT may not be developed enough for controlled contact freezing experiments but does provide alternative research opportunities in this early phase. A more involved investigation of what is triggering the discrepancy between the measured and expected refractive indices as the droplet is cooling/evaporating could be a worthwhile research pursuit, with potential implications on water's diffusive behavior and microscale transport at low temperatures.

4.8 Conclusions

A novel chilled optical aerosol tweezers (COAT) has been designed and constructed. The system is capable of the basic features of a traditional optical tweezers while cooling droplets down to sub-zero temperatures. This is the first demonstration of optical trapping of supercooled aqueous

droplets in the temperature range of 0 to -15 °C relevant to heterogeneous ice nucleation. The chamber design has been shown to achieve ice supersaturation conditions, which is a requirement for producing the thermodynamically metastable supercooled water state. At -12 °C a lower bound of 92% was found for the estimated RH_w which equates to an ice supersaturation of around 5%.

Retrieved Raman spectra of a KCl droplet while being cooled showed evidence of potentially higher surface salt concentrations than in the interior. The re-convergence of the expected bulk salt concentration with the estimated surface salt concentration (via the measured refractive index) points to a transient salt gradient effect occurring during droplet evaporation. Surface segregation of salts has been shown to have important atmospheric implications, which deems further investigating this trend a worthy endeavor. Finally, the system is shown to be sensitive to real time particle collisions via weakening of the WGMs as well as perturbation of the retrieved visual image. An imperfect correlation between WGM and visual image perturbation indicates that more collision tests are needed to examine to what extent an accurate collision frequency can be determined from the real time perturbations of the Raman spectrum.

References

Antonsson, E., Patanen, M., Nicolas, C., Neville, J. J., Benkoula, S., Goel, A. and Miron, C.: Complete bromide surface segregation in mixed NaCl=NaBr aerosols grown from droplets, Phys. Rev. X, 5(1), 2015.

Cai, C., Stewart, D. J., Reid, J. P., Zhang, Y. H., Ohm, P., Dutcher, C. S. and Clegg, S. L.: Organic component vapor pressures and hygroscopicities of aqueous aerosol measured by optical tweezers, J. Phys. Chem. A, 119(4), 704–718, 2015.

Cantrell, W. and Heymsfield, A.: Production of Ice in Tropospheric Clouds: A Review, Bull. Am. Meteorol. Soc., 86(6), 795–807, doi:10.1175/BAMS-86-6-795, 2005.

DeMott, P. J., Prenni, A. J., Liu, X., Kreidenweis, S. M., Petters, M. D., Twohy, C. H. and Richardson, M. S.: Predicting global atmospheric ice nuclei distributions and their impacts on climate, PNAS, 107(25), 11217–11222, doi:10.1073/pnas.0910818107, 2010.

DeMott, P. J., Möhler, O., Stetzer, O., Vali, G., Levin, Z., Petters, M. D., Murakami, M., Leisner, T., Bundke, U., Klein, H., Kanji, Z. A., Cotton, R., Jones, H., Benz, S., Brinkmann, M., Rzesanke, D., Saathoff, H., Nicolet, M., Saito, A., Nillius, B., Bingemer, H., Abbatt, J., Ardon, K., Ganor, E., Georgakopoulos, D. G. and Saunders, C.: Resurgence in Ice Nuclei Measurement Research, Bull. Am. Meteorol. Soc., 92(12), 1623–1635, doi:10.1175/2011BAMS3119.1, 2011.
Durant, A. J. and Shaw, R. A.: Evaporation freezing by contact nucleation inside-out, Geophys. Res. Lett., 32(20), L20814, doi:10.1029/2005GL024175, 2005.

Ervens, B. and Feingold, G.: On the representation of immersion and condensation freezing in cloud models using different nucleation schemes, Atmos. Chem. Phys., 12, 5807–5826, doi:10.5194/acp-12-5807-2012, 2012.

Gettelman, A., Liu, X., Barahona, D., Lohmann, U. and Chen, C.: Climate impacts of ice nucleation, J. Geophys. Res., 117(D20), doi:10.1029/2012JD017950, 2012.

Ghosal, S., Shbeeb, A. and Hemminger, J. C.: Surface segregation of bromine in bromide doped NaCl: Implications for the seasonal variations in Arctic ozone, Geophys. Res. Lett., 27(13), 1879–1882, doi:10.1029/2000GL011381, 2000.

Gorkowski, K., Beydoun, H., Aboff, M., Walker, J. S., Reid, J. P. and Sullivan, R. C.: Advanced aerosol optical tweezers chamber design to facilitate phase-separation and equilibration timescale experiments on complex droplets, Aerosol Sci. Technol., 50(12), 1327–1341, doi:10.1080/02786826.2016.1224317, 2016.

Gurganus, C., Kostinski, A. B. and Shaw, R. A.: High-speed imaging of freezing drops: Still no preference for the contact line, J. Phys. Chem. C, 117(12), 6195–6200, 2013.

Hargreaves, G., Kwamena, N. O. A., Zhang, Y. H., Butler, J. R., Rushworth, S., Clegg, S. L. and

Reid, J. P.: Measurements of the equilibrium size of supersaturated aqueous sodium chloride droplets at low relative humidity using aerosol optical tweezers and an electrodynamic balance, J. Phys. Chem. A, 114(4), 1806–1815, 2010.

Hecht, E.: Optics 4th edition, Opt. 4th Ed. by Eugene Hecht Read. MA AddisonWesley Publ. Co. 2001, 1, 122, doi:10.1119/1.3274347, 2001.

Hess, M., Krieger, U. K., Marcolli, C., Huthwelker, T., Ammann, M., Lanford, W. A. and Peter, T.: Bromine Enrichment in the Near-Surface Region of Br-Doped NaCl Single Crystals Diagnosed by Rutherford Backscattering Spectrometry, J. Phys. Chem. A, 111(20), 4312–4321, doi:10.1021/jp0674120, 2007.

Hiranuma, N., Augustin-Bauditz, S., Bingemer, H., Budke, C., Curtius, J., Danielczok, A., Diehl, K., Dreischmeier, K., Ebert, M., Frank, F., Hoffmann, N., Kandler, K., Kiselev, A., Koop, T., Leisner, T., Möhler, O., Nillius, B., Peckhaus, A., Rose, D., Weinbruch, S., Wex, H., Boose, Y., DeMott, P. J., Hader, J. D., Hill, T. C. J., Kanji, Z. A., Kulkarni, G., Levin, E. J. T., McCluskey, C. S., Murakami, M., Murray, B. J., Niedermeier, D., Petters, M. D., O'Sullivan, D., Saito, A., Schill, G. P., Tajiri, T., Tolbert, M. A., Welti, A., Whale, T. F., Wright, T. P. and Yamashita, K.: A comprehensive laboratory study on the immersion freezing behavior of illite NX particles: a comparison of 17 ice nucleation measurement techniques, Atmos. Chem. Phys., 15(5), 2489–2518, doi:10.5194/acp-15-2489-2015, 2015.

Hoffmann, N., Duft, D., Kiselev, A. and Leisner, T.: Contact freezing efficiency of mineral dust aerosols studied in an electrodynamic balance: quantitative size and temperature dependence for illite particles, Faraday Discuss., 165, 383, doi:10.1039/c3fd00033h, 2013a.

Hoffmann, N., Kiselev, A., Rzesanke, D., Duft, D. and Leisner, T.: Experimental quantification of contact freezing in an electrodynamic balance, Atmos. Meas. Tech., 6(9), 2373–2382, doi:10.5194/amt-6-2373-2013, 2013b.

Hopkins, R. J., Mitchem, L., Ward, A. D. and Reid, J. P.: Control and characterisation of a single aerosol droplet in a single-beam gradient-force optical trap, Phys. Chem. Chem. Phys., 6(21), 4924, doi:10.1039/b414459g, 2004.

Van De Hulst, H. C.: Light Scattering by Small Particles, edited by D. Publications, Dover Publications., 1981.

Ishizaka, S., Wada, T. and Kitamura, N.: In situ observations of freezing processes of single micrometer-sized aqueous ammonium sulfate droplets in air, Chem. Phys. Lett., 506(1–3), 117–121, doi:10.1016/j.cplett.2011.02.058, 2011.

Ladino, L., Stetzer, O., Lüönd, F., Welti, A. and Lohmann, U.: Contact freezing experiments of kaolinite particles with cloud droplets, J. Geophys. Res., 116(January), 1–12, doi:10.1029/2011JD015727, 2011.

Liu, Y. and Daum, P. H.: Relationship of refractive index to mass density and self-consistency of

mixing rules for multicomponent mixtures like ambient aerosols, J. Aerosol Sci., 39(11), 974–986, doi:10.1016/j.jaerosci.2008.06.006, 2008.

Miles, R. E. H., Walker, J. S., Burnham, D. R. and Reid, J. P.: Retrieval of the complex refractive index of aerosol droplets from optical tweezers measurements, Phys. Chem. Chem. Phys., 14(9), 3037, 2012.

Mitchem, L. and Reid, J. P.: Optical manipulation and characterisation of aerosol particles using a single-beam gradient force optical trap., Chem. Soc. Rev., 37(4), 756–69, doi:10.1039/b609713h, 2008.

Morrison, H., de Boer, G., Feingold, G., Harrington, J., Shupe, M. D. and Sulia, K.: Resilience of persistent Arctic mixed-phase clouds, Nat. Geosci., 5(1), 11–17, doi:10.1038/ngeo1332, 2011.

Murray, B. J., O'Sullivan, D., Atkinson, J. D. and Webb, M. E.: Ice nucleation by particles immersed in supercooled cloud droplets, Chem. Soc. Rev., 41(19), 6519, doi:10.1039/c2cs35200a, 2012.

Nagare, B., Marcolli, C., Welti, A., Stetzer, O. and Lohmann, U.: Comparing contact and immersion freezing from continuous flow diffusion chambers, Atmos. Chem. Phys., 16(14), 8899–8914, doi: 10.5194/acp-16-8899-2016, 2016.

Niehaus, J. and Cantrell, W.: Contact freezing of water by salts, J. Phys. Chem. Lett., 2015, 6 (17), pp 3490–3495, doi: 10.1021/acs.jpclett.5b01531, 2015

Power, R. M. and Reid, J. P.: Probing the micro-rheological properties of aerosol particles using optical tweezers., Rep. Prog. Phys., 77(7), 74601, doi:10.1088/0034-4885/77/7/074601, 2014.

Preston, T. C. and Reid, J. P.: Accurate and efficient determination of the radius, refractive index, and dispersion of weakly absorbing spherical particle using whispering gallery modes, J. Opt. Soc. Am. B, 30(8), 2113–2122, doi: org/10.1364/JOSAB.30.002113, 2013.

Preston, T. C. and Reid, J. P.: Determining the size and refractive index of microspheres using the mode assignments from Mie resonances, J. Opt. Soc. Am. A, 32(11), 2210, doi:10.1364/JOSAA.32.002210, 2015.

Pruppacher, H. R. and Klett, J. D.: Microphysics of Clouds and Precipitation, edited by R. D. Rosen, Kluwer Academic Publishers., 1997.

R. K. Chang, B. P. W.: Optical Effects Associated with Small Particles, World Scientific, Singapore., 1988.

Reid, J. P. and Mitchem, Laser probing of single-aerosol droplet dynamics, Annu. Rev. Phys. Chem., 57(1), 245–271, doi: 10.1146/annurev.physchem.57.032905.104621, 2006.

Symes, R., Sayer, R. M. and Reid, J. P.: Cavity enhanced droplet spectroscopy: Principles,

perspectives and prospects, Phys. Chem. Chem. Phys., 6(3), 474, doi:10.1039/b313370b, 2004.
Vali, G. and Snider, J. R.: Time-dependent freezing rate parcel model, Atmos. Chem. Phys., 15(4), 2071–2079, doi:10.5194/acp-15-2071-2015, 2015.

Chapter 5: Conclusions

The research efforts presented in each chapter of this dissertation were all aimed at improving our understanding of heterogeneous ice nucleation. A combination of theoretical modelling, formulating alternative data analysis schemes, and developing new measurement techniques form the bulk of the work. Perhaps it can be said that the complexity of heterogeneous ice nucleation manifests in the myriad of research tools employed.

In Chapter 2 a new framework describing heterogeneous ice nucleation was formulated. A continuum assumption was carried out to establish a distribution containing the heterogeneous ice nucleating (HIN) activity of a particle species. When the critical area was hypothesized, it presented a challenge to the effort made to encompass the HIN activity into one distribution. The success of the random sampling process to predict the freezing behavior below the critical area however gave some validity to an encompassing distribution. An implicit theme, which recurred in Chapter 3, is the contrast between the singular and the continuous. The contrast shows up first in the fundamental difference between stochastic and deterministic and then later in the breakdown of the assumption of one active site density function or one distribution of HIN. The framework could capture droplet freezing behavior over many ranges of particle surface area/material concentration for illite NX, MCC cellulose, and Snomax and provided detailed reasoning of why the commonly used active site density function is problematic, as the diagnostic fails at capturing the complexity of competing contact angle ranges of the distribution of HIN activity. It was speculated that this could be part of the reason why active site densities from the wet and dry dispersion methods don't align for the same freezing temperatures.

In Chapter 3 the framework was taken one step further and expanded to model the freezing behavior of mixtures of different types of HIN particles or ice nucleants. Of particular interest was the biological particle-dust system, a proxy of which, Snomax-illite, was examined in the lab. Snomax in itself was argued to be a mixture of species; two distributions of HIN activity captures the freezing temperature spectral range observed when spanning seven orders of magnitude of Snomax material concentration in droplets. This was consistent with the hypothesis that *Pseudomonas syringae* consists of two dominant ice nucleating protein aggregate classes, type I and III. Snomax displayed its singular behavior when at the limit of its occurrence (very low concentrations) it retained the stronger range of HIN activity of the second distribution. At low concentrations Snomax' decay was abrupt, whereby a very well defined lowest droplet freezing temperature was observed. This singular behavior meant that no new intermediate freezing temperature regime would manifest when Snomax is mixed with illite particles in individual droplets.

Application of the new mixing model to mixtures of dust can be a very beneficial exercise that is well within the resources available at CAPS. This is important in answering the question of whether the distribution of a lower temperature ice nucleating dust regime can be attributed one distribution of ice nucleating activity. The work on bio-dust mixtures also has a lot of room for growth by examining different biological and dust samples. For example, using fungal spores instead of bacteria and feldspars instead of illite. Snomax exhibited such singular behavior that other biological particles may not, allowing them to contribute a high efficiency freezing regime between that of dust and biological particles.

Chapter 4 compiled the work of a challenging project: to design and construct a chilled optical aerosol tweezers (COAT). It could be said that resolving a decades' old outstanding uncertainty,

the contact freezing mode, cannot be done trivially. The system made meaningful strides towards the goal, and opened alternative avenues of research. The COAT was shown to be capable of trapping an aqueous water droplet, cool it down to subzero temperatures, and hold it stably at a fixed subzero temperature. This was done with minimal deterioration in the whispering gallery mode (WGM) quality in the droplet's Raman spectrum, such that the droplet's size and refractive index were determined at these subzero conditions with a good degree of confidence, for the first time. From the information gathered, the relative humidity in the system was estimated and found to be above ice saturation. This is a major design achievement in itself. As the droplet floats in the radial center of a chilled chamber, it is very difficult for it to be colder than its surrounding. In fact, its most certainly going to be warmer which means it has a higher vapor pressure requirement to retain an equilibrium size than the colder nearby walls. With ice deposition on walls very likely at freezing temperatures, maintaining ice saturation at the droplet's position is difficult in and of itself. However, with careful design of the critical trapping area and an optimized trapping protocol minimizing salt deposition on the window below the droplet, high moisture levels were retained. The second hurdle to conducting contact freezing is being able to controllably collide particles with the trapped droplet. Collision tests presented indicate sensitivity of visual image and WGMs to dust perturbations.

Admittedly the technical hurdles that have been overcome through the COAT system don't mean that direct contact freezing experiments are possible right away. But many design lessons have been acquired in the process and can guide improvements to the next generation COAT. The current design can conduct some exciting measurements on evaporating aqueous droplets exhibiting potential discrepancies between their bulk and surface concentrations. The restoration of the refractive index measured at the surface to a value consistent with the amount of water lost

from the droplet does beg the question of what caused its increase during cooling. Short term future experiments can investigate this behavior further by repeating the tests described here at varied conditions of cooling rate, hold temperatures, initial salt concentration, and even rewarming the droplet. This should begin to narrow down what variables are most contributing to the phenomena being observed. More tests on the capability of the tweezers to evaluate collision frequency are also worthwhile endeavors within themselves that can be conducted with the current system. The tests reported here can be repeated for varied dust concentrations to try and correlate concentration with collision frequency. Size selection of the dust particles can also aid in the answering the question of how sensitive the collisions are to size.

The findings in all three chapters therefore can be used as research aids or launching points for new research endeavors at the Center for Atmospheric Particle Studies (CAPS) at Carnegie Mellon University. The hope is that the new formulation in Chapter 2 and its expanded form in Chapter 3 can facilitate interpretation of droplet freezing temperature spectra for current and future aerosol particle systems examined at CAPS, and to also improve the experimental design and data analysis methods used by the international ice nucleation community.

Appendix: Matlab script to produce modelled frozen fraction curves in Chapters 2 and 3

The following Matlab script was written and implemented to produce the modelled frozen fraction curves shown in Chapters 2 and 3:

```
bin_width=1e-4; %define width of each discrete theta bin

T=273:-0.5:233; %Temperature in K

th=0:bin_width:pi; %define theta array

mu_bar=0.6; %define mean of g_bar distribution

sig_bar=0.05; %define standard deviation of g distribution

g_bar=norma(th,mu_bar,sig_bar); %define g_bar as a normal distribution using
                                %using fucntion norma

A_c=1e-9; %critical surface area in m2

A_p=A_c*0.1; %surface area of particles being modelled

n_draws=80; %number of draws from g_bar

N=60; %number of particle surfaces/droplets modelled

g_star=zeros(N,length(th)); %define matrix of g_star distributions

%the following double for loop conducts random sampling of thetas
% from g_bar for every droplet/particle surface n_draws times

for j=1:N
for i=1:n_draws
    x=floor(rand*length(th))+1; %random variable between 0 and pi
    g_star(j,x)=g_bar(x);
end
end


j=1:N;

g_star(j,:)=((g_star(j,:)/(trapz(th,g_star(j,:))))); %normalize all g_star
                                                     %distributions
```

```
run Pf_info.m %run script containing all information to compute freezing
              %probabilities

dT=0.01667; %specify cooling rate K/second

Q=zeros(1,length(T)); %Defined to evaluate the first integral over theta in
Pf

Pf=zeros(N,length(T)); %the freezing probabilities of all droplets

Pf_bar=zeros(1,length(T)); %the array for freezing probability using g_bar

Pf_avg=zeros(1,length(T)); %average of freezing probabilities of all droplets
                           %at each T


%the following double loop evaluates the freezing probabilities using
%Pf_info.m, g_bar, and all g_star's

for j=1:N

for l=2:length(T)

    Q(j,l)=-trapz(th,g_p(j,:).*J(l,:));

    Pf(j,l)=1-exp(-(A_p/dT)*trapz(T(1:l),Q(j,1:l)));

    Pf_bar(l)=1-exp(-(A_c/dT)*trapz(T(1:l),Q1(1:l)));

    Pf_avg(l)=mean(Pf(:,l));

end

end


%Pf_info.m is a subscript imbedded in the preceding script and evaluated
%the ice nucleation rate J as a function of theta and temperature

n=1e15;  %cm-2

k=1.3806488*1e-23; %boltzmann constant J/K

Mw=18; %water molecular weight

ro=0.9167; %density of ice g.cm-3

Na=6.023*1e23; %avogadro's number

f=(0.25)*(2+cos(th)).*((1-cos(th)).^2); %catalytic factor

T=273:-0.5:233; %temperature range in K
```

```
dF=((k*(T.^2)*892)./((T-118).^2)); %diffusion energy F

Tr=((T-273)/(273)); %reduced temperature

Ts=373.16;

To=273.16;

ews=1013.246; %atmospheric pressure

eio=6.1071; %ice vapor pressure

%Liquid vapor pressure vs. Temperature:
Pl=10.^(-7.90298*((Ts./T)-1)+5.02808*log10(Ts./T)-1.3816*1e-
7*(10.^(11.344*(1-T./Ts))-1)+8.3128*1e-3*(10.^(-3.19149*(Ts./T))-
1)+log10(ews));

%Ice vapor pressure vs. Temperature:
Pice=10.^(-9.09718*((To./T)-1)-3.56654*log10(To./T)+0.876793*(1-
(T./To))+log10(eio));

S=Pl./Pice;

v=(Mw/(ro*Na))*((1-0.05294*Tr-0.05687*(Tr.^2)-0.002913*(Tr.^3)).^-1); %volume
of H20 in ice cm3

sig=(3.298*1e-6+(1.2048*1e-6)*Tr-(4.6705*1e-5).*(Tr.^2)); %surface tension of
supercooled water J/cm2

dG=((16*pi)/(3))*(((v.^2).*(sig.^3))./((k*T.*log(S)).^2)); %Gibbs free energy

h=6.62606957*1e-34; %Plank's constant

J=zeros(length(T),length(th)); %the nucleation rates as a function of theta
and T

for i=1:length(th) %making a J matrix with theta and T dimensions
    J(:,i)=((k*T*n)/(h)).*exp(-(dF./(k*T))).*exp(-f(i)*(dG./(k*T)));
end
```